UNIVERSITY of CALIFORNIA

SANTA CRUZ

THE EVOLUTION OF BINARIES IN A GASEOUS MEDIUM: THREE-DIMENSIONAL SIMULATIONS OF BINARY BONDI-HOYLE-LYTTLETON ACCRETION

A thesis submitted in partial satisfaction of the requirements for the degree of

BACHELOR OF SCIENCE

in

PHYSICS

by

Andrea Antoni

17 Aug 2018

The thesis of Andrea Antoni is approved by:

_____

Professor Enrico Ramirez-Ruiz
Advisor

_____

Professor Alexander Sher
Senior Theses Coordinator

_____

Professor Robert P. Johnson
Chair, Department of Physics

Abstract

The Evolution of Binaries in a Gaseous Medium: Three-Dimensional Simulations of

Binary Bondi-Hoyle-Lyttleton Accretion

by

Andrea Antoni

Binary stars are not rare. While only close binary stars may eventually interact with one another, even the widest binary systems interact with their gaseous surroundings. The rates of accretion and the gaseous drag forces arising in these interactions are the key to understanding how these systems evolve. This thesis examines accretion flows around a binary system moving supersonically through a background gas. We perform three-dimensional hydrodynamic simulations of Bondi-Hoyle-Lyttleton accretion using the adaptive mesh refinement code FLASH. We simulate a range of values of initial semi-major axis of the orbit relative to the gravitational focusing impact parameter of the pair. On large scales, gas is gravitationally focused by the center-of-mass of the binary, leading to dynamical friction drag and to the accretion of mass and momentum. On smaller scales, the orbital motion imprints itself on the gas. Notably, the magnitude and direction of the forces acting on the binary inherit this orbital dependence. The long-term evolution of the binary is determined by the timescales for accretion, slowing of the center-of-mass, and orbital inspiral. We use our simulations to measure these timescales and to establish a hierarchy between them. Our simulations indicate that binaries moving through gaseous media will slow down before the orbit decays. We find that the timescale for orbital inspiral is proportional to the semi-major axis to the +0.19 power. Gas drag can tighten the orbit until gravitational wave radiation dominates. We use our measured inspiral timescale to find the critical separation where this occurs.

Contents

List of Figures

List of Tables

For David.

1

Introduction

The capture, or accretion, of gas by a star from its surroundings is a classical problem in astrophysics. The brightness, mass, metal-content, and evolutionary fate of the star are intimately related to the star's accretion history and the timescales over which the episodes of accretion occurred. Studies of accretion flows around embedded stars began with the work of Hoyle and Lyttleton [1] who derived, analytically, the rate of accretion expected for a point mass in supersonic, straight-line motion relative to a uniform background gas. They were the first to acknowledge that an embedded star has a capture radius (or, accretion radius) that exceeds its geometric radius as a result of the star's gravitational influence on the surrounding gas. Bondi and Hoyle [2] extended the analysis to include hydrodynamical effects, allowing for the buildup of a finite-sized downstream wake. Although the theory of gravitational drag (dynamical friction) for collisionless systems was still in its infancy [3], Bondi and Hoyle pointed out that the gravitationally-induced wake would exert a gravitation force on the star, depleting the star's linear momentum relative to the gas [2].

For the solitary object described above, the drag force exerted by the wake acts purely along the line of motion of the object [4]. In a binary system, on the other hand, the two objects

move along curved paths. In addition to the linear momentum of the center of mass (CM), the orbital motional introduces a net angular momentum about the CM. The drag forces exerted on each object will torque the binary, leading to a metamorphosis of the size and shape of their shared orbit. The introduction of a time-dependent potential drastically alters the steady-state nature of the classical Bondi, Hoyle, and Lyttleton (BHL) problem, preventing a simple formalism from effectively describing the drag on the center of mass or the orbital decay [5, 6, 7].

The effects of accretion and drag can have profound consequences. For example, a metal-poor star (consisting primarily of hydrogen and helium) moving through the interstellar medium (ISM) could accrete, over its history, enough material to significantly enhance its birth metallicity [8]. More dramatically, a stellar-mass black hole binary (BHB) embedded in an AGN disk may be hardened by drag torques due to the gaseous part of the disk and be brought to a small enough binary separation to be able to merge under the influence of gravitational wave (GW) radiation within the age of the Universe [9]. Whether these binaries form *in situ* or are dynamically captured [10], they may be the only case of BHB mergers that are accompanied by an electromagnetic signature since they are embedded in a dense, gaseous disk [9].

Our goal in this paper is to examine the nature of accretion and drag experienced by binaries moving through gaseous environments and to learn the extent to which we can derive physical intuition from the classical BHL formalism [1, 11, 2]. To that end, we perform three-dimensional (3D) hydrodynamical studies using the adaptive mesh refinement code FLASH [12]. We simulate binary systems across a wide range of values of the orbital semi-major axis of the pair. We calculate the forces, accretion rates, and fundamental timescales governing the evolution of binaries as a function of initial semi-major axis.

This paper is organized as follows. In the next chapter, we explain the BHL formalism,

we define relevant quantities from two-body dynamics, we extend the BHL formalism to to binary systems, and we consider the scales for several typical encounters in astrophysics. In chapter 3, we describe our numerical method. In chapter 4, we present the results of our simulations. In chapter 5, we apply our results to astrophysical systems. In chapter 6, we conclude.

2

Background

2.1 Characteristic Scales in Binary BHL Flows

A single point mass moving through an initially-uniform background gas accelerates matter in its direction as it moves. Suppose the motion of the particle is supersonic and follows a straight-line trajectory. A symmetric bow shock forms about the line of motion of the point mass and shocked gas piles up in a stagnation region downstream. The point mass accretes gravitationally bound material from the wake while the rest is eventually advected downstream. Although the material in the wake is transient, the overall structure of the wake persists and it exerts a gravitational drag force on the point mass until there ceases to be relative motion between the particle and the gas. The BHL formalism provides the analytical estimates that are the natural starting point for considering the long-term evolution of the particle's interaction with the gas. Let M be the mass of the particle, v_∞ the speed of the particle relative to the gas at infinity, and $c_{s,\infty}$ the sound speed of the gas at infinity[1]. We define the Mach number of the flow to be $\mathcal{M}_\infty = v_\infty / c_{s,\infty}$. The particle's in-

---

[1]These quantities must be specified at infinity because, at finite distances, the gas is perturbed by the presence of the gravitating object.

fluence on the gas may be characterized by its accretion radius. If the particle moves supersonically, we may use the Hoyle-Lyttleton (HL) accretion radius

$$R_{a} = \frac{2GM}{v_{\infty}^2} \tag{2.1}$$

[1], where G is the gravitational constant. For very subsonic motion, the accretion radius is given by the Bondi radius

$$R_B = \frac{GM}{c_{s,\infty}^2} \tag{2.2}$$

[2]. In the transonic regime, $\mathcal{M}_{\infty} \sim 1$, the work of Bondi and Hoyle [11, 2] led to the interpolation formula

$$R_{\mathrm{BH}} = \frac{2GM}{v_{\infty}^2 + c_{s,\infty}^2} \tag{2.3}$$

which we refer to as the Bondi-Hoyle (BH) radius. In general, BHL predicts an accretion rate that is given by the flux of matter through a circular cross-section far upstream from the particle, where the radius of the cross-section is the accretion radius of the particle. In the supersonic regime, this gives

$$\dot{M}_{\mathrm{HL}} = \pi R_{a}^2 \rho_{\infty} v_{\infty} = 4\pi G^2 M^2 \rho_{\infty} v_{\infty}^{-3} \tag{2.4}$$

[1]. The drag force on the particle due to the wake is then

$$F_{\mathrm{HL}} = \dot{M}_{\mathrm{HL}} v_{\infty} = 4\pi G^2 M^2 \rho_{\infty} v_{\infty}^{-2} \tag{2.5}$$

and the rate at which energy is dissipated is

$$\dot{E}_{\mathrm{HL}} = \frac{1}{2}\dot{M}_{\mathrm{HL}} v_{\infty}^2 = 2\pi G^2 M^2 \rho_{\infty} v_{\infty}^{-1}. \tag{2.6}$$

The time it take for the particle to stop is

$$\tau_{\mathrm{stop,HL}} \equiv \frac{\frac{1}{2}M v_{\infty}^2}{\dot{E}_{\mathrm{HL}}} = \frac{v_{\infty}^3}{4\pi G^2 M \rho_{\infty}}. \tag{2.7}$$

For mild Mach numbers, we instead write equations 2.4, 2.5, 2.6, and 2.7 using R_{BH} and we replace the characteristic velocity v_∞ with $(v_\infty^2 + c_{s,\infty}^2)^{1/2}$. The BH accretion rate is then

$$\dot{M}_{\mathrm{BH}} = \pi R_{\mathrm{BH}}^2 \rho_\infty (v_\infty^2 + c_{s,\infty}^2)^{1/2} = \frac{4\pi G^2 M^2 \rho_\infty}{(v_\infty^2 + c_{s,\infty}^2)^{3/2}} \tag{2.8}$$

[13]. The BH drag force becomes

$$F_{\mathrm{BH}} = \dot{M}_{\mathrm{BH}}(v_\infty^2 + c_{s,\infty}^2)^{1/2} = 4\pi G^2 M^2 \rho_\infty (v_\infty^2 + c_{s,\infty}^2)^{-1} \tag{2.9}$$

and the BH energy dissippation rate is

$$\dot{E}_{\mathrm{BH}} = \frac{1}{2}\dot{M}_{\mathrm{BH}}(v_\infty^2 + c_{s,\infty}^2) = 2\pi G^2 M^2 \rho_\infty (v_\infty^2 + c_{s,\infty}^2)^{-1/2}, \tag{2.10}$$

which gives a BH stopping time of

$$\tau_{\mathrm{stop,BH}} \equiv \frac{\frac{1}{2}M(v_\infty^2 + c_{s,\infty}^2)}{\dot{E}_{\mathrm{BH}}} = \frac{(v_\infty^2 + c_{s,\infty}^2)^{3/2}}{4\pi G^2 M \rho_\infty}. \tag{2.11}$$

Of course, the above equations are only approximately correct, but the coefficients for drag and accretion for the above canonical case have been obtained numerically [13, 14, 15, 16, 17]. See Edgar [18] for a review of the BHL accretion formalism, including derivations of the above equations, and Ostriker [4] for the first analytical treatment of the gaseous dynamical friction (DF) drag approximated by the expressions for F_{HL} and F_{BH}.

For convenience, we note that with $\beta = \mathcal{M}_\infty^2/(1+\mathcal{M}_\infty^2)$,

$$R_{\mathrm{BH}} = \beta R_{\mathrm{a}} \qquad \dot{M}_{\mathrm{BH}} = \beta^{3/2}\dot{M}_{\mathrm{HL}}$$
$$F_{\mathrm{BH}} = \beta F_{\mathrm{HL}} \qquad \dot{E}_{\mathrm{BH}} = \beta^{1/2}\dot{E}_{\mathrm{HL}} \tag{2.12}$$

and

$$\tau_{\mathrm{stop,BH}} = \beta^{-3/2}\tau_{\mathrm{stop,HL}}. \tag{2.13}$$

Now consider what happens when we replace the single point mass M with two point masses, m_1 and m_2, whose total mass is M, and whose CM moves in a straight line with velocity $\mathbf{v}_\infty$

relative to the gas. Things are already more complicated because we now must specify the binary

mass ratio, the initial eccentricity of the orbit, the inclination of the orbital plane relative to $\mathbf{v}_\infty$, and

the initial semi-major axis of the orbit, a_0. Let us take the simplest case of an equal-mass binary

in an, initially, circular orbit, and inclination of $\frac{\pi}{2}$ (that is, the incoming gas intercepts the binary

"edge-on" to the orbit). Given these assumptions, the initial orbit is fully described by a_0, but we

have yet to characterize the influence of the binary on the gas. Consider, for a moment, a binary

with very small a. The binary approaches a single particle of total mass $M = m_1 + m_2$, located at the

binary's CM. This motivates us to retain equation 2.3 to describe the accretion radius of the CM.

Because the standoff distance of the shock front induced by a particle of mass M is $\sim R_{BH}$, we are

also motivated to consider what happens in the two regimes $a < R_{BH}$ and $a \gtrsim R_{BH}$.

2.1.1   Case $a < R_{BH}$

If $a < R_{BH}$, the orbiting binary is contained within the shock structure of a single particle

of the same total mass. The rates of accretion and drag are determined by the size and density of

the downstream wake, which we would expect to be similar to the single-particle case. Therefore,

equation 2.8 gives the total accretion rate of the pair, equation 2.9 represents the drag force on the

CM of the binary, and we expect the CM motion of the binary to cease in a time $\tau_{\text{stop,BH}}$ (equation

2.11). In this regime, the large-scale structure is largely blind to the presence of a binary (instead

of a single object), but at scales smaller than $\sim R_{BH}$ the orbital motion of the binary matters. For a

binary in a circular orbit, the orbital speed is $v_{\text{orb}} = \sqrt{GM/a}$, or $a = GM/v_{\text{orb}}^2$. Therefore

$$\frac{R_{BH}}{a} = \frac{2GM/(v_\infty^2 + c_{s,\infty}^2)}{GM/v_{\text{orb}}^2} = \frac{2v_{\text{orb}}^2}{v_\infty^2 + c_{s,\infty}^2} = \frac{2v_{\text{orb}}^2}{c_{s,\infty}^2(1 + \mathcal{M}_\infty^2)}. \tag{2.14}$$

If $R_{BH} > 2a$, then $v_{\text{orb}}^2 > c_{s,\infty}^2(1 + \mathcal{M}_\infty^2)$ and the orbital motion of the binary is supersonic. This

means that the gas at the orbital separation of the binary cannot be replaced within a single orbit.

Each particle interacts with gas that has already been influenced by its companion. Even though the size and shape of the overall shock front is not changed by the presence of the binary, the material behind the shock, especially at orbital scales, no longer resembles the gas structure of the single-particle case.

2.1.2 Case $a \gtrsim R_{\mathrm{BH}}$

First consider what happens as $a \to \infty$. The orbital velocity of each point mass goes to zero so each particle moves at $\mathbf{v}_\infty$ relative to the gas. Each particle induces its own independent downstream wake (notice that the symmetry axes through the two wakes are parallel since the relative velocity vectors of the two particles are parallel). That is, the system evolves according to the BHL prescription but for two independent particles (each of mass $\frac{1}{2}M$). So as $a \to \infty$, we expect both the accretion rate of the system and the total DF force on the binary to be $\propto (m_1^2 + m_2^2) = M^2/2$.

Once we allow $a \sim R_{\mathrm{BH}}$, the size of the orbit is on the order of the stand-off distance of the shock structure of a single particle of the same total mass. If $a \gtrsim R_{\mathrm{BH}}$, the overall shock structure will certainly change throughout each orbit since each particle traverses the shock structure set up by the other. A major consequence of the orbital motion is the phase-dependence of the velocity of each particle relative to the gas. The magnitude and direction of the drag forces acting on each particle will inherit this orbital dependence. An understanding of the torques exerted on the orbital motion and the forces exerted on the CM require a vector description, as well as an understanding of the flow. Hydrodynamical simulations are required to capture the small- and large-scale structures that contribute to the evolution of the orbital and CM motion of the binary. We expect a/R_{BH} to have a significant impact on the flow. The purpose of this paper is to explore a/R_{BH} and to characterize the evolution of a binary as a function of this ratio.

2.2 Typical Encounters in Binary BHL

Binary systems span many orders of magnitude in mass and semi-major axis and these systems may interact with a wide variety of ambient gases. Some of these systems may evolve in a Hubble time and others may not. In table 2.1, we calculate a/R_{BH} for a sampling of binary systems moving through the ISM. This list is by no means exhaustive; we will consider ambient gases of much higher densities in section 5. Instead, we hope to give a sense of the values of a/R_{BH} that arise in a variety of circumstances. In the table, we assume an isothermal ideal gas, calculating the sound speed as $c_{s,\infty} = \sqrt{k_B T / m_p}$. We also take the CM velocity of the binary, v_∞, to be the dispersion velocity of that medium. This yields the Bondi-Hoyle radius of the CM of the binary (equation 2.3). For the cold ISM, we calculate the sound speed using $T = 10^4$ K [19]. We include two columns for the cold ISM in the table. The first takes $v_\infty = 10$ km s^{-1}, which would be the case for newly formed binaries in the plane of the disk (where the dispersion velocity is $\approx 10-50$ km s^{-1} [20]). The second column for the cold ISM considers motion perpendicular to the disk, which represents halo or bulge binaries crossing the disk plane. For that case, we show a/R_{BH} for the range of dispersion velocities $v_\infty = 100-300$ km s^{-1}. For the hot ISM, we use a temperature range of $T = 10^6 - 10^7$ K [19] and a dispersion velocity of $v_\infty = 100$ km s^{-1} [21, 22].

2.3 Two-Body Orbits

Before we describe our numerical method, it is necessary to define the notation we will use to describe the orbit of the binary. We follow the notation of Hilditch [23] with the exception that we use M to represent the total mass of the binary. Let us summarize the quantities relevant to this paper. If $\mathbf{r}_1$ and $\mathbf{r}_2$ are the positions of m_1 and m_2, respectively, relative to the coordinate origin,

Binary Type	Mass [$M_\odot$]	a	a/R_{BH}		
			Cold ISM		Hot ISM
			motion in plane of disk	*motion perpendicular to disk*	
Stellar Binary	1 + 1	2 $R_\odot$	5×10^{-3}	0.03 - 0.24	0.05 - 0.24
		1 AU	0.05	2.8 - 25	5 - 26
		0.05 pc	531	$10^4 - 10^5$	$10^4 - 10^5$
Massive Stellar Binary	10 + 10	30 $R_\odot$	7×10^{-4}	0.04 - 0.35	0.07 - 0.4
		1 AU	0.005	0.3 - 2.5	0.5 - 2.6
Binary Black Holes	30 + 30	10 $R_\odot$	8×10^{-5}	0.004 - 0.04	0.008 - 0.04
		100 $R_\odot$	8×10^{-4}	0.04 - 0.4	0.08 - 0.4
SMBHs	10^6 - 10^8	1 pc	$10^{-4} - 10^{-2}$	0.01 - 10	0.02 - 11
Double Planet	$3.7 M_{\text{Jup}} + 3.7 M_{\text{Jup}}$	3.9 AU	56	$10^3 - 10^4$	$10^3 - 10^4$

Table 2.1: a/R_{BH} in a variety of encounters. The temperature of the cold ISM and the hot ISM are taken to be $T = 10^4$ K and $T = 10^6 - 10^7$ K, respectively. For the cold ISM with motion in the plane of the disk, we assume the CM moves at $v_\infty = 10$ km s^{-1}. For the cold ISM with motion perpendicular to the disk, we use $v_\infty = 100 - 300$ km s^{-1}. For the hot ISM, we adopt $v_\infty = 100$ km s^{-1}. See the text for references.

then the CM is located at

$$\mathbf{R} = \frac{m_1}{M}\mathbf{r}_1 + \frac{m_2}{M}\mathbf{r}_2. \tag{2.15}$$

Similarly, the velocity of the CM is

$$\mathbf{V} = \frac{m_1}{M}\mathbf{v}_1 + \frac{m_2}{M}\mathbf{v}_2 \tag{2.16}$$

where $\mathbf{v}_1$ and $\mathbf{v}_2$ are the velocities of m_1 and m_2 relative to the origin. Consistent with Hilditch [23], we use capital letters with subscripts for the barycentric quantities. The barycentric positions of m_1 and m_2 are

$$\mathbf{R}_1 = \mathbf{r}_1 - \mathbf{R}$$
$$\mathbf{R}_2 = \mathbf{r}_2 - \mathbf{R} \tag{2.17}$$

and the barycentric velocities are

$$\mathbf{V}_1 = \mathbf{v}_1 - \mathbf{V}$$
$$\mathbf{V}_2 = \mathbf{v}_2 - \mathbf{V}. \tag{2.18}$$

The position of m_1 relative to m_2 is $\mathbf{r} = \mathbf{r}_1 - \mathbf{r}_2$ and the semi-major axis of this "relative" orbit is denoted by a. The semi-major axis of the barycentric orbit of m_1 is

$$a_1 = \frac{m_1}{M} a \tag{2.19}$$

and the semi-major axis of the barycentric orbit of m_2 is

$$a_2 = \frac{m_2}{M} a. \tag{2.20}$$

The linear speeds of the relative orbit, barycentric orbit of m_1, and barycentric orbit of m_2, respectively, are

$$
\begin{aligned}
v_{\mathrm{orb}}^2 &= GM \left[\frac{2}{r} - \frac{1}{a} \right] \\
V_1^2 &= \frac{Gm_2^3}{M^2} \left[\frac{2}{R_1} - \frac{1}{a_1} \right] \\
V_2^2 &= \frac{Gm_1^3}{M^2} \left[\frac{2}{R_2} - \frac{1}{a_2} \right]
\end{aligned}
\tag{2.21}
$$

where $R_1 = |\mathbf{R}_1|$ and $R_2 = |\mathbf{R}_2|$. The total energy of the binary system is

$$E_{\mathrm{orb}} = \frac{-Gm_1 m_2}{2a} \tag{2.22}$$

and the total angular momentum is

$$J_{\mathrm{orb}} = m_1 m_2 \left[\frac{Ga(1-e^2)}{M} \right]^{1/2} \tag{2.23}$$

where e is the eccentricity of the orbit.

3

Numerical approach

We perform simulations of supersonic BHL flows around an embedded binary system. The traditional approach to numerical studies of BHL is to perform simulations in the frame of a point mass by constructing a wind tunnel that sends gas flowing past a single, gravitating sink particle that is fixed at the coordinate origin. The sink particle accretes gas from the domain and the forces experienced by the sink particle due to the gas are recorded at each time step. We modify this approach by instead placing two sink particles in orbit within a wind tunnel. The sink particles are free to move about the domain and we start the simulations in the initial frame of the CM of the binary. The sink particles accrete gas from the domain and actively respond to the forces they experience due to the gas. In the following subsections, we give a brief history of the numerical studies of BHL that are most relevant to the current work, we describe our numerical method, and we outline the parameters chosen for the suite of simulations that we run.

3.1 Previous numerical studies of BHL

Hunt [24] performed the first hydrodynamical simulations of BHL accretion, constructing a two-dimensional mesh around a gravitating point mass that solved the fluid equations at each time step. Assuming reflection symmetry about the line of motion of the point mass and perfect accretion (ie. they surrounded the point mass by a perfectly absorbing sink), they studied flow Mach numbers $\mathcal{M}_\infty = 0.6$, 1.4, and 2.4. Shima [13] improved on the work of Hunt by using an improved numerical scheme that was better-suited to handling shocks, as well as higher resolution. Our equations for the BH accretion radius (equation 2.3) and accretion rate (equation 2.8) adopt the corrected numerical coefficient obtained by Shima. Further numerical advances have allowed much study of the BHL accretion problem and the reader is directed to Edgar [18] and Foglizzo et al. [25] for recent reviews.

Of importance to the current work are the studies of Ruffert and Arnett [26, 27, 15, 14, 16], which explored BHL accretion across an exhaustive range of parameter space. They performed three-dimensional hydrodynamical simulations of the canonical case of accretion from an initially uniform background gas in order to study the effects of adiabatic index, Mach number, resolution, and the size of the computational domain on the rates of accretion and drag. They found increasing accretion rates with increasing gas compressibility, decreasing accretion rates with increasing Mach number, and less stable flow and lower accretion rates with decreasing sink size.

3.2 Hydrodynamical Setup

We model BHL accretion onto a binary system moving with supersonic speed v_∞ relative to a uniform gas using FLASH [12], an Eulerian hydrodynamic code with adaptive mesh refinement (AMR). In our calculations, we use FLASH's directionally split Piecewise Parabolic Method

Riemann solver [28] and an ideal gas, gamma-law equation of state

$$P = (\gamma - 1)\rho e. \tag{3.1}$$

where γ is the adiabatic index and $\gamma = \gamma_1 = \gamma_3$ for an ideal gas. We initialize a 3D cartesian grid with the coordinate origin at its center. The size of the computational domain in x, y, and z is L, giving a domain volume of L^3.

We use the active sink particles (ASP) unit in FLASH [29] to model the binary system. We represent the binary with two point masses, m_1 and m_2, placed at positions $\mathbf{r}_1$ and $\mathbf{r}_2$ relative to the grid. We begin the simulations with the CM of the binary at rest ($\mathbf{V} = \mathbf{0}$) at the origin of the coordinate system ($\mathbf{R} = \mathbf{0}$). The two masses are initialized in a circular orbit in the $x - y$ plane with the orbital angular momentum vector pointing in the $+z$ direction. The initial values of m_1 and m_2 are determined by the binary mass ratio, $q = m_2/m_1$, chosen at runtime, and the total mass of the binary $M = m_1 + m_2 = (2G)^{-1}$, which is fixed. At the beginning of the simulation, m_1 and m_2 are placed at positions $\mathbf{r}_1 = -\frac{m_2}{M}a\hat{y}$ and $\mathbf{r}_2 = +\frac{m_1}{M}a\hat{y}$. They are given initial velocities $\mathbf{v}_1 = \mathbf{V}_1 = +\frac{m_2}{M}\left(\frac{GM}{a}\right)^{1/2}\hat{x}$ and $\mathbf{v}_2 = \mathbf{V}_2 = -\frac{m_1}{M}\left(\frac{GM}{a}\right)^{1/2}\hat{x}$, which are obtained by setting $r = a$, $R_1 = a_1$, and $R_2 = a_2$ in equations 2.21, as are the case for a circular orbit.

To model the supersonic motion of the binary relative to a uniform gas, we fill the domain with a homogenous wind of density ρ_∞ and adiabatic index γ that flows in the +x direction at speed v_∞. The wind speed is related to the sound speed, $c_{s,\infty}$, through the Mach number $\mathcal{M}_\infty = v_\infty/c_{s,\infty}$. In our code units, $v_\infty = 1$ and $\mathcal{M}_\infty$ is chosen at runtime. The initial gas pressure is set according to

$$P_\infty = \frac{\rho_\infty c_{s,\infty}^2}{\gamma} = \frac{\rho_\infty}{\gamma \mathcal{M}_\infty^2}. \tag{3.2}$$

An inflow boundary condition at the $-x$ boundary of the computational domain replenishes this homogenous wind throughout the simulation. All other boundaries of our computational domain

have an outflow condition, allowing gas to freely leave and enter the domain at those boundaries. With the choice of $v_\infty = 1$ and $M = (2G)^{-1}$, $R_a = 2GM/v_\infty^2 = 1$. The result is a dimensionless setup with length unit R_a and time unit R_a/v_∞. Although no BHL formalism exists for the case of a binary moving through a gas, this setup mirrors the single-particle numerical approach to BHL of MacLeod and collaborators [30, 31, 32] where now R_a is the accretion radius of the CM of the binary.

In all simulations, we use a domain of volume $L^3 = (32R_a)^3$. The CM of the binary is initialized at the center of the grids, which places each domain boundary a distance of $16R_a$ from the CM. The box is initialized with 4 blocks of 8^3 cells in the x, y, and z directions. Between 1 and 7 levels of refinement are adaptively applied, both at initialization and throughout the simulation. The finest grid cells are $\delta_{\mathrm{min}} = 0.016R_a$ wide in x,y, and z. The ASP unit automatically maximally refines the region of each sink particle, and we further instruct the AMR unit to refine on the internal energy of the gas.

3.3   Active Sink Particle Dynamics and Diagnostics

We utilize many of the ASP unit's built-in features and we have added some diagnostics. See Federrath et al. [29] for a complete description; we describe briefly our implementation here. We use two massive particles to represent our binary system. Each particle is a gravitationally softened point mass surrounded by a spherical inflow boundary of radius R_s. Once initialized, each particle moves freely along the grid, responding to gravitational accelerations due to the other particle and due to the gas in the grid. The inflow boundary, or sink, that surrounds each particle absorbs gas from the domain. Once material falls into the sink, it is added to the sink particle properties and then it is deleted. This boundary condition represents perfectly efficient accretion

without feedback. In our implementation of the ASP, we turn off the creation of new sink particles and we turn off self-gravity of the gas.

3.3.1 Accreted Quantities

The accreted gas carries with it mass and momentum, which are acquired by the particle. The accretion step is performed by integrating the quantity over all cells within the volume of the sink and by adding the summed values to the particle's properties. To compute an accretion rate, we simply divide each accreted quantity by the time step. The accretion rates are recorded, then the accreted gas is deleted by setting the density within the sink cells to a very small value, ρ_{sink}, and setting all components of the gas velocity to zero. The mass accretion rate for m_1 is calculated as

$$\dot{m}_1 = \frac{1}{\Delta t} \int_{\text{sink}_1} \left(\rho_i - \rho_{\text{sink}} \right) dV \tag{3.3}$$

and the mass accretion rate for m_2 is

$$\dot{m}_2 = \frac{1}{\Delta t} \int_{\text{sink}_2} \left(\rho_i - \rho_{\text{sink}} \right) dV. \tag{3.4}$$

The total mass accretion rate for the binary is $\dot{M} \equiv \dot{m}_1 + \dot{m}_2$.

The accretion of linear momentum is integrated in each cartesian coordinate. For m_1, this is given by

$$\dot{\mathbf{p}}_1 = \frac{1}{\Delta t} \int_{\text{sink}_1} \mathbf{v} \left(\rho - \rho_{\text{sink}} \right) dV \tag{3.5}$$

and

$$\dot{\mathbf{p}}_2 = \frac{1}{\Delta t} \int_{\text{sink}_2} \mathbf{v} \left(\rho - \rho_{\text{sink}} \right) dV \tag{3.6}$$

is the linear momentum accreted by m_2. The accreted linear momentum represents a force on each particle. We will denote these "momentum transport forces" on m_1 and m_2, respectively, as $\mathbf{F}_{\dot{p}_1}$ and

$\mathbf{F}_{\dot{p}_2}$. Then the total momentum transport force on the binary CM is

$$\mathbf{F}_{\dot{p}} = \mathbf{F}_{\dot{p}_1} + \mathbf{F}_{\dot{p}_2}. \tag{3.7}$$

3.3.2 Dynamical Friction

Each sink particle exerts a gravitational force on the gas, which restructures the gas in the domain. In turn, the redistributed gas exerts a gravitational force on each particle. This gravitational drag force, or gaseous dynamical friction (DF), will occur whenever the gas distribution is not spherically symmetric about the particle. The total (vector) DF force acting on each particle is found by summing up the gravitational force on the particle due to each cell in the domain. Recalling that $\mathbf{r}_1$ is the location of m_1 in the grid and letting $\mathbf{r}'$ denote the location of a particular gas cell, then the force on m_1 due to the cell is

$$d\mathbf{F}_{\mathrm{DF}_1} = -\frac{Gm_1\rho(\mathbf{r}')dV}{|\mathbf{r}_1 - \mathbf{r}'|^3}(\mathbf{r}_1 - \mathbf{r}') \tag{3.8}$$

and the total DF force on m_1 is the integral over the domain

$$\mathbf{F}_{\mathrm{DF}_1} = -\int_{\mathrm{domain}} \frac{Gm_1\rho(\mathbf{r}')dV}{|\mathbf{r}_1 - \mathbf{r}'|^3}(\mathbf{r}_1 - \mathbf{r}'). \tag{3.9}$$

Similarly, the DF force on m_2 is

$$\mathbf{F}_{\mathrm{DF}_2} = -\int_{\mathrm{domain}} \frac{Gm_2\rho(\mathbf{r}')dV}{|\mathbf{r}_2 - \mathbf{r}'|^3}(\mathbf{r}_2 - \mathbf{r}') \tag{3.10}$$

and the total DF force on the CM is

$$\mathbf{F}_{\mathrm{DF}} = \mathbf{F}_{\mathrm{DF}_1} + \mathbf{F}_{\mathrm{DF}_2}. \tag{3.11}$$

3.3.3 Particle Advancement

The CM position and CM velocity of each particle is updated to account for the accreted gas. Before the gas is evolved further, each particle's motion is advanced using ASP's Leap Frog

integrator. The advancement step applies the momentum transport, DF, and the sink-on-sink accel-

erations to each sink particle. Note that, in additional to the accretion rates and forces described so

far, the instantaneous total mass, position vector components, velocity vector components, and spin

angular momentum vector components of each particle are recorded during each time step.

3.4   Simulation parameters

To summarize, the free physical parameters of our numerical setup are the background

density ρ_∞, the flow Mach number $\mathcal{M}_\infty$, the adiabatic index γ, the mass ratio q, and the initial

semi-major axis of the binary a_0. All simulations in this paper set $\mathcal{M}_\infty = 2$, $\gamma = 5/3$, and $q = 1$. We

vary only the parameter a_0, simulating seven values of a_0/R_a: 0.0, 0.16, 0.3, 0.41, 0.55, 0.74, and

1.0. We report the results in chapter 4.

4

Numerical Results

4.1 Flow

The presence of a binary significantly alters the morphology of BHL accretion flows. At a given time, the manifestation of the binary's presence depends strongly on a_0. For a given a_0, the morphology of the gas structures depend on time (specifically, on orbital phase). We demonstrate these two aspects of BHL flows in figures 4.1, 4.3, and 4.4. In these figures, we show slices through the orbital ($z = 0$) plane. The initially-homogenous wind of density $\rho_\infty = 10$ and $\mathcal{M}_\infty = 2$ flows from left to right. The x and y axes are given in units of R_a and the steamlines follow the velocity field. We show only a portion of the computational domain; the full grid extends to $\pm 16 R_a$ in the x, y, and z directions.

4.1.1 Macroscopic Properties of the Flow

Figure 4.1 illustrates the effect of semi-major axis on flow morphology. Here we plot density (in units of ρ_∞) at $t = 40 R_a / v_\infty$ for our single-particle simulation (upper left) and for binary
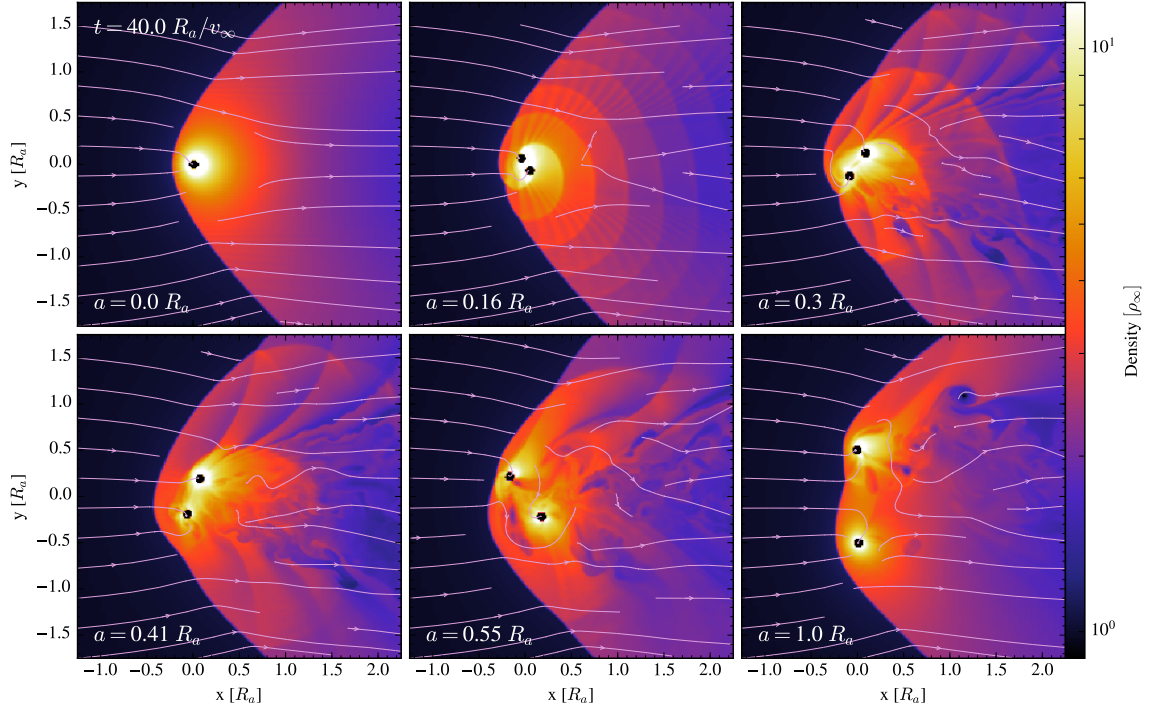
Figure 4.1: Comparison of binary flow morphology to single-particle BHL flow. Shown are density slices through the orbital ($z = 0$) plane in units of ρ_∞ at time $t = 40.0 R_\mathrm{a}/v_\infty$ with streamlines following the velocity field. The wind flows from left to right in these images. The axes are in units of $R_a = 2GMv_\infty^{-2}$, the accretion radius of the CM of the particle(s). These slices show the region of the orbiting pair; the full computational domain extends to $\pm 16 R_a$ in x, y, and z. The upper left snapshot shows BHL flow for a single particle of mass $M = (2G)^{-1}$. The remaining snapshots show the binary systems simulated, each with total mass $M = (2G)^{-1}$ but a different value of the initial semi-major axis, a_0. The images run from the smallest separation simulated ($a_0 = 0.16R_a$) to the largest ($a_0 = 1.0R_a$). The imprint of the binary on the shape of the overall shock front increases with a_0. The spiral shock waves appear less coherent for larger a, as the orbital period lengthens relative to the crossing time of the wind.

simulations with 5 different values of semi-major axis (namely, $a_0/R_a = 0.16, 0.3, 0.41, 0.55$, and

1.0). The total mass of each binary system is $M = (2G)^{-1}$. By also setting the mass of the single

particle to M, we have ensured that its accretion radius is the same as that of each binary system

simulated. In this way, we can think of the single particle as a binary with no separation ($a_0 = 0.0R_a$),

so figure 4.1 shows a series in a_0 from zero to $1.0R_a$.

The $a_0 = 0.0R_a$ snapshot of figure 4.1 illustrates key features of canonical BHL flow: the

supersonic motion sets up an upstream shock front that funnels material into a downstream wake;

the leading boundary layer separating the pre-shock region from the post-shock region is smooth

and axisymmetric about the line of motion of the point mass; the sink sits well within the standoff

distance of the shock; the density enhancement around the sink is smooth and axisymmetric; the

opening angle of the shock is proportional to $c_{s,\infty}/v_\infty$. With $a_0 = 0.16R_a$ (upper middle image), the

size and shape of the primary shock remains very similar to that of $a_0 = 0.0R_a$, though the opening

angle is broadened slightly from the additional pressure support that the orbiting binary provides.

Behind the primary shock, the presence of the binary is unmistakable. The spiral waves induced by

the orbital motion of the pair cause significant restructuring of the gas. In fact, these wave fronts can

be seen as slight divots in the leading edge of the primary shock. The divots grow more pronounced

with increasing a_0, as does the broadening of the opening angle of the shock. By $a_0 = 1.0R_a$, each

particle sets up its own primary shock (during parts of the orbit) and the overall structure is the

superposition of the two. Readily apparent in this snapshot is the lower density of the gas within

the orbit of the binary. The formally divergent potential at the origin (with $a_0 = 0.0R_a$) has been

replaced by a softened potential with a softening length of $\approx a_0/2$. The highest densities are found

nearest m_1 and m_2, but these densities are not as high as the material around M in the $a_0 = 0.0R_a$

snapshot. Now, we would not expect the densities to be the same since m_1 and m_2 have a mass of

$M/2$, but the longer orbital periods of wider binaries also give the finite sound speed and the finite wind speed more time to respond. The restructuring of the material in the wake has implications for the rates of accretion and drag, which we discuss in detail in sections 4.2 and 4.3. Although not conveyed by the stills of figure 4.1, the only simulation in steady-state is $a_0 = 0.0R_a$. The $a_0 = 0.0R_a$ simulation reaches steady-state in approximately the wind crossing time of the domain $\sim 30 R_a/v_\infty$, but the binaries never reach a steady-state. Instead, the gas structures vary throughout each orbit, meaning that we must discuss rates of accretion and drag in an orbit-averaged way. We will discuss the time dependent properties of the flow in section 4.1.2.

Behind the primary shock, supersonic orbital motion leads to the generation of secondary shocks near the orbiting particles. These structures can be seen in figure 4.2, where we plot the velocity divergence, $\nabla \cdot \mathbf{V}_{\text{gas}}$. The snapshots in this figure are otherwise identical to those of figure 4.1. Shocked material is revealed in purple in the figure, where $\nabla \cdot \mathbf{V}_{\text{gas}} < 0$ indicates the abrupt stagnation of gas. Especially pronounced for the binaries with $a_0 = 0.16R_a$ and $a_0 = 0.3R_a$, secondary shocks are induced ahead of both particles and these structures propagate downstream, contained within the primary wake. As the binary separation increases, the relative motion between each particle and the gas decreases. The particle moving through $-y$ positions transitions to subsonic relative motion first, since the particle in the lower half of the orbit moves in the same direction as the wind. This transition to subsonic relative motion is visible in the bottom row of the figure. In the $a_0 = 0.41R_a$ slice, the secondary shock ahead of the lower particle is just barely discernible. By $a_0 = 1.0R_a$ both secondary shocks are absent and the only inflection of the binary envelope is from the superposition of *two* primary shocks fronts, which have time to set up in response to the oblique potential of such widely separated particles with such a slow orbital period.

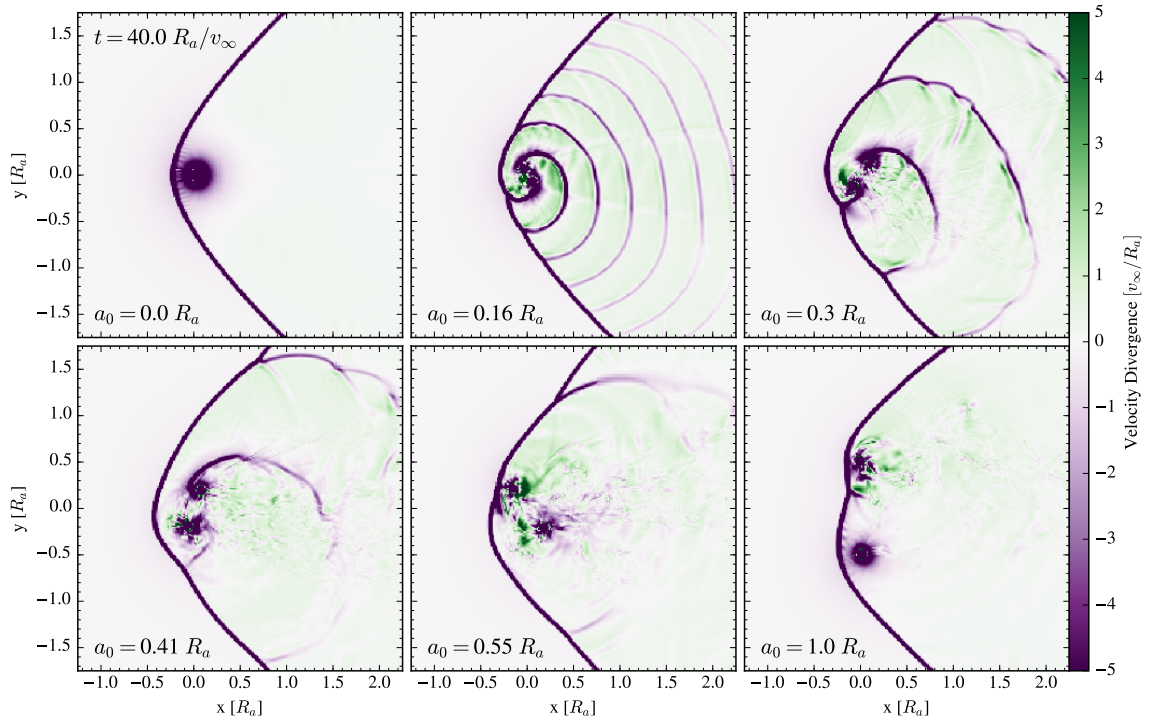Figure 4.2: Same as in figure 4.1, except that here we plot velocity divergence, $\nabla \cdot \mathbf{V}_{\text{gas}}$. Shades of purple highlight shocked material, where $\nabla \cdot \mathbf{V}_{\text{gas}} < 0$. Secondary shock fronts form ahead of particles in supersonic relative motion. The increasing orbital period with increasing a_0 means that the secondary shocks are absent by $a_0 = 1.0 R_a$.

4.1.2 Time-Dependent Properties of the Flow

The illusion of steady-state imparted by figures 4.1 and 4.2 is quickly dispelled by figures 4.3 and 4.4, in which we show time series of the flow for $a_0 = 1.0R_a$ and $a_0 = 0.41R_a$, respectively. As in figure 4.1, we show density slices (normalized to $\rho_\infty = 10$) of a $3.5R_a \times 3.5R_a$ section of the orbital plane. For reference, the simulation time is shown in the lower-left corner of each snapshot and we have marked m_1 with a blue dot and m_2 with a black dot. In both of these time series, we show the binary over half of an orbit only. The second half of each orbit is qualitatively similar to the first, except that the roles of m_1 and m_2 are reversed.

Figure 4.3 shows $a_0 = 1.0R_a$ over the half-orbit that begins at $t = 42.1\,R_a/v_\infty$. In the first image, m_1 is fully upstream from m_2, setting up a primary shock front which funnels material into a high density wake. Although at this instant the particles lie along a line parallel to the wind direction (at ∞), the primary shock is not symmetric about this line. Rather, the shape of the primary shock reflects the shape of the potential well at an earlier time. We will see this shape arise again as we follow the remaining snapshots. Situated downstream, m_2 interacts with material that has already been influenced by m_1. This dense, lower-velocity material piles up around m_2, resulting in a higher-than-average, and almost spherical, density distribution about m_2. This density enhancement remains with m_2 as time advances across row 1 of the figure, approaching the primary shock by the first image of the second row. At $t = 43.7\,R_a/v_\infty$, (first panel of the second row), a second shock front is forming ahead of m_2 as the particle approaches its greatest velocity relative to the gas. Between this snapshot and the next, m_2 crosses the leading boundary of the primary shock of m_1. The over-density that has been carried along by m_2 remains with the particle during the crossing. In the next two images ($t = 44.3$ and $44.8\ R_a/v_\infty$), we see that this material is suffering impingement by the incoming wind. By $t = 45.4\,R_a/v_\infty$ (first panel of third row), the over-density
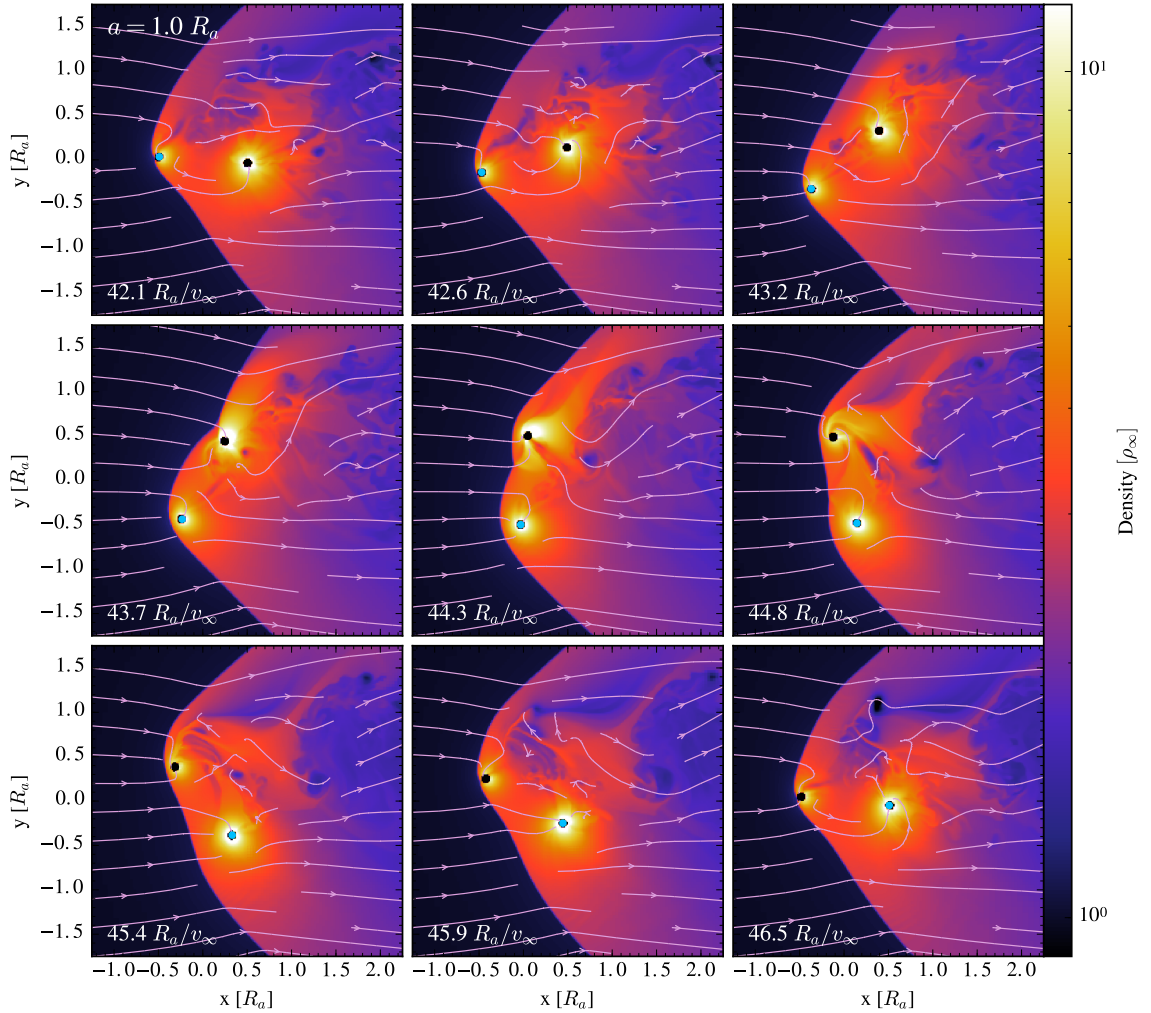
Figure 4.3: Flow morphology over half of an orbit for the $a_0 = 1.0 R_a$ simulation. As in figure 4.1, we show density slices through the orbital ($z = 0$) plane. Simulation times are printed in the lower left corner of each slice, given in our time units of R_a/v_∞. The particle we refer to as m_1 is blue, while the black particle is m_2. The overall shape of the primary shock front responds to the rotation of the oblique potential of two particles with finite separation. The density distribution about each particle is heavily influenced by the motion of the particle relative to the wind. In this series, m_1 moves in the $+x$ direction, as does the wind, so has a lower speed relative to the gas. m_2 moves in the $-x$ direction, head-on into the wind. The downstream particle interacts with material that has already interacted with its binary companion (see m_1 in the last two snapshots). As a particle moves into an upstream position, it will actually cross the primary shock front of its companion (see m_2 in the $t = 43.7$ and $44.4 R_a/v_\infty$ snapshots, for example). As a result, the accretion rates and forces show tremendous time-variability.

is largely detached from m_2 and is being pulled into the approaching potential well of m_1. In the same panel, a bridge of material connects the two particles and, for the first time in these snapshots, the density enhancement about m_1 is greater than that of m_2. Several things occur in the last row of the figure. First, the dense material that is attached to m_2 at $t = 45.4\,R_a/v_\infty$ becomes fully detached from the particle as the downstream region is increasingly dominated by the gravitational pull of m_1. Second, as m_2 moves down and to the left, the shock set up by the particle turns with it, giving a slightly hooked appearance to the primary shock. This asymmetry is accentuated by the lower half of the primary shock, which is shifted to the right under the gravitational influence of m_1.

Figure 4.4 shows the $a_0 = 0.41 R_a$ binary for the half-orbit beginning at $t = 40.1\,R_a/v_\infty$. As in figure 4.3, m_1 is marked by a blue dot and m_2 is marked by a black dot. Behind the primary shock, the gas is unable to adjust within the orbital period of the binary, so significant restructuring of the gas occurs. As discussed in the context of figure 4.2, at any given time the particle moving through $+y$ values travels head-on into the wind, setting up a secondary shock in front of the particle. The creation of these secondary shocks and the orbital speed of the binary are responsible for the fan-like structures emanating from the binary behind the primary shock. Material crossing the primary shock interacts with each particle twice, resulting in four fan structures per orbit. In the upper left snapshot ($t = 40.1\,R_a/v_\infty$), the particles are located at $x \approx 0$. There is a large stand-off distance between the primary shock and the binary. Behind the primary shock, a secondary shock is set up in front of m_1. We label these structures "1" and "2", respectively, in all of the snapshots shown, so that one can follow each structure over time. From $t = 40.2$ to $40.3\,R_a/v_\infty$, shock 1 is deflected due to the gravitational pull of m_1. By $t = 40.4$, shock 2 is pushed past shock 1 by m_1 as the particle advances in the $-x$ direction. Throug $t = 40.6$ and $40.8\,R_a/v_\infty$, the bend in shock 1 is stretched as the structure expands at the sound speed. By $t = 41.0\,R_a/v_\infty$, m_2 has advanced to $+y$ values and shock
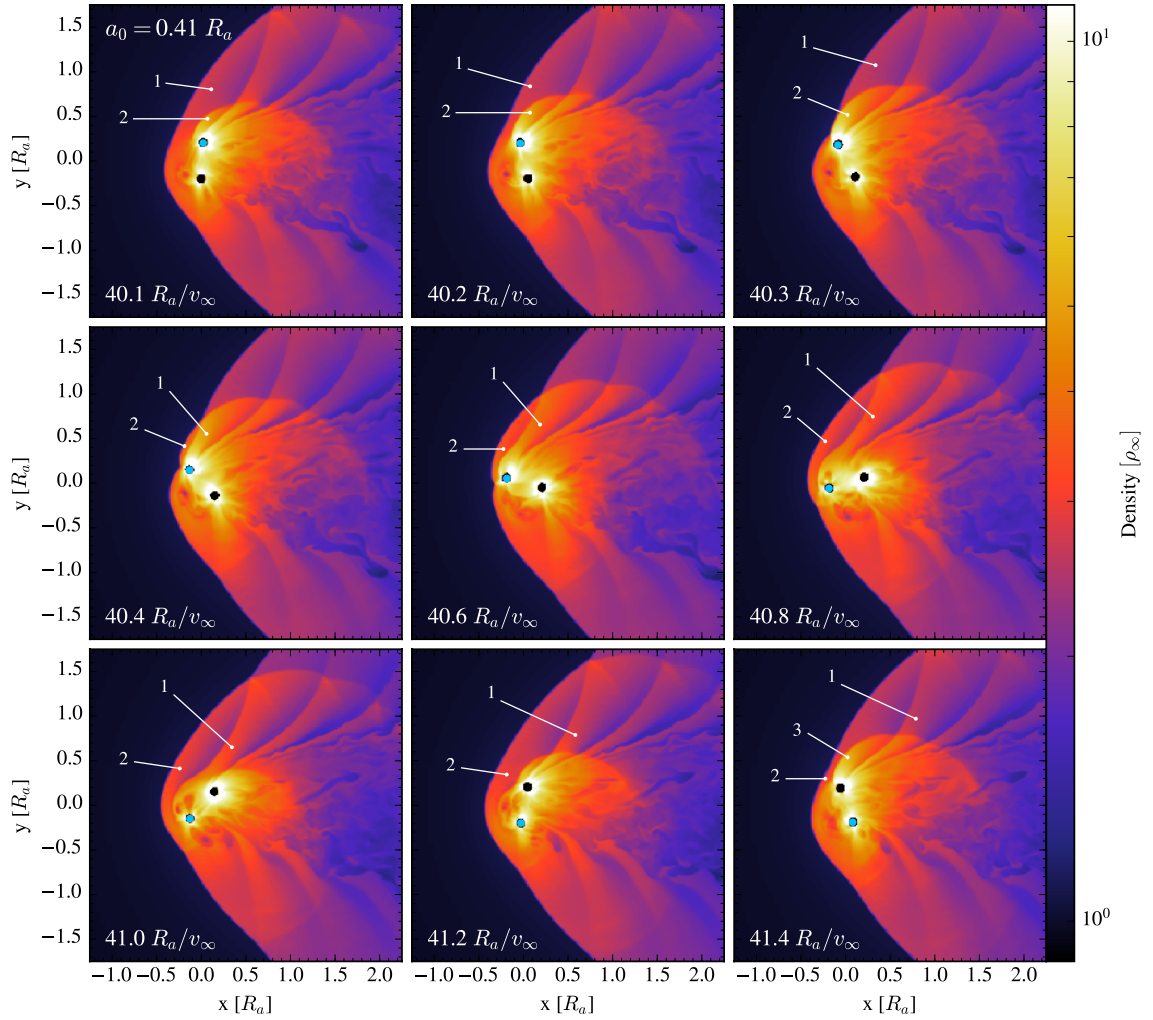
Figure 4.4: Same as in figure 4.3, but for the $a_0 = 0.41R_a$ simulation. The persistent density structures behind the primary shock reflect the quick orbital speed of the binary. Material cannot advect faster than the binary period and so encounters each particle repeatedly. The curved fan structures arise four times each orbit. Each particle crosses the shock it set up one orbit before, then crosses the primary shock set up by its companion a half-orbit before. The hook in each fan blade is created by the gravitational pull of the particle just before the particle crosses the material. Each fan structure expands outward ($\pm y$ direction) while also being advected downstream. The fan structures are more pronounced in the upper half of each slice due to the greater relative motion of the particle moving through the upper half of the orbit.

1 is defected yet further, now by the gravitational pull of m_2. At $t = 41.2\,R_a/v_\infty$, a new secondary shock (that was set up by m_2 and labeled "3" in the figure) crosses shock 1 as shock 1 continues to advect downstream. In the final image, shock 3 is advancing to meet shock 2, and will cross shock 2 as the orbit continues. In addition to the fan structures, the density very close to the binary is of interest. In particular, it appears that the particle at $+y$ positions exhibits a higher density local density than its counterpart at $-y$ values. A persistent bridge of dense material always connects the two particles giving a slightly higher density enclosed by the orbit than in the $a_0 = 1.0R_a$ simulation.

4.2 Accretion

4.2.1 Instantaneous Accretion Rates

In figure 4.5, we plot the instantaneous accretion rates versus time for $a_0 = 0.16, 0.41,$ and $1.0R_a$ for simulation times $\geq 30\,R_a/v_\infty$. The y axis shows the instantaneous accretion rate in units of $\dot{M}_{BH}$ (equation 2.8). In each panel of the figure, we plot $\dot{m}_1$ in blue and $\dot{m}_2$ gray, which are calculated according to equations 3.3 and 3.4, respectively. The black curve is the total accretion rate for the binary, $\dot{M} = \dot{m}_1 + \dot{m}_2$. On each panel, we include a pink line segment indicating the length of the orbital period of the binary, P_{orb}[1]. The dashed line across all panels shows the steady-state value of $\dot{M}(a_0 = 0)$, the accretion rate for our single-particle simulation. As expected from prior studies of canonical BHL accretion (with $R_s = 0.05R_a$, $\mathcal{M}_\infty \sim 2$, and at our resolution), $\dot{M}(a_0 =$

---

[1]The orbital period squared is

$$P_{\text{orb}}^2 = \frac{4\pi^2 a^3}{GM} = \frac{8\pi^2 a^3}{R_a v_\infty^2}$$

where we have eliminated GM with the expression for the accretion radius $R_a = 2GM/v_\infty^2$. Then if we simply plug in a in our length units of R_a, we obtain P_{orb} in our time units, R_a/v_∞. As an example, for the $a_0 = 0.41R_a$ binary

$$P_{\text{orb}} = \sqrt{\frac{8\pi^2(0.41R_a)^3}{R_a v_\infty^2}} = 2.33\,R_a/v_\infty.$$
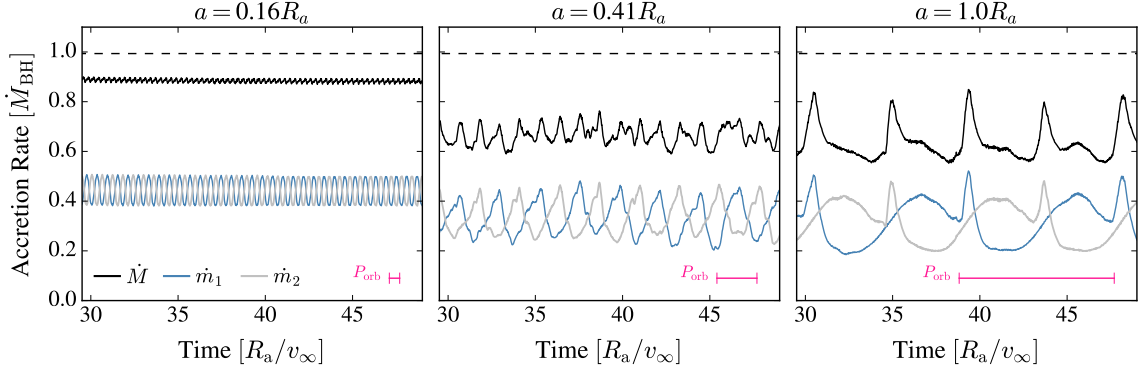
Figure 4.5: Instantaneous accretion rates over time for the binaries with $a_0 = 0.16R_a$ (left panel), $a_0 = 0.41R_a$ (center panel), and $a_0 = 1.0R_a$ (right panel). The individual accretion rates, $\dot{m}_1$ and $\dot{m}_2$, are plotted in blue and gray, respectively. The total rate of accretion, $\dot{M} = \dot{m}_1 + \dot{m}_2$, is plotted in black. The orbital period of each binary is included for reference as a pink line segment. On each panel, the dashed line indicates the steady-state accretion rate realized in the single-particle simulation, $a_0 = 0.0R_a$. The individual accretion rates for the $a_0 = 0.16R_a$ binary sum to an almost constant value, while the total accretion rates for $a_0 = 0.41R_a$ and $a_0 = 1.0R_a$ exhibit significant time variability. The wider binaries experience lower accretion rates than the tightest binary, whose total accretion rate approaches that of the single particle simulation.

$0) \approx 0.7\dot{M}_{\mathrm{HL}} \approx 1.0\dot{M}_{\mathrm{BH}}$ [17, 14].

Although $\dot{M}(a_0 = 0)$ reaches a steady state, the accretion rates for the members of the binary systems are periodic. For the tightest binary, $a_0 = 0.16R_a$ (left panel of figure 4.5), $\dot{m}_1$ and $\dot{m}_2$ are exactly out of phase, each with an accretion rate that follows the orbital period. As such, $\dot{M}$ is almost constant in time and approaches $\dot{M}(a_0 = 0)$. For more widely separated binaries, the individual accretion rates of the two particles no longer sum to a constant value. In the case of $a_0 = 1.0R_a$ (right panel of 4.5), $\dot{m}_1$ shows a sharp spike once per orbit before declining to a minimum value, then the rate climbs to a local maxima before the next sharp spike in accretion. While the curve for $\dot{m}_2$ looks very similar, the variation in $\dot{M}$ reveals that the individual accretion rates are not exactly out of phase. Of note is the difference in $\dot{M}$ over each half-orbit. Rather than being identical, every other peak in $\dot{M}$ is higher than the one that follows it and the curves connecting neighboring peaks vary in shape from one orbit to the next. This suggests that some features of
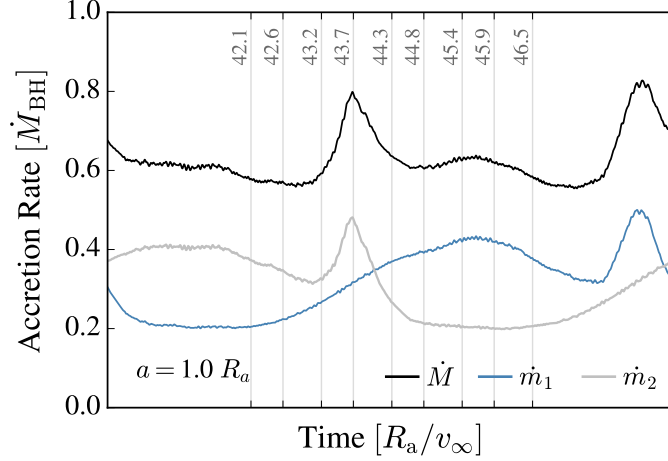
Figure 4.6: As in the right panel of figure 4.5, instantaneous accretion rates are shown for the $a_0 = 1.0R_a$ binary. Here we focus on one orbit of the binary, which begins at $t = 39.9\,R_a/v_\infty$. Each vertical gray line corresponds to one of the density snapshots of figure 4.3 and we have listed the simulation time next to each line to enable connection between the two figures. Colors are the same as in figure 4.5. Note that $\dot{m}_1$ is in blue to match the color of the particle in the density slices.

the flow are operating on their own timescales not synced with the orbital period. In the case of $a_0 = 0.41R_a$ (middle panel of 4.5), the individual accretion rates reveal one peak and one valley per orbit with transitions between the two that appear to vary from one orbit to the next. In addition, $\dot{m}_1$, for example, reveals a slight overall increase and decrease over many orbits. The superposition of these trends in $\dot{m}_1$ and $\dot{m}_2$ yields an $\dot{M}$ that has irregularly spaced peaks and valleys with significant variation from orbit to orbit. Let us connect features of the accretion rates depicted in figure 4.5 to the flow morphology discussed in section 4.1.2. In figures 4.6 and 4.7 we repeat the accretion rate time series for $a_0 = 1.0$ and $0.41R_a$, respectively, except that we now restrict the x axis of each figure to highlight the simulation times depicted in the density slices of figures 4.3 and 4.4, respectively. We discuss each set in turn.

In figure 4.6, we show $\dot{m}_1$, $\dot{m}_2$, and $\dot{M}$ for the $a_0 = 1.0R_a$ simulation for simulation times $t = 39.9$ to $48.7\ R_a/v_\infty$. As in figure 4.5, $\dot{m}_1$ is in blue, $\dot{m}_2$ is in grey, and $\dot{M}$ is in black. The vertical gray lines (labeled with the simulation time) correspond to the nine density slices of figure 4.3.
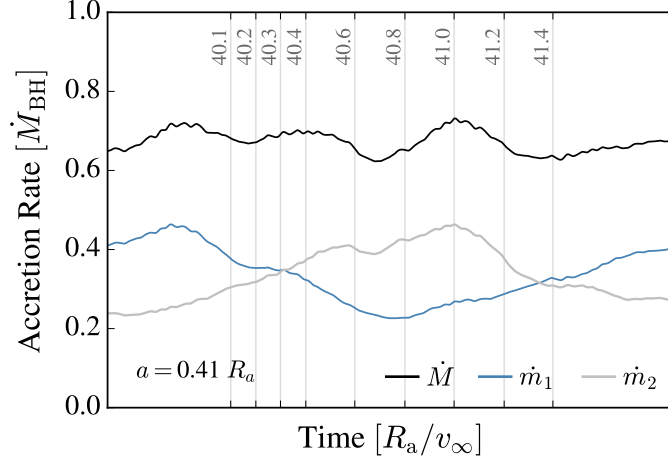
Figure 4.7: Instantaneous accretion rates for the $a_0 = 0.41R_a$ binary for a single orbit, beginning at $t = 39.6 R_a/v_\infty$. Each vertical gray line corresponds to one of the density snapshots of figure 4.4 and we have listed the simulation time next to each line to enable connection between the two figures. Colors are as in figure 4.6.

Recall that m_1 is also in blue in figure 4.3. In the first row of figure 4.3, m_2 moves from a position directly downstream from m_1 at $t = 42.1 R_a/v_\infty$ into a lower-density pocket behind the primary shock by $t = 43.2 R_a/v_\infty$. Figure 4.6 reveals a decreasing accretion rate for m_2 during the same period of time. Although m_2 has carried along higher-density material during this time interval, the material is able to expand into the low-density region behind the primary shock, giving rise to the local mimimum in $\dot{m}_2$ at $t \approx 43.2 R_a/v_\infty$. Between $t = 43.2$ and $43.7 R_a/v_\infty$, m_2 has turned into the oncoming wind and approaches the primary shock front. As noted in section 4.1.2, m_2 reaches its highest velocity relative to the gas at $t = 43.7 R_a/v_\infty$ and a second shock front forms in front of m_2. Meanwhile, the high-density clump that has followed m_2 is now stopped by this second shock and a stream of material flows from m_1 to m_2. Indeed, this confluence of flow gives $\dot{m}_2$ a sharp peak at $t = 43.7 R_a/v_\infty$. By $t = 44.3 R_a/v_\infty$, m_2 has crossed the primary shock of m_1, and now $\dot{m}_2$ declines. From $t = 44.3$ to $44.8 R_a/v_\infty$, m_2 begins to lose the high-density clump that has followed the particle since its time downstream from m_1. $\dot{m}_2$ bottoms out as the clump of material finally detaches from

m_2 and is swept down stream ($t = 45.4$ to $46.5 R_a/v_\infty$). At the same time, m_1 is moving into a position downstream from m_2. There is an increase in $\dot{m}_1$ from $t = 44.3$ to $45.9 R_a/v_\infty$ as m_1 begins to pull material from m_2. From 45.9 to 46.5, $\dot{m}_1$ declines slightly as the clump of material that has detached from m_2 crosses outside of the orbit of m_1 as it is advected downstream and out of reach.

Figure 4.7 shows the accretion rates for the $a_0 = 0.41 R_a$ simulation for the time period $t = 39.6$ to $t = 41.9 R_a/v_\infty$. Colors are the same as in figure 4.6, but now the vertical gray lines corresponding to the density slices of figure 4.4. From $t = 40.1$ to $40.8 R_a/v_\infty$, $\dot{m}_2$ steadily increases as m_2 moves in the same direction as the flow. At $40.8 R_a/v_\infty$, m_2 turns upstream. There is a steepening of $\dot{m}_2$ to a maximum at $41.0 R_a/v_\infty$ as m_2 deflects shock 1 while also stripping material from the region surrounding m_1. Between 41.0 and 41.2 R_a/v_∞, shock 3 forms in front of m_2. Once this material crosses shock 1 (at $41.2 R_a/v_\infty$), it expands into the lower density region behind shock 2, reducing the rate of accretion onto m_2. Meanwhile, m_1 experiences a decreasing accretion rate from $t = 40.1 R_a/v_\infty$ to $t = 40.8 R_a/v_\infty$ as the particle takes up a position in front of m_2. There is a flattening of $\dot{m}_1$ from $t = 40.2$ to $40.3 R_a/v_\infty$ when shock 1 is pulled into m_1 and shock 2 crosses shock 1. The overall decrease in $\dot{m}_1$ continues through $t = 40.8 R_a/v_\infty$ while m_1 is in the upstream position and m_2 pulls material away from m_1. Just before $t = 40.8 R_a/v_\infty$, the slope of $\dot{m}_1$ turns positive as m_1 moves to $-y$ values. There, m_1 moves in the same direction as the wind, reducing the relative motion between the particle and the gas. From there the cycle depicted in Figure 4.4 begins again, but this time with the roles of m_1 and m_2 reversed.

4.2.2   Orbit-Averaged Accretion Rates

It is apparent from figure 4.5 that the three accretion rates $\dot{m}_1$, $\dot{m}_2$, and $\dot{M}$ for $a_0 = 0.41$ and $1.0 R_a$, are always lower than the corresponding accretion rates in the $a_0 = 0.16 R_a$ case. To look
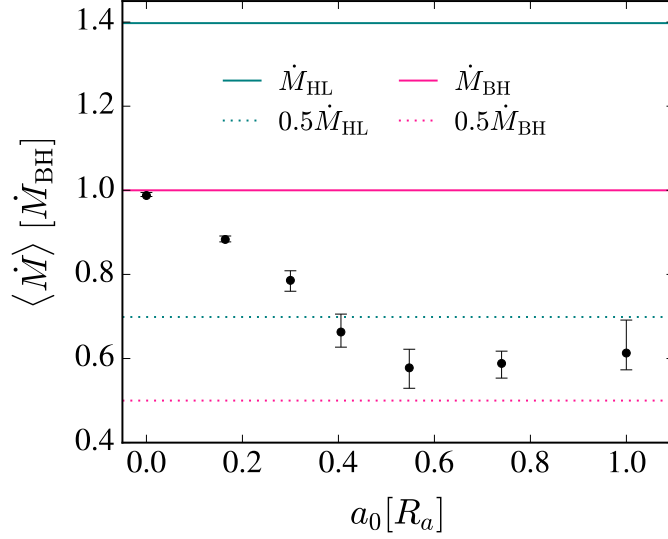
Figure 4.8: Orbit-averaged total accretion rate, $\langle \dot{M} \rangle$, in units of $\dot{M}_{BH}$ versus a_0, in units of R_a. The black points show the median of $\dot{M}(t)$ for each binary over an integer number of orbits between $t = 30\,R_a/v_\infty$ and $t = 50\,R_a/v_\infty$. The error bars show the 15.87th to 85.13th percentile range about the median. The solid pink line is $\dot{M}_{BH} = 4\pi G^2 M^2 \rho_\infty (v_\infty^2 + c_{s,\infty}^2)^{-3/2}$. The mass dependence of $\dot{M}_{BH}$ is proportional to $M^2 = (m_1 + m_2)^2$. The dashed pink line is $\dot{M}_{BH,\text{independent}} = 0.5\dot{M}_{BH}$, which has mass dependence $\propto (m_1^2 + m_2^2)$. At smaller separations, the accretion rate approaches that of a single particle with $\langle \dot{M} \rangle \approx \dot{M}_{BH} \propto M^2$, while at larger separations, the accretion rate approaches that of two independent particles with $\langle \dot{M} \rangle \approx \dot{M}_{BH,\text{independent}}$. Analogous to the pink line, but written in the HL formalism instead, the solid green line is $\dot{M}_{HL}$ and the dotted green line is $0.5\dot{M}_{HL}$.

for trends in the accretion rate as a function of a_0, let us compare the time averaged total accretion rate for each pair. The temporal variation of the accretion rate due to the orbital motion of the binary requires that any time average we compute be taken over an integer number of orbits. We use angled brackets, $\langle\,\rangle$, to indicate such orbit-averaged quantities. In general, each time average begins at $t = 30\,R_a/v_\infty$ and terminates at the end of the last complete orbit before the end of the simulation ($t = 50\,R_a/v_\infty$). The $a_0 = 1.0R_a$ binary (with $P_{\text{orb}} \approx 8.89\,R_a/v_\infty$) completes two complete orbits during this time. The $a_0 = 0.16R_a$ binary completes 33. In figure 4.8, we plot the orbit-averaged total accretion rate, $\langle \dot{M} \rangle$, for each binary system simulated versus the binary's initial semi-major axis, a_0. The black points are the median values of $\dot{M}$ and the error bars give the 15.87th to 85.13th percentile spread about the median over the time interval used to compute the median. For the

$a_0 = 0.0R_a$ simulation, the median and error bars are instead computed using the times $t = 30$ to $t = 50R_a/v_\infty$. We have normalized the y axis to $\dot{M}_{BH}$. We include the pink solid line at $\langle \dot{M} \rangle$ to highlight the accretion rate predicted by BH theory. As the binary separation decreases, $\langle \dot{M} \rangle$ approaches the pink solid line. According to equation 2.8, this says that $\dot{M}_{BH} \propto M^2 \propto (m_1 + m_2)^2$. That is, binaries of smaller separations accrete like a single particle of mass $m_1 + m_2$. Wider binaries, on the other hand, have a lower accretion rate and fall between the two dotted lines. The pink dotted line at $\langle \dot{M} \rangle = 0.5\dot{M}_{BH}$ assumes that m_1 and m_2 accrete independently of one another. To see where the factor of 0.5 comes from, let us write the BH accretion rate for $m_1 = M/2$:

$$\dot{M}_{BH,1} = \frac{4\pi G^2 m_1^2 \rho_\infty}{(v_\infty^2 + c_{s,\infty}^2)^{3/2}} = \frac{4\pi G^2 (M/2)^2 \rho_\infty}{(v_\infty^2 + c_{s,\infty}^2)^{3/2}} = \frac{1}{4}\dot{M}_{BH}. \tag{4.1}$$

Since $m_2 = M/2 = m_1$, $\dot{M}_{BH,2} = \dot{M}_{BH,1}$. Then the total accretion rate for the pair (treating them as independent particles) is $\dot{M}_{BH,independent} = 0.25\dot{M}_{BH} + 0.25\dot{M}_{BH} = 0.5\dot{M}_{BH}$. For more general m_1 and m_2, we would say that since $\dot{M}_{BH,1} \propto m_1^2$ and $\dot{M}_{BH,2} \propto m_2^2$, $\dot{M}_{BH,independent} \propto (m_1^2 + m_2^2)$. Returning to figure 4.8, the simulated binaries with larger a_0, fall closer to $0.5\dot{M}_{BH}$. At arbitrarily large separation, we would expect this trend to continue so that the binary accretes like two independent particles with $\langle \dot{M} \rangle \propto (m_1^2 + m_2^2)$. The solid and dotted green lines are analogous to the solid and dotted pink lines, but in the HL formalism instead. The fact that $\langle \dot{M} \rangle$ does not fall directly to $0.5\dot{M}_{BH}$ tells us that the hydrodynamics are important for transitional ($a \approx R_a$) binaries. The $a_0 = 0.55, 0.74$, and $1.0R_a$ binaries exhibit very different flow morphology than the smaller a_0 pairs. The orbital motion of the particles, the finite sound speed of the gas, and the speed of incoming wind all play a part in the instantaneous and orbit-averaged accretion rates. It is in this transition that the particles begin creating their own primary shocks. The binaries also transition from having intervals of supersonic orbital motion (relative to the gas behind the primary shock) to having orbital velocities that are always subsonic.

4.3   Forces

The presence of a binary restructures the distribution of the gas about its CM. The orbital motion of the binary adds a time-dependence to the shape of the potential well, causing the morphology of the flow to change as a function of time - especially on a_0 scales. In turn, the restructured gas exerts time-dependent forces on the two particles. In the case of a single-particle, the force vectors due to gaseous DF and due to momentum accretion are always antiparallel or parallel (respectively) to $\mathbf{V}$. Therefore, the DF force always represents a drag on the translation motion of the point-mass and momentum accretion gives the particle a small thrust. In the case of a binary, on the other hand, the velocity vectors of the two particles change direction throughout the orbit. The time-dependence of the local flow complicates matters even more because the directions of the forces themselves are always changing. To understand how the forces influence the translational motion of the CM and the orbital motion of the binary about the CM requires numerical calculation. In this section, we discuss how these force projections are calculated from our numerical simulations and we show an example calculation for our $a_0 = 0.41R_a$ simulation. The question of the longterm evolution of the binary is better answered in terms of timescales. In section 4.4, we calculate the timescale for accretion as well as the timescales for decay of the translation and orbital motion for each of our simulations. The reader may skip to section 4.4 if the details of the forces are not of interest.

4.3.1   Forces on the Center-of-Mass

First, let us consider how the forces change the translational motion of the binary CM. At each time step, we calculate the DF and momentum transport forces acting on each particle. The DF forces on m_1 and m_2 are given by equations 3.9 and 3.10, respectively, while the momentum transport forces are calculated according to equations 3.5 and 3.6. We can ask how these forces

influence the motion of the CM by considering the component of each force along the CM velocity relative to the gas. The velocity of the CM relative to the grid is $\mathbf{V}$ and the velocity of the wind relative to the grid is $\mathbf{v}_\infty = v_\infty \hat{x}$, so the velocity of the CM relative to the gas is $\mathbf{V}_{\text{rel}} = \mathbf{V} - \mathbf{v}_\infty$. Letting $\hat{V}_{\text{rel}}$ be the unit vector in the direction of $\mathbf{V}_{\text{rel}}$, the scalar component of the DF and momentum transport forces along $\mathbf{V}_{\text{rel}}$ are, respectively,

$$F_{\text{DF,CM}} \equiv \left(\mathbf{F}_{\text{DF}_1} + \mathbf{F}_{\text{DF}_2} \right) \cdot \hat{V}_{\text{rel}} \tag{4.2}$$

and the momentum transport force on the CM is

$$F_{\dot{p},\text{CM}} \equiv \left(\mathbf{F}_{\dot{p}_1} + \mathbf{F}_{\dot{p}_2} \right) \cdot \hat{V}_{\text{rel}}. \tag{4.3}$$

Notice that $F_{\text{df,CM}}$ and $F_{\dot{p},\text{CM}}$ may be positive or negative. A positive value indicates a net thrust while a negative value exerts a net drag. The total drag (or thrust) on the CM is the sum of the two projections

$$F_{\text{net,CM}} = F_{\text{DF,CM}} + F_{\dot{p},\text{CM}}. \tag{4.4}$$

Figure 4.9, shows the forces on the CM of the $a_0 = 0.41 R_a$ binary from $t = 30 R_a$ until the end of the simulation. The top panel shows the DF forces on the CM (equation 4.2). The contribution due to m_1, which is $\mathbf{F}_{\text{DF}_1} \cdot \hat{V}_{\text{rel}}$, is shown in blue. The contribution from m_2, which is $\mathbf{F}_{\text{DF}_2} \cdot \hat{V}_{\text{rel}}$ is shown in grey. The periodic modulation of the blue and grey curves is due to the orbital motion of each particle. Even though the density structure at large scales is relatively stable, the position of each particle relative to the gas distribution changes as the particles complete each orbit. This gives rise to a changing magnitude of the force vectors themselves ($\mathbf{F}_{\text{DF}_1}$ and $\mathbf{F}_{\text{DF}_2}$) as well as a modification of the angle between each force vector and $\hat{V}_{\text{rel}}$. In both cases, the values of the dot products in equation 4.2 change as a function of orbital phase. In the same panel, $F_{\text{DF,CM}}$ (in black) also shows variation due to the orbital motion about a nearly constant value of -4.2 F_{BH}. This
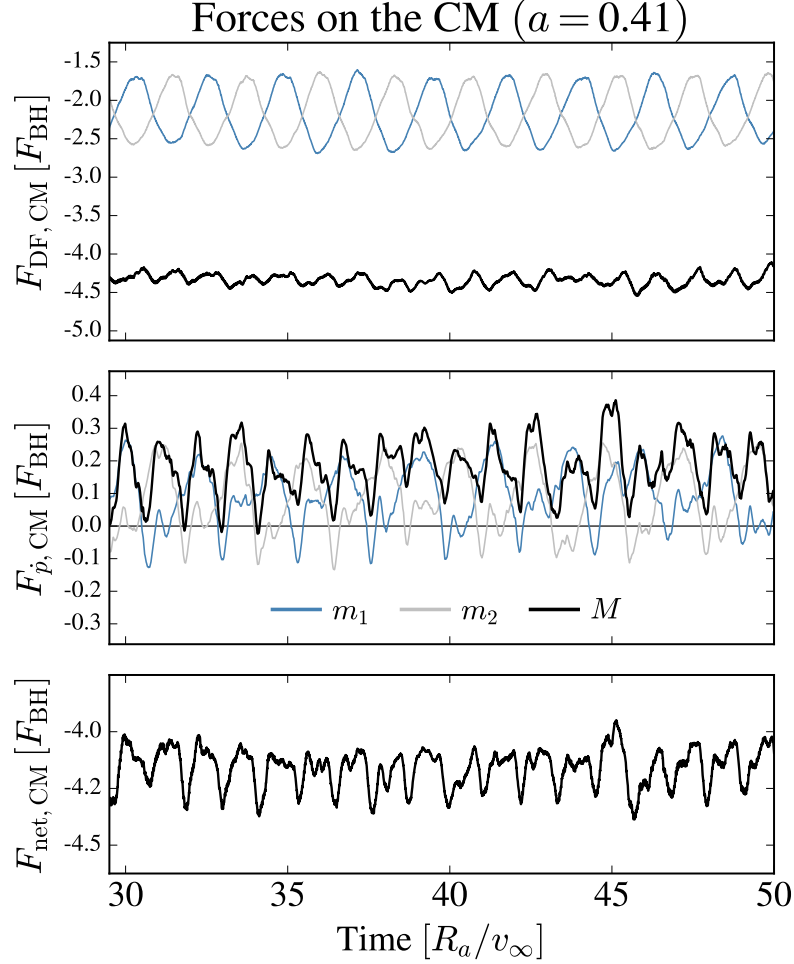
Forces on the CM ($a = 0.41$)

Figure 4.9: Center of mass forces over time for the $a_0 = 0.41 R_a$ binary. In the upper and middle panels, we show the DF and momentum transport forces, respectively, acting along the CM velocity vector relative to the wind, $\hat{V}_{\text{rel}}$. The blue and grey curves show the contributions from m_1 and m_2, respectively, to the total of each type of force (black curve). The bottom panel in the figure is the total force on the CM due to both DF and momentum transport. In each panel, a positive value indicates a net thrust of the CM while a negative value indicates a net drag on the CM. See the text for how these force projections are calculated. The DF force arising from the downstream wake dominates the total force on the CM of the binary. At all times, this net drag force acts to slow down the translational motion of the CM relative to the background gas.

negative value indicates that the large scale structure always exerts a drag on the CM motion of the pair, though by a lesser amount than the single-particle value of -5.1 F_{BH}.

Analogous to the top panel, the center panel of figure 4.9 shows the momentum transport forces acting along the CM motion of the binary, which are calculated according to equation 4.3. The blue and grey curves show $\mathbf{F}_{\dot{p}_1} \cdot \hat{V}_{\mathrm{rel}}$ and $\mathbf{F}_{\dot{p}_2} \cdot \hat{V}_{\mathrm{rel}}$, respectively. The black curve is the sum, $F_{\dot{p},\mathrm{CM}}$. The blue and grey curves dip to negative values when accreted material is moving opposite the motion of the particle. Their sum is always positive, though, so the momentum transport force always exerts a net thrust on the CM. This is similar to the single-particle case, although the median value of $|F_{\dot{p},\mathrm{CM}}| \approx 0.18\ F_{\mathrm{BH}}$ is 74% less than the magnitude of the single-particle value of 0.69 F_{BH}. Finally, the bottom panel of figure 4.9 shows the net force on the CM, given by equation 4.4. The combination of DF and momentum transport forces always exerts a drag on the CM. The orbit-averaged net force on the CM for the $a_0 = 0.41 R_a$ binary is -4.06 F_{BH}, a value that is only 7% lower in magnitude than in the single-particle case.

4.3.2 Forces on the Orbital Motion

Now, we consider the forces effecting the motion of the binary *about* the CM. To do this, we find the projections of the forces along the barycentric velocity vectors of the two particles. The barycentric velocities of m_1 and m_2 are $\mathbf{V}_1$ and $\mathbf{V}_2$, respectively (equations 2.18). The unit vectors in the directions of these velocities are then $\hat{V}_1 = \mathbf{V}_1/V_1$ and $\hat{V}_2 = \mathbf{V}_2/V_2$. The DF force on the orbital motion of the binary is

$$F_{\mathrm{DF,orb}} \equiv \mathbf{F}_{\mathrm{DF}_1} \cdot \hat{V}_1 + \mathbf{F}_{\mathrm{DF}_2} \cdot \hat{V}_2 \qquad (4.5)$$

and the momentum transport force on the orbit is

$$F_{\dot{p},\mathrm{orb}} \equiv \mathbf{F}_{\dot{p}_1} \cdot \hat{V}_1 + \mathbf{F}_{\dot{p}_2} \cdot \hat{V}_2, \qquad (4.6)$$
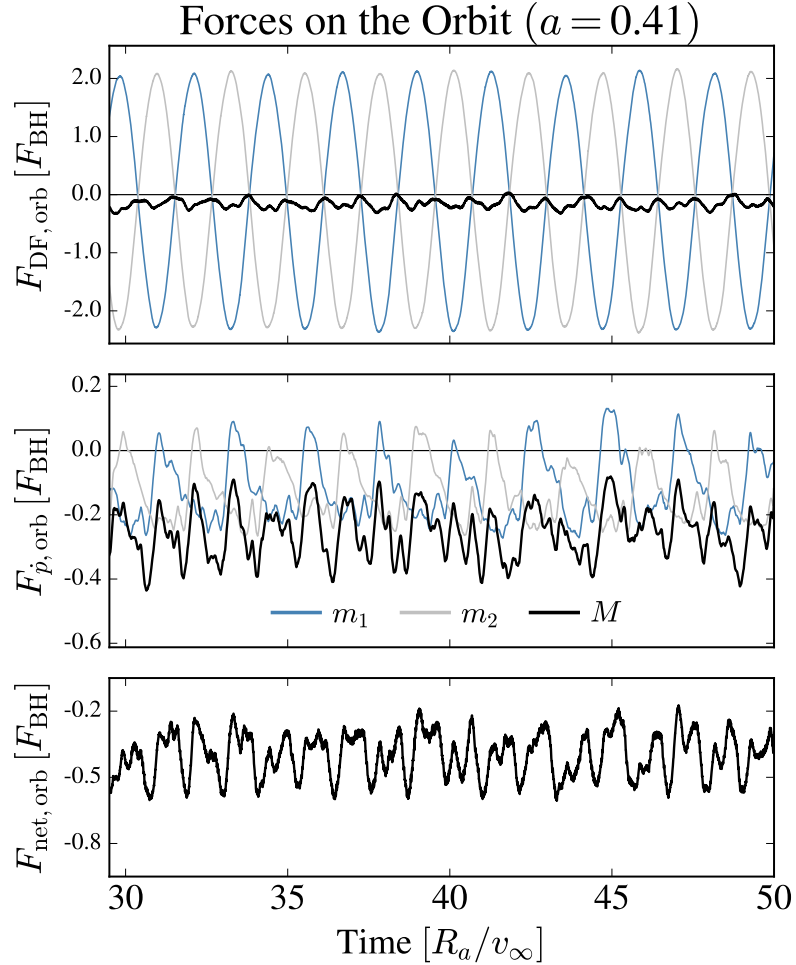
Figure 4.10: Orbital forces over time for the $a_0 = 0.41R_a$ binary. As in figure 4.9, the upper, middle, and lower panels correspond to the DF, momentum transport, and net force, respectively, on the binary over time with blue and grey curves representing the contributions to the total from m_1 and m_2, respectively. Here we plot instead the projections of the forces along the barycentric velocities of m_1 and m_2. Both DF and momentum transport cause a net drag on the orbital motion at all times. Momentum transport and DF contribute almost equally to the overall drag on the motion. The flow at small scales in the vicinity of the orbiting binary cannot be neglected, as momentum accretion contributes nearly half of the overall drag on the orbital kinetic energy of the binary.

which gives a net "orbital" force of

$$F_{\text{net,orb}} = F_{\text{DF,orb}} + F_{\dot{p},\text{orb}}. \tag{4.7}$$

In figure 4.10, we show these orbital forces calculated for $a_0 = 0.41 R_a$. As in figure 4.9, blue curves represent the contributions from m_1, gray curves the contributions from m_2, and black curves the total for the pair. In the upper panel, we show the realization of equation 4.5. The blue and gray curves, which are $\mathbf{F}_{\text{DF}_1} \cdot \hat{V}_1$ and $\mathbf{F}_{\text{DF}_2} \cdot \hat{V}_2$, respectively, show a sinusoidal fluctuation between large negative and positive values. Because the overdense wake located at positive x values remains the primary driver of DF forces, this periodic change in the sign of $F_{\text{DF,orb}}$ reflects the changing direction of the barycentric velocities over individual orbits. The net force on the orbit due to DF (black curve in the upper panel) is small and negative, always exerting a small drag on the orbit. Things become more interesting in the center panel, where we show the momentum transport forces acting along the orbit. The blue and gray curves are the first and second terms of equation 4.6, while the black curve is the total, $F_{\dot{p},\text{orb}}$. Consider the blue curve, for m_1. The momentum accretion often causes a drag on the orbital motion of m_1. The most negative value (largest drag force) occurs while m_1 is moving in the same direction as the wind (for example, the bottom three panels of figure 4.4). At some instances, the blue curve turns positive. This occurs when m_1 is traveling head-on into the wind. At this time, m_1 is moving supersonically relative to the material behind the primary shock. The sharp (positive) peaks in the blue curve occur when a secondary shock forms ahead of m_1 (as in the first snapshot of figure 4.4). In these cases, m_1 shocks and focuses material locally, accreting some of this material from downstream. This material is moving in the same direction as m_1 when it is accreted, giving m_1 a momentum thrust. Although the momentum transport forces on m_1 and m_2 are sometimes positive, these forces always sum to a negative value (black curve in the middle panel of figure 4.10). This reflects the fact that, in the case of $a_0 = 0.41 R_a$, the highest accretion rates

happen during the subsonic portions of the orbit of each particle. Material accreted from upstream exerts a drag force on each particle's orbital motion, and the overall result of momentum accretion is a net drag on the orbit.

In the bottom panel of figure 4.10, we show the net force on the orbit due to momentum accretion and DF. The net force is always negative (a drag). Comparing the black curve in the bottom panel to the black curve in the center panel, we see that $F_{\dot{p},\mathrm{orb}}$ makes up a significant fraction of $F_{\mathrm{net,orb}}$. In fact, when we find the median of each curve over an integer number of orbits beginning at $t = 30\,R_\mathrm{a}/v_\infty$, we find that $\langle F_{\mathrm{net,orb}}\rangle = -0.32 F_{\mathrm{BH}}$ and $\langle F_{\dot{p},\mathrm{orb}}\rangle = -0.25 F_{\mathrm{BH}}$. So 78% of the drag on the orbit of this binary is due to momentum accretion. Momentum accretion is a local phenomenon that depends on the details of the flow in the region of the orbiting binary. This is very different from the CM forces shown in figure 4.9. The drag on the CM is dominated by the DF force that is driven by the large scale structure of the gas. A complete description of the evolution of the binary system, then, requires us to treat the problem at both large and small scales. The time variation of the forces over an orbit motivates thinking about the evolution in an orbit-averaged sense. In the next section, we calculate orbit-averaged timescales for accretion, for slow down of the CM, and for decay of the orbit. These timescales will allow us to explore the longterm impact of the forces presented here and to also consider how the evolution of a binary depends on a_0.

4.4 Timescales

A binary interacting with an ambient gas will transform as a result of drag and accretion. If $M(t)$ is the mass of the binary over time, the characteristic timescale for accretion is

$$\tau_{\mathrm{accr}} \equiv \frac{M(t=0)}{\dot{M}(t)}. \tag{4.8}$$

If $\mathbf{V}(t)$ is the velocity of the CM of the binary, then $E_{\text{trans}} = \frac{1}{2}M\mathbf{V}^2$ is the translational kinetic energy

of the CM at time t, and the characteristic timescale for slowdown of the CM is

$$\tau_{\text{stop}} \equiv \frac{E_{\text{trans}}(t = 0)}{\dot{E}_{\text{trans}}(t)}. \tag{4.9}$$

Lastly, if $a(t)$ is the semi-major axis of the binary, then

$$\tau_{\text{insp}} \equiv \frac{a(t = 0)}{\dot{a}(t)} \tag{4.10}$$

describes the time that it takes the drag-induced torques to dissipate the orbital angular momentum

of the pair.

4.4.1   Analytical Timescales

Before turning to our numerical simulations, let us see what the BHL formalism tells us

about these timescales. The BHL stopping timescales are $\tau_{\text{stop,HL}}$ and $\tau_{\text{stop,BH}}$ (equations 2.7 and

2.11, respectively) with $M = m_1 + m_2$. We derived analytical formulas for τ_{insp} in appendix A. We

quote the results here. In the regime of mild Mach numbers, the Bondi-Hoyle (BH) formalism gives

an orbital inspiral time of

$$\tau_{\text{insp,BH}} = \frac{1}{16\pi} \left(\frac{M}{G} \right)^{1/2} \rho_\infty^{-1} a^{-3/2} \left[1 + \frac{8}{\mathcal{M}_\infty^2} \frac{a}{R_a} \right]^{1/2}. \tag{4.11}$$

For large Mach numbers, the Hoyle-Lyttleton (HL) characteristic scalings give an orbital inspiral

time of

$$\tau_{\text{insp,HL}} = \frac{1}{16\pi} \left(\frac{M}{G} \right)^{1/2} \rho_\infty^{-1} a^{-3/2}. \tag{4.12}$$

The two stopping times are related by equation 2.13 and the inspiral times are related by

$$\tau_{\text{insp,BH}} = \tau_{\text{insp,HL}} \left[1 + \frac{8}{\mathcal{M}_\infty^2} \frac{a}{R_a} \right]^{1/2}. \tag{4.13}$$

All of these expressions are inversely proportional to the ambient density, ρ_∞. If the density of the medium is increased, then the binary evolves more quickly. A less-intuitive feature of the two inspiral timescales is the leading-order dependence on $a^{-3/2}$. This dependence arises from the fact that the accretion radius of each particle is inversely proportional to the square of its speed relative to the gas. As the binary separation decreases, the orbital speed of each particle increases, so the BHL force decreases with decreasing a. We will discuss both of these features of the inspiral timescale in detail in section 4.4.2. A natural question to ask is whether the stopping time is longer than the inspiral timescale for a given binary. In the BH regime, the ratio of the timescales is

$$\frac{\tau_{\text{insp,BH}}}{\tau_{\text{stop,BH}}} = \frac{1}{2^{7/2}} \left(\frac{\mathcal{M}_\infty^2}{1+\mathcal{M}_\infty^2} \right)^{3/2} \left(\frac{R_a}{a} \right)^{3/2} \left[1 + \frac{8}{\mathcal{M}_\infty^2} \frac{a}{R_a} \right]^{1/2}. \tag{4.14}$$

For $\mathcal{M}_\infty = 2$, this says that $\tau_{\text{stop,BH}} > \tau_{\text{insp,BH}}$ where $a \gtrsim 0.18 R_a$ (this transition occurs at $a = 0.198 R_a$ if the HL timescales are used instead). Of course, BHL is a scalar description, which can take us only so far. We saw in section 4.3 that the large- and small-scale hydrodynamics as well as the changing velocity vectors of the two particles require numerical calculation. Let us turn to our numerical simulations to see how these forces effect the longterm evolution of each system.

4.4.2 Numerical Timescales

For our simulated binaries, the instantaneous timescales defined by equations 4.8, 4.9, and 4.10 will carry the imprint of the orbital motion of the binary. To understand the longterm evolution of each binary, we instead want to find orbit-averaged values. First, we construct the instantaneous timescales according to equations 4.8, 4.9, and 4.10, selecting an integer number of orbits from $t = 30 R_{\text{a}}/v_\infty$ until the end of each simulation ($t = 50 R_a/v_\infty$). Then, we simply take the median of the data to find the orbit-averaged timescales. These values are plotted with points in the upper panel of figure 4.11, where we plot each timescale as a function of initial semi-major axis, a_0. To indicate

the time-variability of each timescale over the orbits used, the 15.87th to 87.13th percentile range is shown with error bars. We plot $\langle \tau_{\text{accr}} \rangle$ in red, $\langle \tau_{\text{insp}} \rangle$ in black, and $\langle \tau_{\text{stop}} \rangle$ in purple (recall that angle brackets indicate the average over an integer number of orbits). The lower panel of the figure repeats the plot of $\langle \tau_{\text{stop}} \rangle$ but with the y axis scaled to show the plot more clearly. All timescales have been normalized to the BH stopping time, $\tau_{\text{stop,BH}} = (v_\infty^2 + c_{s,\infty}^2)^{3/2}/(4\pi G^2 M \rho_\infty)$. For $a_0 = 0.0 R_a$, the median and percentile ranges of $\langle \tau_{\text{accr}} \rangle$ and $\langle \tau_{\text{stop}} \rangle$ are computed over $30 \leq t \leq 50 R_a/v_\infty$. The difference in $\langle \tau_{\text{accr}} \rangle$ and $\langle \tau_{\text{stop}} \rangle$ at $a_0 = 0.0 R_a$ conveys the difference in efficiency of accretion and drag. These are not new results (eg. [33, 17]). Our interest here is in how these timescales change as we introduce binaries of increasing separation. The lengthening accretion timescale with larger binary separation comes as no surprise, since figure 4.8 showed a drop in $\dot{M}$ with larger a_0. We also see that $\langle \tau_{\text{stop}} \rangle$ changes by less than 10% as the binary separation increases. This reflects the fact that the slow-down of the CM is dominated by the DF force due to the downstream wake. We saw in section 4.1, that the primary shock is qualitatively similar for our simulated binaries. The wider binaries show larger time-variablity since the primary shock changes shape as the particles move in and out of each other's wakes (see figure 4.1), but the overall structure downstream from the binary is similar in each simulation. The stopping timescale is longer for binaries than in the single-particle case since the velocity vectors of the two particles do not always lie along the same line as the forces acting on the CM. The x component of each particle's velocity vector changes in magnitude and direction over an orbit. When this component is smaller, the ability of the forces to do work on the CM motion is also smaller, causing an overall lengthening of $\langle \tau_{\text{stop}} \rangle$ for the binary systems.

Figure 4.11 shows that the timescales fall into a clear hierarchy with $\langle \tau_{\text{accr}} \rangle > \langle \tau_{\text{insp}} \rangle > \langle \tau_{\text{stop}} \rangle$. The most striking aspect of this hierarchy is that $\langle \tau_{\text{insp}} \rangle > \langle \tau_{\text{stop}} \rangle$ for all of the binary systems
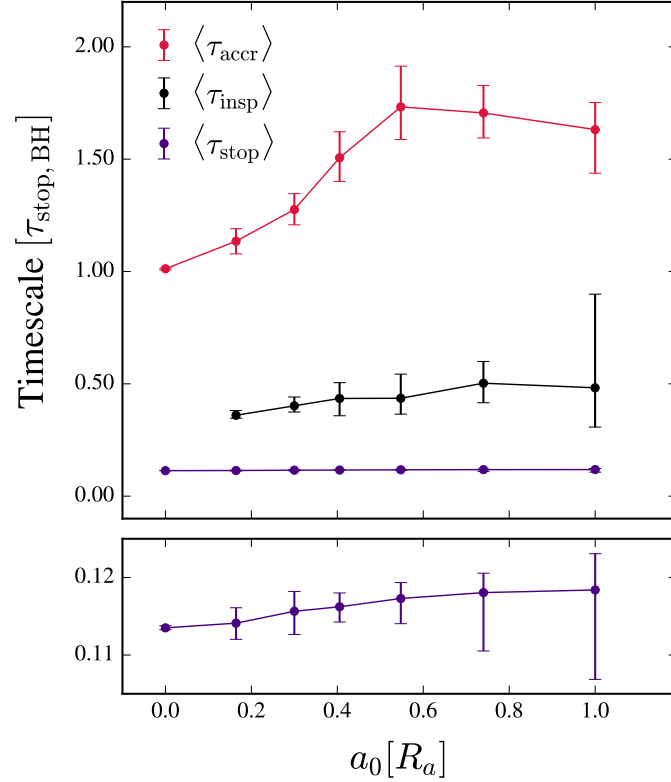
Figure 4.11: Orbit-averaged timescales versus initial semi-major axis, a_0. For each simulation, we calculate the instantaneous timescales τ_{accr}, τ_{stop}, and τ_{insp} according to equations 4.8, 4.9, and 4.10, respectively. Then, taking the median of the instantaneous timescales over an integer number of orbits from $t = 30R_a/v_\infty$ through the end of the simulation gives their respective orbit-averaged values: $\langle\tau_{\text{accr}}\rangle$, $\langle\tau_{\text{stop}}\rangle$, and $\langle\tau_{\text{insp}}\rangle$. The filled circles give these median values while the error bars show the 15.87th to 87.13th percentile range. $\langle\tau_{\text{accr}}\rangle$ is in red, $\langle\tau_{\text{insp}}\rangle$ is in black, and $\langle\tau_{\text{stop}}\rangle$ is in purple. We repeat the plot of $\langle\tau_{\text{stop}}\rangle$ in the bottom panel for clarity. Unlike the prediction of BHL, we find that for all of the simulated binaries, the CM motion slows faster than the orbit decays. The difference between $\langle\tau_{\text{accr}}\rangle$ and $\langle\tau_{\text{stop}}\rangle$ for the $a_0 = 0R_a$ simulation (single particle) indicates the difference in efficiency between accretion and drag on the CM. The shape of $\langle\tau_{\text{accr}}\rangle$ with increasing a_0, though, shows the truncation of the accretion rate as the binary separation grows. Though not clear in the present figure, the shape of $\langle\tau_{\text{insp}}\rangle$ versus a_0 is important. We explore the matter in detail in figure 4.12 and the associated text.

we simulated. In section 4.4.1, we found that a simple application of BHL predicts that $\langle \tau_{\text{stop}} \rangle$ should be longer than $\langle \tau_{\text{insp}} \rangle$ for all binaries with $a_0 \geq 0.18 R_a$. Clearly this is not the case for our simulated binaries. Instead, the stopping time is always shorter, which means that the CM motion will come to a stop before the orbit decays. The implication of this result can have profound consequences for binaries embedded in a common envelope and for binaries interacting with AGN disks. We will discuss these systems in more detail in section 5.

Another prediction of the BHL formalism is the shape of $\langle \tau_{\text{insp}} \rangle$ as a function of a_0. We plot $\tau_{\text{insp,BH}}$ versus a_0 in figure 4.12 (dashed line). The plot reveals the $a^{-3/2}$ leading order shape of $\tau_{\text{insp,BH}}$. This analytical inspiral time *increases* with decreasing a_0, which says that the binary will take an infinite time to merge. We include in figure 4.12 our calculated values of $\langle \tau_{\text{insp}} \rangle$ in black. These black points and error bars are identical to those of figure 4.11. The shape of $\langle \tau_{\text{insp}} \rangle$ is certainly not $a^{-3/2}$. Instead, the timescale *decreases* with decreasing a_0. To obtain the a_0-dependence of $\langle \tau_{\text{insp}} \rangle$, we perform a least squares fit to a power law of the form

$$f(a_0) = A(a_0/R_a)^B. \tag{4.15}$$

We fit to the median values (the black points in figure 4.12) and use one standard deviation (approximately the average of the upper and lower error bars) as the uncertainty on each point when performing the fit. We find $A = 0.51 \pm 0.01$ and $B = 0.19 \pm 0.01$, giving the function form

$$\tau_{\text{insp,fit}} = 0.51(a_0/R_a)^{0.19} \tag{4.16}$$

where $\tau_{\text{insp,fit}}$ is in units of $\tau_{\text{stop,BH}}$. The fit is shown with a pink line in figure 4.12. The fact that $\tau_{\text{insp,fit}} \propto a_0^{0.19}$ means that gas drag and accretion can shrink the binary separation and that the inspiral time becomes shorter as the orbit decays. The consequences of this are profound. The presence of gas can indeed reduce the binary separation to a value at which GW radiation can take over. The
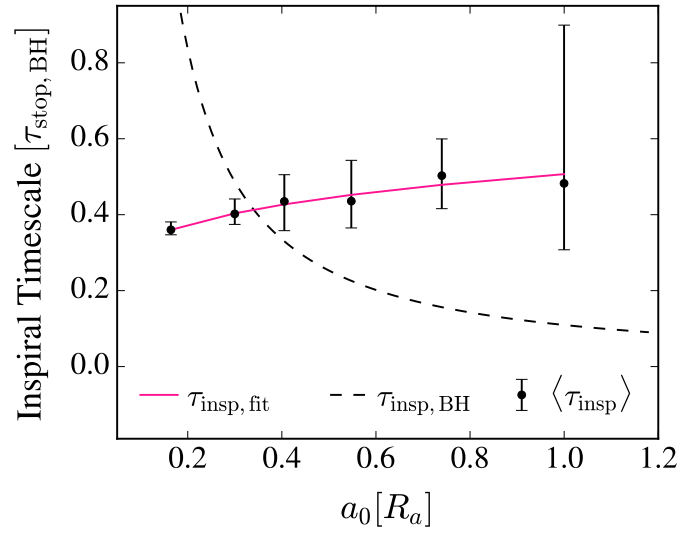
Figure 4.12: Comparison of inspiral timescale to theory. In black, we plot $\langle \tau_{\text{insp}} \rangle$, the orbit-averaged inspiral timescale for our simulated binaries, from figure 4.11. A least squares fit of $\langle \tau_{\text{insp}} \rangle$ gives $\tau_{\text{insp,fit}} = 0.51(a_0/R_a)^{0.19}$ (pink line). This increasing inspiral time with a_0 is in stark contrast to the timescale predicted by BHL theory, with leading order behavior of $\tau_{\text{insp,BH}} \propto a^{-3/2}$ (dashed line), which says the binary will never merge. Instead, our simulations show that the inspiral timescale decreases as the binary spirals in, which means that the gas can bring the binary to a separation at which the strong power-law of inspiral due to GW radiation ($\tau_{\text{insp,GW}} \propto a_0^4$) can take over.

timescale for merger of an equal mass binary on a circular orbit by GWs follows the strong power-law $\tau_{\mathrm{insp,GW}} \propto a_0^4$. In section 5, we will find the critical separation that marks the transition between gas-dominated inspiral ($\tau_{\mathrm{insp,fit}}$) and GW-dominated inspiral ($\tau_{\mathrm{insp,GW}}$) and discuss the implications of these results.

The BHL formalism clearly fails to predict the a_0-dependence of τ_{insp}. We hope that we have convinced the reader that calculation of the accretion and drag effecting the orbit is a hydrodynamical problem, requiring numerical solution. The forces doing work on the orbit depend both on the *rate* of accretion and the *direction* that the accreted material is traveling at the time of capture. The magnitude and direction of these forces change with time. They depend on the orbital phase of the binary, the crossing time of material across the orbit, and whether or not the individual particles are supersonic relative to the local gas. We have already emphasized that BHL is a scalar description: it simply cannot capture the time-dependent, vector-driven aspects of the gas-particle interactions. At the same time, single-particle BHL has been extremely useful in an order-of-magnitude sense for the last 70 years to describe the evolution of a point particle moving through a gas. It would be useful if we could diagnose some of the physical reasons for the disagreement between the predicted $a^{-3/2}$ dependence of $\tau_{\mathrm{insp,BH}}$ and the numerically obtained $a_0^{0.19}$ power law. Of course, the overall normalization of the inspiral timescale must be obtained numerically. This is not new, for even in single-particle BHL, the normalization of the accretion rate was obtained numerically by Shima [13]. Now, inspecting $\tau_{\mathrm{insp,BH}}$ in the form of equation 4.11, G is a constant and $\mathcal{M}_\infty$, R_{a}, and M do not depend on a. The background density, ρ_∞, is the only quantity that we can change. Let us explore the a-dependence of the gas density, ρ.

The presence of a gravitational potential, whether a single particle or a binary, restructures the background gas, and we certainly do not expect material near the accreting object(s) to be at

the background density. In fact, we know that material that has crossed the primary shock will find its density increased by a factor of four. In single-particle BHL, one gets by with using ρ_∞ because the dominant force is DF along the line of motion of the particle. The DF force is primarily influenced by the large-scale structure; local conditions are less important. Second, there is no length scale associated with the potential (the particle is a point source), so the density enhancement just represents an overall normalization of the accretion rate and force on the particle. This factor is just absorbed in the coefficients of drag and accretion that are generally found numerically. In the case of a binary, on the other hand, we expect the density enhancement to be more than a simple normalization factor. Instead, we expect the density structure to have some functional dependence on a. After all, the binary is a non-divergent potential whose size is set by the binary separation. The density structure at scales of the orbit must be set by this new length scale. Although the large-scale structure still sets the DF force, we have shown that the DF force does not dominate the forces acting on the orbital motion. Rather, the momentum transport force is equally important, and this force is sensitive to the density of material at orbital scales.

It would be helpful to improve $\tau_{\mathrm{insp,BH}}$ by replacing ρ_∞ with an expression describing the density as a function of distance from the CM of the binary. A complete description of this density structure requires numerical solution. Instead, let us consider the classical problem of spherical accretion onto a point mass, whose analytic solutions were found by Bondi [2]. Let R' be the radial distance from the CM of the binary (which is also the radial distance from the single particle in the $a = 0.0R_{\mathrm{a}}$ simulation). All of our simulated binaries are contained well within the Bondi radius (equation 2.2), so we only need to consider the small R' solution here. At small R', the gas is gravity-dominated and the solution assumes material moves at the sound speed. This gives the solution, for

$R' \ll R_B$ and $\gamma = 5/3$,

$$\rho(R') \approx \frac{2^{1/2}}{4} \rho_\infty \left(\frac{R_B}{R'} \right)^{3/2} = \frac{\mathcal{M}_\infty^3 \rho_\infty}{8} \left(\frac{R_a}{R'} \right)^{3/2} \tag{4.17}$$

[34], where we have invoked $R_B = \frac{1}{2}\mathcal{M}_\infty^2 R_a$ to write the second equality. The characteristic length scale of the orbit is a, and equation 4.17 says that we should expect something like $\rho(a) \propto a^{-3/2}$. So let us take $R' = a$ and write

$$\tilde{\rho} \equiv \frac{\mathcal{M}_\infty^3 \rho_\infty}{8} \left(\frac{R_a}{a} \right)^{3/2}. \tag{4.18}$$

Replacing ρ_∞ with $\tilde{\rho}$ in equation 4.11 cancels the leading $a^{-3/2}$ dependence of $\tau_{\mathrm{insp,BH}}$. Let us denote this modified BH inspiral timescale with a tilde to indicate that we have replaced ρ_∞ with $\tilde{\rho}$. The modified timescale is then

$$\tilde{\tau}_{\mathrm{insp,BH}} = \frac{\eta}{2\sqrt{2}\pi} \frac{v_\infty}{G\mathcal{M}_\infty^3 \rho_\infty R_a} \left[1 + \frac{8a}{\mathcal{M}_\infty^2 R_a} \right]^{1/2}. \tag{4.19}$$

The coefficient η is an overall normalization of the timescale, which we will find shortly. In figure 4.13, we compare equation 4.19 to our simulations. The orange line shows $\tilde{\tau}_{\mathrm{insp,BH}}$ with $\eta = 1$ while the blue curve shows $\tilde{\tau}_{\mathrm{insp,BH}}$ with $\eta = 4.96$. For comparison, we include the dashed line and black data points from figure 4.12. Recall that the dashed line is the original form of $\tau_{\mathrm{insp,BH}}$ with $\rho = \rho_\infty =$ constant. The black points and error bars are the orbit-averaged inspiral times from our simulations, $\langle \tau_{\mathrm{insp}} \rangle$. Again, we normalize all of the plots to $\tau_{\mathrm{stop,BH}}$.

The orange curve, with $\eta = 1$, is equivalent to taking the Bondi density profile without adjusting the normalization. At $a_0 = 0.16\ R_a$, this curve gives a value of $\tilde{\tau}_{\mathrm{insp,BH}} = 0.072\ \tau_{\mathrm{stop,BH}}$, a predicted inspiral time that is ≈ 5 times faster than what we find from our simulations. That is, the Bondi solution overestimates the density by a factor of ≈ 5. The orbital motion of the binary is a source of angular momentum for the gas, which provides pressure support to counteract the gravitational pull of the binary's CM. The orbital motion also heats the gas, giving rise to a lower-
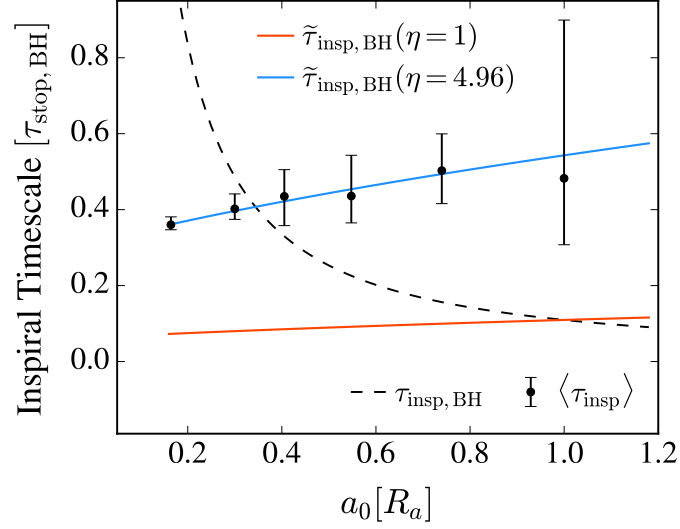
Figure 4.13: Comparison of analytical inspiral timescales. As in figure 4.12, the black points show $\langle \tau_{\mathrm{insp}} \rangle$ for our simulated binaries. The dashed line, also as in figure 4.12, shows $\tau_{\mathrm{insp,BH}}$, which assumes $\rho = \rho_\infty$. The orange and blue curves show the modified BH inspiral timescale, $\widetilde{\tau}_{\mathrm{insp,BH}}$ (equation 4.19) with $\eta = 1$ and $\eta = 4.96$, respectively. $\widetilde{\tau}_{\mathrm{insp,BH}}$ is identical to $\tau_{\mathrm{insp,BH}}$, except that it takes $\rho = \tilde{\rho}$, the Bondi density profile given by equation 4.18. The orange curve predicts an inspiral time that is ≈ 5 times faster than our simulations indicate. This is due to the fact that the Bondi density profile is never fully realized. The binary supplies the gas with angular momentum, providing pressure-support in opposition to the potential well of the binary CM. The binary's motion heats the gas, resulting in a lower-density cavity at small scales. All of these effects give our simulated binaries a lower overall density and a longer inspiral time than predicted by the orange curve. With the choice of $\eta = 4.96$, the blue curve equals $\langle \tau_{\mathrm{insp}} \rangle$ at $a_0 = 0.16 R_a$. With this normalization obtained from our simulations, we see that the blue curve provides a reasonable description of $\langle \tau_{\mathrm{insp}} \rangle$.

density cavity within the binary orbit. Combined with the constant gravitational potential enclosed by the binary orbit, an $a^{-3/2}$ profile cannot be fully realized at orbital scales and smaller. The fact that the density at scales on the order of a is much lower than predicted by theory also contributes to the important hierarchy of timescales that we discussed earlier. Clearly the inspiral of the binary takes longer than the theory predicts, meaning that a gaseous environment may capture a binary by slowing down the CM motion while still leaving a binary system intact.

With the choice of $\eta = 4.96$, the blue curve of figure 4.13 is correctly normalized to return $\widetilde{\tau}_{\mathrm{insp,BH}} = 0.36\ \tau_{\mathrm{stop,BH}}$ at $a_0 = 0.16 R_a$, the value of $\langle \tau_{\mathrm{insp}} \rangle$ at that value of a_0. We stated before

that the normalization of the timescale must come from numerical simulations; our interest here is in the shape of the analytical inspiral timescale as a function of a. Though not perfect, the blue curve provides a reasonable description of $\langle \tau_{\mathrm{insp}} \rangle$. Unlike the dashed curve (which assumes that $\rho = \rho_\infty$), the blue curve gives an inspiral time that decreases as the binary separation decreases. The timescale mildly increases with a, although somewhat more steeply than $\langle \tau_{\mathrm{insp}} \rangle$. This slight disagreement is to be expected since we do not expect the Bondi density profile to exactly describe the flow of our binary systems. First, the pressure support provided by the angular momentum of the orbital motion means that material is not gravity-dominated as it falls closer to the binary, as is assumed by the Bondi solution. Second, the Bondi problem describes a point-mass at rest relative to the gas at infinity. The CM of our simulated systems is moving at v_∞ relative to the gas at infinity. The incoming wind sweeps material from the region of the binary, constantly modifying the density structure of the local region. Despite these differences, comparison to these analytical solutions is useful. We have shown that the background density indeed has a dependence on the binary separation and this density structure clearly impacts the inspiral timescales realized by binary systems moving through gases. In fact, our simple application of the Bondi density profile has recovered an important feature of $\langle \tau_{\mathrm{insp}} \rangle$: the inspiral time is a rising power law with a. As we discussed earlier in this subsection, this positive power law gives the gas the ability to shrink the separation of a binary and this effect will happen more quickly as the orbit decays until reaching a critical separation at which the emission of GWs can take over.

5

Discussion

We have demonstrated that the interaction between a binary system and a gas requires a treatment of the hydrodynamics at both large and small scales. The ratio of the initial separation of the binary, a_0, relative to the accretion radius of its center of mass, R_a, is an essential parameter in describing the flow. This ratio informs the rate of mass accretion and it determines the nature of the drag forces acting on the orbital and translational motion of pair. The timescales for accretion, τ_{accr}, orbital inspiral, τ_{insp}, and slow down of the center of mass, τ_{stop} inherit this dependence on a_0/R_a. We have shown that, in opposition to the expectation from BHL, τ_{insp} is a monotonically increasing function of a_0. In addition, the timescales follow a definite hierarchy, with $\tau_{\mathrm{accr}} > \tau_{\mathrm{insp}} > \tau_{\mathrm{stop}}$ for all a_0/R_{a} that we simulated. In this section, we apply these results to the merger of binaries by GWs, to the evolution of binaries in the ISM and in the disks of AGN, and to the possible outcomes of common envelope (CE) in hierarchical triple systems.

5.1 Critical Separation between Gas- and GW-Dominated Inspiral

The timescale for orbital inspiral of a binary due to the radiation of GWs is strongly dependent on a_0. For a circular orbit, equal-mass binary, Peters [35] found

$$\tau_{\text{insp,GW}} = \frac{5a_0^4 c^5}{64 G^3 M^3}.$$ (5.1)

This says that a $10 M_\odot$ binary with a separation of $1 R_\odot$ will merge in one Myr (roughly the age of homo sapiens), but the same binary with a separation of 1 AU requires 10^6 Gyr to merge ($\approx 10^5$ times the age of the universe). The strong dependence on a_0 implies that only very massive binaries with very small separations can merge within a Hubble time (≈ 14 Gyr). On the other hand, our results show that the presence of gas can reduce the separation of a binary with a timescale that shortens as the binary spirals in. The mild, positive power law that we found numerically, $\tau_{\text{insp,gas}} \propto a_0^{0.19}$, allows $\tau_{\text{insp,gas}}$ to operate at much larger separation than $\tau_{\text{insp,GW}}$. At very small separations, though, $\tau_{\text{insp,GW}}$ will become smaller than $\tau_{\text{insp,gas}}$ and GW radiation will then be the dominate driver of the inspiral until the eventual merger of the binary. We can use our result to find the critical separation at which $\tau_{\text{insp,gas}} = \tau_{\text{insp,GW}}$, which defines the boundary between gas-dominated and GW-dominated inspiral. Our expression for $\tau_{\text{insp,fit}}$ (equation 4.16) is given in units of $\tau_{\text{stop,BH}}$. To simplify the algebra, let us write our fit in terms of $\tau_{\text{stop,HL}}$, instead. Let us define

$$\tau_{\text{insp,gas}} = A \left(\frac{a_0}{R_a} \right)^B \frac{v_\infty^3}{4\pi G^2 M \rho_\infty}.$$ (5.2)

In these units, $A = 0.71$ instead of 0.51 ($B = 0.19$ as before). Equating $\tau_{\text{insp,gas}}$ and $\tau_{\text{insp,GW}}$ gives the critical separation

$$a_{0,\text{crit}} = \frac{1}{2} \left[\frac{A}{5\pi} \frac{G^{1-B}}{c^5} M^{2-B} v_\infty^{2B+3} \rho_\infty^{-1} \right]^{1/(4-B)}$$ (5.3)
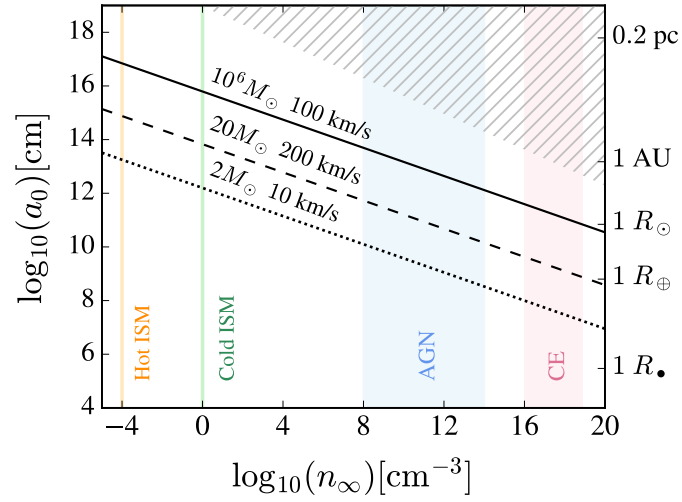
with $A = 0.71$ and $B = 0.19$.

Figure 5.1: Critical separation between gas-dominated and GW-dominated inspiral as a function of background number density, n_∞. The black curves show $a_{0,\mathrm{crit}}$ (equation 5.3) for three combinations of M and v_∞: $M = 10^6 M_\odot$ and $v_\infty = 100$ km /s (solid); $M = 20 M_\odot$ and $v_\infty = 200$ km / s (dashed); $M = 2M_\odot$ and $v_\infty = 10$ km /s (dotted). Above each line, $\tau_{\mathrm{insp,gas}} < \tau_{\mathrm{insp,GW}}$. Below each line, $\tau_{\mathrm{insp,gas}} > \tau_{\mathrm{insp,GW}}$. Vertical shaded regions correspond to the densities found in the Hot ISM (orange), the Cold ISM (green), an AGN disk (blue), and a red giant envelope (pink). In the grey hatched region, a $2M_\odot$ binary would enclose more than its own mass and, thus, would not remain bound. For higher mass binaries, this "forbidden" region moves up and to the right. See the text for an application of this plot to a few astrophysical systems.

In figure 5.1, we plot $a_{0,\text{crit}}$ versus number density, n_∞, for three sample binary systems (black lines), where we have converted mass density to number density through $\rho_\infty = m_p n_\infty$. The y axis gives a_0 in cm and the x axis gives n_∞ in cm^{-3}. Both axis are log-scaled. The accompanying y axis on the right side of the figure is identical to the y axis at left, but we have instead labeled the axis with standard astrophysical length scales ranging from $R_\bullet$, the Schwarzchild radius of a 1 $M_\odot$ black hole, to 0.2 pc (probably the limit for widely separated binaries to remain bound [36, 37]). The vertical shaded regions give the typical densities encountered in the hot ISM (orange), the cold ISM (green), a model AGN disk (blue), and the envelope of a red giant (pink; labeled "CE" for common envelope). The ISM densities use values from [19], the AGN conditions use the disk models of [10], and the CE densities are modeled after the red giant proposed by [38] to have initiated a CE phase in the hierarchical triple system PSR J0337+1715 . A given binary cannot occupy all regions of this figure. The binary will be tidally disrupted if its orbit encloses a mass on the order of its own. Assuming a uniform-density sphere of radius $a_0/2$, the mass enclosed by the binary orbit is $M_{\text{encl}} \approx \pi(a_0/2)^4 n_\infty m_p$. As an example, the grey hatched region in the figure shows where $M_{\text{encl}} > 2M_\odot$. This region is off-limits to a binary of $2M_\odot$. For higher mass binaries, the lower boundary of the hatched region moves up and to the right. Each black line plots equation 5.3 for a different combination of M and v_∞. The solid line takes $M = 10^6 M_\odot$ and $v_\infty = 100$ km /s, the dashed line uses $M = 20M_\odot$ and $v_\infty = 200$ km / s, and the dotted line corresponds to $M = 2M_\odot$ and $v_\infty = 10$ km /s. Above each line, $\tau_{\text{insp,gas}}$ is faster than $\tau_{\text{insp,GW}}$ and we say that the binary is in the gas-dominated regime. Below each line, $\tau_{\text{insp,GW}} < \tau_{\text{insp,gas}}$, and the binary is in the GW-dominated regime. Let us consider some example systems in the context of this figure.

5.1.1 Cold ISM

The cold ISM has a number density of 1 cm^{-3} and a temperature of 10^4 K. A binary traveling at 10 km/s relative to the gas has a Mach number of 1.1. At this speed, a $2M_\odot$ binary with a separation of 1 AU has $\tau_{\mathrm{insp,gas}} > \tau_{\mathrm{insp,GW}}$. For this system, our numerical fits of $\langle \tau_{\mathrm{insp}} \rangle$ and $\langle \tau_{\mathrm{stop}} \rangle$ (equations 4.16 and B.2, respectively) give a stopping timescale of 2×10^{14} yr and an orbital inspiral timescale of 5×10^{13} yr. Using $2\dot{P}_{\mathrm{orb}}/P_{\mathrm{orb}} = 3\dot{a}/a = 3/\tau_{\mathrm{insp}}$, the inspiral time gives a period derivative of $\dot{P}_{\mathrm{orb}} \approx 10^{-13}$. The very precise tracking of the rotational phase of a pulsar can make such extremely accurate timing measurements and, in principle, test this prediction.

5.1.2 AGN Disks

The central regions of galaxies hosting young AGN experience a large influx of gas that settles into a cold accretion disk. Binary systems are expected to be common in these densely populated regions due to dynamical interactions between stars and due to the trapping of stars by the AGN disk itself. Stars trapped by the disk may feed the growth of the central black hole [39]. Their high accretion rates - fueled by high densities in the disk - allow stellar evolution to proceed rapidly, enhancing the metallicity of the AGN with supernovae ejecta [40]. Our result that $\tau_{\mathrm{stop}} < \tau_{\mathrm{insp}}$ for all the binaries we simulated demonstrates that trapping by the AGN disk is not reserved for single stars. Instead, the CM motion of a binary can be slowed by the gaseous disk without causing a merger of the binary. That is, binaries formed outside of the disk can remain intact after undergoing capture.

Binary black holes (BBHs) that can merge in much less than a Hubble time serve as critical sources of GWs for ground-based detectors such as Advanced LIGO. BBHs, in particular, should be common in galactic nuclei [10]. High-mass stars will sink to the center of the galactic

potential well, where they may be captured by the AGN disk. Rapid mass growth due to accretion of disk gas should enhance the abundance of single black holes. Of course, in the dense stellar environments characteristic of galactic centers, BBHs will form dynamically from this reservoir of stellar mass BHs. In the field, stellar mass BBHs must have small binary separations to merge within a Hubble time, but our results indicate that the merger of BBHs embedded in the disk will be greatly aided by gas drag. In addition, BBH mergers in dense, gaseous environments may be accompanied by detectable electromagnetic emission [9].

Let us give two concrete examples of binaries interacting with an AGN disk. Using the disk model of Bartos et al. (their equation 1 - 4; [10]) with a central BH mass of $M_\bullet = 10^6 M_\odot$, we can find the density as a function of R_{disk}, the cylindrical distance from the BH. In general, the central black hole dominates the gravitational force within ≈ 1 pc, so we assume that binaries orbiting the BH in this region do so in Keplerian orbits with a CM speed of $v_\infty = \sqrt{GM_\bullet / R_{\text{disk}}}$.

- At $R_{\text{disk}} = 1$ pc, the disk has a number density of 6×10^9 cm^{-3}. A binary in a Keplerian orbit with $v_\infty = 66$ km /s will have $\mathcal{M}_\infty = 4$ (neglecting the effect of rotation of the disk, which will increase or decrease the relative motion between the binary and the gas depending on the direction and inclination of the binary's orbit about the black hole). A $2M_\odot$ binary with $a_0 = 1$ AU $= 1.2R_a$ falls in the gas-dominated regime. The stopping timescale for the binary is 5×10^5 yr, while the inspiral timescale is 2×10^6 yr.

- At $R_{\text{disk}} = 0.1$ pc, $n_\infty = 3 \times 10^{11}$ cm^{-3} and the Keplerian speed is $v_\infty = 207$ km / s. This speed gives a CM Mach number of 4.6, again assuming motion is perpendicular to the disk. A $20M_\odot$ binary with $a_0 = 2$ AU falls in the gas-dominated region of the plot (well above the dashed line, which corresponds to a $20M_\odot$ binary with $v_\infty = 200$ km /s). Using our fitting formula, we find for this interaction $\tau_{\text{stop}} = 4 \times 10^4$ yr, $\tau_{\text{insp}} = 2 \times 10^5$ yr, and $\tau_{\text{accr}} = 5 \times 10^5$ yr.

5.1.3 Embedded binaries in Common Envelope (CE)

Triple-star systems are common [41]. For long-term dynamical stability, these systems must be hierarchical (that is, a large mass difference between the inner and outer members of the system; [42]). In triples containing compact objects, significant mass-transfer events must have taken place as their stellar progenitors evolved (eg. PSR J0337+1715, a neutron star orbited by two white dwarfs; [43, 38]). In the progenitor system, a binary may have accreted the stellar wind from the third star in the system, or have become embedded in a common envelope when the third star evolved to become a giant. Unraveling the outcomes of these encounters requires an understanding of gas accretion and orbital evolution as studied in this paper. If one assumes a simple formalism, such as the timescales derived from BHL, it would appear that a binary embedded in a CE should merge faster than its CM spirals into the donor star's envelope. We have shown here that this is not necessarily the case. Instead, we have found that the slow-down of the binary's CM (which is the driver of the CE inspiral) occurs more quickly than the binary's own finite separation decays. The outcome of a binary embedded in a CE is not known and is the subject of ongoing debate, but our results indicate that a the binary CM can spiral into the envelope gas and that that process alone will not cause the binary to merge. Since the binary may be able to complete part of the CE inspiral intact, there are many possible outcomes for the interaction. The binary may survive the CE if the envelope can be ejected early in the encounter, the binary may be tidally disrupted before envelope ejection, or, in the case of unsuccessful envelope ejections, one or both of the binary components could merge with the core of the donor star. The revised formalism presented in this paper should be used when examining the various outcomes expected from these complex interactions.

6

Conclusions

This paper has studied the evolution of binaries moving through gaseous media as a function of the binary system's initial semi-major axis, a_0, relative to its gravitational focussing radius, R_a. We extended the analytical and numerical formalisms of single-particle Bondi-Hoyle-Lyttleton accretion to the case of a binary system whose center of mass moves perpendicularly to the orbital angular momentum vector of the pair. We performed 3D hydrodynamical simulations to study the effects of accretion and drag on the translational and orbital motion of the system. Let us summarize the main conclusions of this work.

1. The introduction of a finite binary separation softens the gravitational potential of the pair, truncating the densities that can be achieved within the binary orbit. The orbital angular momentum provides pressure support to the gas, further reducing the amount of material that can fall into the potential well of the binary CM.

2. The orbit-averaged accretion rates of binary systems are reduced relative to the single-particle value of $\approx \dot{M}_{\mathrm{BH}} = 4\pi G^2 M^2 \rho_\infty (v_\infty^2 + c_{s,\infty}^2)^{-3/2}$ (see figure 4.8). Increasing the binary separation decreases these median accretion rates further. The decline is not monotonic as a_0

increases from $0.55R_a$ to $1.0R_a$, because $a_0 = 0.74R_a$ and $a_0 = 1.0R_a$ represent the transition from $a_0 < R_{BH}$ to $a_0 > R_{BH}$. In this transition, significant orbital variation of the instantaneous accretion rates is present, and this variation is exhibited in the non-monotonic decrease in the median accretion rates.

3. As in the single-particle case, gaseous dynamical friction due to the large scale structure of the gas is the dominant force slowing down the translational motion of the CM. The orbital decay of the binary, on the other hand, is strongly influenced by momentum accretion, with momentum accretion and dynamical friction playing roughly an equal role in decreasing the separation of the binary.

4. Unlike the behavior expected from the BHL formalism, the net force on the orbital motion of the binary *increases* with *decreasing a*.

5. The timescales for accretion, τ_{accr}, orbital inspiral of the binary, τ_{insp}, and slow down of the CM, τ_{stop}, all depend on a_0. For all values of a_0 that we simulated, though, the timescales exhibit a clear hierarchy with $\tau_{stop} < \tau_{insp} < \tau_{accr}$. Therefore, a gaseous medium can slow down the CM motion of a binary to a stop while leaving a finite binary separation intact.

6. Equation 4.16 gives $\tau_{insp,fit}$, our fit for the orbit-averaged inspiral time of the binaries $\langle \tau_{insp} \rangle$ as a function of a_0. We find $\tau_{insp,fit} \propto a_0^{0.19}$. Since τ_{insp} decreases with decreasing binary separation, gas drag can successfully reduce the binary separation.

7. Gas drag can shrink the binary separation until the timescale for orbital inspiral due to GW radiation, $\tau_{insp,GW}$, becomes shorter than the inspiral timescale due to the gas. The critical a_0 at which this transition occurs is $a_{0,crit}$, given in equation 5.3.

There are many aspects of this problem left to explore. In this work, we have considered binary systems moving such that the incoming wind hits the orbital plane edge-on. Sánchez-Salcedo and Chametla [5] solved, in detail, the "face-on" case (orbital angular momentum vector parallel to the CM velocity vector). Of course, a binary's CM may move at any angle relative to the orbital plane and we imagine future simulations in which we study the effects of inclination between the two vectors. To extend the formalism of BHL, we studied the idealized case of a uniform-density background gas. Binary systems are often subject to nonuniform gases with gradients in density, pressure, and Mach number. Previous work has shown that breaking the archetypal symmetry of canonical BHL has significant impacts on the flow. For example, MacLeod and collaborators [31, 32] found that in single-particle BHL, the presence of realistic density gradients (like those found in the interiors of red giants during CE) reduces the rates of accretion since the gradient gives the gas a net angular momentum about the point mass. The binary case is interesting as this net angular momentum may be aligned, anti-aligned, or at some arbitrary angle relative to the angular momentum of the binary's orbit.

63

Acknowledgements

Appendix A

Derivation of Analytical Timescales

A principle objective of this paper is to learn how the predictions of BHL must be modified to describe a binary system. To that end, let us use the BHL formalism to find simple analytic versions of the timescales defined by equations 4.8, 4.9, and 4.10.

A.1 Timescales for Stopping and Accretion

For a binary of mass M moving at v_∞ relative to the gas, if we assume F_{BH} (equation 2.9) acts on the CM of the pair, then the CM slows at a rate of $\dot{E}_{\mathrm{BH}}$ (equation 2.10). The characteristic stopping time of the CM is just $\tau_{\mathrm{stop,BH}}$, given in equation 2.11 where now M is the total mass of the binary. In the Hoyle-Lyttleton formalism, the stopping time of the binary CM is $\tau_{\mathrm{stop,HL}}$, given by equation 2.7.

Although we must, in general, differentiate between τ_{accr} and τ_{stop} (because accretion and drag have some efficiencies associated with them), it is not necessary to define an analytical

accretion timescale in the BHL formalism since

$$\tau_{\text{accr,HL}} = \frac{M}{\dot{M}_{\text{HL}}} = \frac{\frac{1}{2}Mv_\infty^2}{\frac{1}{2}\dot{M}_{\text{HL}}v_\infty^2} = \frac{\frac{1}{2}Mv_\infty^2}{\dot{E}_{\text{HL}}} = \tau_{\text{stop,HL}}. \tag{A.1}$$

A.2 Orbital Inspiral Timescales

To associate a timescale with the decay of the orbit, we imagine the CM at rest and calculate the Bondi-Hoyle energy dissipation rate for m_1 and m_2 as they orbit the CM. For an equal-mass binary in a circular orbit,

$$m_1 = m_2 = \frac{1}{2}M \tag{A.2}$$

and the orbital speed is

$$v_{\text{orb}}^2 = \frac{GM}{a}. \tag{A.3}$$

If V_1 and V_2 are the barycentric speeds of m_1 and m_2, respectively, then

$$V_1 = V_2 = \frac{1}{2}v_{\text{orb}}. \tag{A.4}$$

The accretion radius of m_1 is

$$R_{\text{BH},1} = \frac{2Gm_1}{V_1^2 + c_{s,\infty}^2} = \frac{2G(M/2)}{(v_{\text{orb}}/2)^2 + c_{s,\infty}^2} = \frac{4GM}{v_{\text{orb}}^2 + 4c_{s,\infty}^2} \tag{A.5}$$

with an accretion rate

$$\dot{M}_{\text{BH},1} = \pi R_{\text{BH},1}^2 \rho_\infty (V_1^2 + c_{s,\infty}^2)^{1/2} = \pi \left(\frac{4GM}{v_{\text{orb}}^2 + 4c_{s,\infty}^2}\right)^2 \rho_\infty (v_{\text{orb}}^2/4 + c_{s,\infty}^2)^{1/2}$$

$$= \frac{16\pi G^2 M^2}{(v_{\text{orb}}^2 + 4c_{s,\infty}^2)^2} \rho_\infty \frac{1}{2}(v_{\text{orb}}^2 + 4c_{s,\infty}^2)^{1/2} = 8\pi G^2 M^2 \rho_\infty (v_{\text{orb}}^2 + 4c_{s,\infty}^2)^{-3/2}. \tag{A.6}$$

The energy dissipation rate for m_1 is

$$\dot{E}_{\text{BH},1} = \frac{1}{2}\dot{M}_{\text{BH},1}(V_1^2 + c_{s,\infty}^2) = \frac{1}{8}\dot{M}_{\text{BH},1}(v_{\text{orb}}^2 + 4c_{s,\infty}^2) = \pi G^2 M^2 \rho_\infty (v_{\text{orb}}^2 + 4c_{s,\infty}^2)^{-1/2}. \tag{A.7}$$

The total for m_1 and m_2 is just twice $\dot{E}_{\text{BH},1}$, or

$$\dot{E}_{\text{BH,orb}} = 2\pi G^2 M^2 \rho_\infty (v_{\text{orb}}^2 + 4c_{s,\infty}^2)^{-1/2}. \tag{A.8}$$

The total orbital energy of the binary is

$$E_{\text{orb}} = -\frac{Gm_1 m_2}{2a} = -\frac{GM^2}{8a}. \tag{A.9}$$

so the timescale for orbital decay is

$$\tau_{\text{insp,BH}} \equiv \frac{|E_{\text{orb}}|}{\dot{E}_{\text{BH,orb}}} = \frac{GM^2/8a}{2\pi G^2 M^2 \rho_\infty (v_{\text{orb}}^2 + 4c_{s,\infty}^2)^{-1/2}} = \frac{\rho_\infty^{-1} a^{-1}}{16\pi G} (v_{\text{orb}}^2 + 4c_{s,\infty}^2)^{1/2}. \tag{A.10}$$

If we factor v_{orb}^2 out of the parenthesis and substitute $v_{\text{orb}} = (GM/a)^{1/2}$ then

$$\tau_{\text{insp,BH}} = \frac{\rho_\infty^{-1} a^{-1}}{16\pi G} \left(\frac{GM}{a}\right)^{1/2} \left[1 + 4a\frac{c_{s,\infty}^2}{GM}\right]^{1/2} = \frac{\rho_\infty^{-1} a^{-3/2}}{16\pi} \left(\frac{M}{G}\right)^{1/2} \left[1 + 4a\frac{c_{s,\infty}^2}{GM}\right]^{1/2}. \tag{A.11}$$

Now,

$$\frac{c_{s,\infty}^2}{GM} = \frac{2c_{s,\infty}^2}{v_\infty^2} \frac{v_\infty^2}{2GM} = \frac{2}{\mathcal{M}_\infty^2 R_a} \tag{A.12}$$

so we can write

$$\tau_{\text{insp,BH}} = \frac{1}{16\pi} \left(\frac{M}{G}\right)^{1/2} \rho_\infty^{-1} a^{-3/2} \left[1 + \frac{8a}{\mathcal{M}_\infty^2 R_a}\right]^{1/2}. \tag{A.13}$$

In the Hoyle-Lyttleton formalism, the sound speed is omitted from the characteristic velocity in equations A.5, A.6, and A.7, resulting in a total orbital energy dissipation rate of

$$\dot{E}_{\text{HL,orb}} = 2\pi G^2 M^2 \rho_\infty v_{\text{orb}}^{-1} \tag{A.14}$$

and a decay timescale of

$$\tau_{\text{insp,HL}} = \frac{1}{16\pi} \left(\frac{M}{G}\right)^{1/2} \rho_\infty^{-1} a^{-3/2}. \tag{A.15}$$

which is just the leading coefficient of $\tau_{\text{insp,BH}}$. That is,

$$\tau_{\text{insp,BH}} = \tau_{\text{insp,HL}} \left[1 + \frac{8a}{\mathcal{M}_\infty^2 R_a}\right]^{1/2}. \tag{A.16}$$

Appendix B

Fitting Formulae to Simulation Results

In this section, we provide fitting formulae for the timescales, $\langle\tau_{\text{stop}}\rangle$, $\langle\tau_{\text{insp}}\rangle$, and $\langle\tau_{\text{accr}}\rangle$, and for the total accretion rate, $\langle\dot{M}\rangle$, as a function of a_0. As a reminder, the angled brackets indicate a time average of the quantity over an integer number of orbits between $t = 30R_{\text{a}}/v_\infty$ and $t = 50R_{\text{a}}/v_\infty$. The median values of each quantity for each simulation are given in table B.1. Attached to each median, the sub- and superscripts give the 15.87th to 87.13th percentile spread about the median. Recall that the median values and 15.87th to 87.13th percentile ranges were shown with point and error bars, respectively, for $\langle\dot{M}\rangle$ in figure 4.8 and for the timescales in figure 4.11. Just as in the figures, we present the values in the table in BH units. The timescales are in units of the BH stopping time, $\tau_{\text{stop,BH}} = (v_\infty^2 + c_{s,\infty}^2)^{3/2}/(4\pi G^2 M\rho_\infty)$, while $\langle\dot{M}\rangle$ is in units of $\dot{M}_{\text{BH}}$.

Using the data of table B.1, let us now find fitting formulae for $\langle\tau_{\text{insp}}\rangle$, $\langle\tau_{\text{stop}}\rangle$, $\langle\tau_{\text{accr}}\rangle$, and $\langle\dot{M}\rangle$ as a function of a_0. The fit for $\langle\tau_{\text{insp}}\rangle$ was already given in section 4.4.2. Motivated by the fact that $\langle\tau_{\text{insp}}\rangle$ appears as a line in log-log space, we found the power-law fit given by equation 4.16, which is plotted with a pink curve in figure 4.12. The remaining quantities, $\langle\tau_{\text{stop}}\rangle$, $\langle\tau_{\text{accr}}\rangle$, and $\langle\dot{M}\rangle$ appear non-linear to a varying degree in log-log space. At very large a_0, the accretion rate
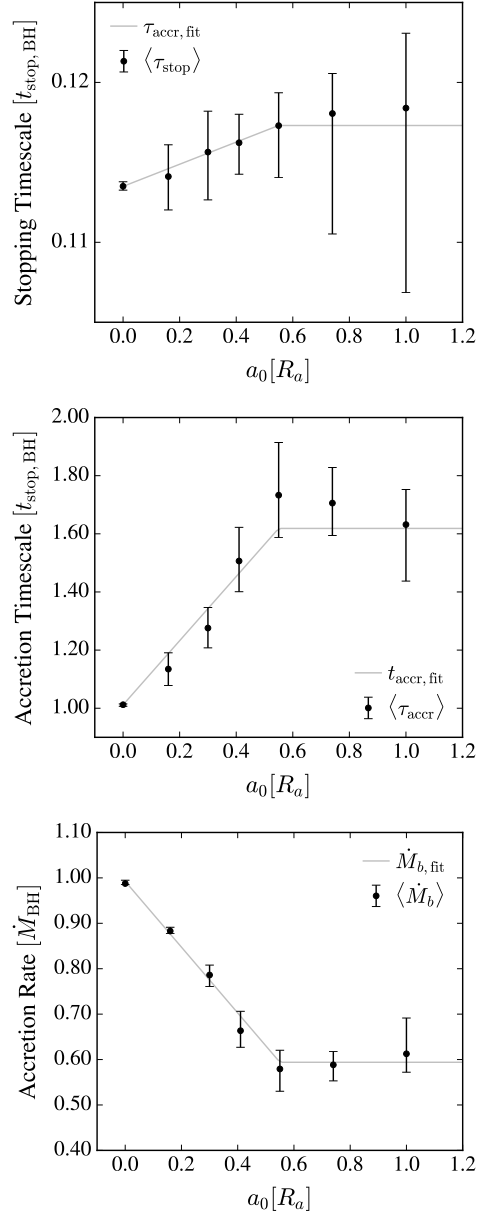
Figure B.1: Piecewise fits of $\langle\tau_{\mathrm{stop}}\rangle$, $\langle\tau_{\mathrm{accr}}\rangle$, and $\langle\dot{M}\rangle$ (left, middle, and right panels respectively). In each panel, the black points and error bars correspond to the data of table B.1 and the grey line shows the fit, which are given by equations B.2, B.3, and B.4, respectively.

a_0 [R_a]	$\langle\tau_{\text{insp}}\rangle$ [$\tau_{\text{stop,BH}}$]	$\langle\tau_{\text{stop}}\rangle$ [$\tau_{\text{stop,BH}}$]	$\langle\tau_{\text{accr}}\rangle$ [$\tau_{\text{stop,BH}}$]	$\langle\dot{M}\rangle$ [$\dot{M}_{\text{BH}}$]
0.0	—	$0.1135^{+0.0003}_{-0.0002}$	$1.0121^{+0.0029}_{-0.0054}$	$0.9875^{+0.0073}_{-0.0023}$
0.16	$0.3602^{+0.0208}_{-0.0132}$	$0.1141^{+0.0020}_{-0.0021}$	$1.1347^{+0.0560}_{-0.0563}$	$0.8830^{+0.0083}_{-0.0057}$
0.3	$0.4021^{+0.0393}_{-0.0276}$	$0.1156^{+0.0026}_{-0.0030}$	$1.2758^{+0.0709}_{-0.0681}$	$0.7862^{+0.0218}_{-0.0255}$
0.41	$0.4349^{+0.0704}_{-0.0770}$	$0.1162^{+0.0018}_{-0.0020}$	$1.5065^{+0.1158}_{-0.1056}$	$0.6635^{+0.0428}_{-0.0365}$
0.55	$0.4357^{+0.1074}_{-0.0706}$	$0.1173^{+0.0021}_{-0.0033}$	$1.7329^{+0.1812}_{-0.1452}$	$0.5793^{+0.0412}_{-0.0491}$
0.74	$0.5028^{+0.0968}_{-0.0869}$	$0.1181^{+0.0025}_{-0.0075}$	$1.7057^{+0.1224}_{-0.1114}$	$0.5883^{+0.0292}_{-0.0353}$
1.0	$0.4824^{+0.4168}_{-0.1748}$	$0.1184^{+0.0047}_{-0.0115}$	$1.6318^{+0.1207}_{-0.1944}$	$0.6127^{+0.0788}_{-0.0405}$

Table B.1: Orbit-averaged simulation data. Here we give median values of the orbit-averaged timescales and accretion rates for our simulated binaries. The subscripts and superscripts give the 15.87th to 87.13th percentile spread, respectively, about the median. The timescales are given in units of $\tau_{\text{stop,BH}}$. The accretion rates are in units of $\dot{M}_{\text{BH}}$.

and the drag on the CM should approach a constant value since wakes of the two particles become independent as $a_0 \to \infty$. To capture the slope of each quantity at small a_0 while for a constant value at large a_0, we will model $\langle\tau_{\text{stop}}\rangle$, $\langle\tau_{\text{accr}}\rangle$, and $\langle\dot{M}\rangle$ to a simple piecewise function of two lines:

$$f(a_0) = \begin{cases} A(a_0/R_a)+B & a_0 \leq 0.55R_a \\ A(0.55)+B & a_0 > 0.55R_a \end{cases} \tag{B.1}$$

where f is normalized to the appropriate BH value. We perform least-squares fits to the model, $f(a_0)$. For the uncertainty on each point, we use one standard-deviation of the data over the same time interval used to calculated the percentile values shown in table B.1. For $\langle\tau_{\text{stop}}\rangle$, we find $A = 0.007$ and $B = 0.114$, giving

$$\tau_{\text{stop,fit}}[\tau_{\text{stop,BH}}] = \begin{cases} 0.007(a_0/R_a)+0.114 & a_0 \leq 0.55R_a \\ 0.117 & a_0 > 0.55R_a \end{cases} \tag{B.2}$$

in units of $\tau_{\text{stop,BH}}$. For $\langle \tau_{\text{accr}} \rangle$, we obtain $A = 1.103$ and $B = 1.012$, resulting in the fitting formula

$$\tau_{\text{accr,fit}}\left[\tau_{\text{stop,BH}}\right] = \begin{cases} 1.103(a_0/R_{\text{a}}) + 1.012 & a_0 \leq 0.55R_{\text{a}} \\ \\ 1.619 & a_0 > 0.55R_{\text{a}} \end{cases} \tag{B.3}$$

in units of $\tau_{\text{stop,BH}}$. For the accretion rate, $\langle \dot{M} \rangle$, in units of $\dot{M}_{\text{BH}}$, we find

$$\dot{M}_{\text{b,fit}}\left[\dot{M}_{\text{BH}}\right] = \begin{cases} -0.724(a_0/R_{\text{a}}) + 0.882 & a_0 \leq 0.55R_{\text{a}} \\ \\ 0.594 & a_0 > 0.55R_{\text{a}}. \end{cases} \tag{B.4}$$

In the left, center, and right panels of figure B.1, we plot $\langle \tau_{\text{stop}} \rangle$, $\langle \tau_{\text{accr}} \rangle$, and $\langle \dot{M} \rangle$, respectively, with points and error bars. The associated fit of each quantity is shown with a grey line in each panel.

Appendix C

Attachment: Journal Paper

This appendix contains a preprint of the manuscript entitled "The Evolution of Binaries in a Gaseous Medium: Three-Dimensional Simulations of Binary Bondi-Hoyle-Lyttleton Accretion" based on the work described in this thesis. The manuscript has been reviewed by the Astrophysical Journal and is currently under minor revision in response to suggestions by the referee.

The Evolution of Binaries in a Gaseous Medium: Three-Dimensional Simulations of Binary Bondi-Hoyle-Lyttleton Accretion

Andrea Antoni,[1,2] Morgan MacLeod,[3,*] and Enrico Ramirez-Ruiz[1,4]

[1]Department of Astronomy & Astrophysics, University of California, Santa Cruz, CA 95064, USA
[2]Department of Astronomy, University of California, Berkeley, CA 94720, USA
[3]Harvard-Smithsonian Center for Astrophysics, 60 Garden Street, Cambridge, MA, 02138, USA
[4]Niels Bohr Institute, University of Copenhagen, Blegdamsvej 17, DK-2100 Copenhagen, Denmark

ABSTRACT

Binary stars are common. While only those with small separations may exchange gas with one another, even the widest binaries interact with their gaseous surroundings. Drag forces and accretion rates dictate how these systems are transformed by these interactions. We perform three-dimensional hydrodynamic simulations of Bondi-Hoyle-Lyttleton flows, in which a binary moves supersonically relative to a homogeneous medium, using the adaptive mesh refinement code FLASH. We simulate a range of values of the initial semi-major axis of the orbit relative to the gravitational focusing impact parameter of the pair. When the binary separation is less than the gravitational focusing impact parameter, the pair orbits within a shared bow shock. When the pair is wider, each object has an individual bow-shock structure. The long-term evolution of the binary is determined by the timescales for accretion, slowing of the center of mass, and orbital inspiral. We find a clear hierarchy of these timescales; a binary's center-of-mass motion is slowed over a shorter timescale than the pair inspirals or accretes. In contrast to previous analytic predictions, which assume an unperturbed background medium, we find that the timescale for orbital inspiral is proportional to the semi-major axis to the 0.19 ± 0.01 power. This positive scaling indicates that gaseous drag forces can drive binaries either to coalescence or to the critical separation at which gravitational radiation dominates their further evolution. We discuss the implications of our results for binaries embedded in the interstellar medium, active galactic nuclei disks, and common envelope phases.

1. INTRODUCTION

Many objects in the universe are found in binary systems. The components of these binaries range from substellar mass objects to supermassive black holes (SMBHs) in the centers of galaxies (Cowley 1992; Duchêne & Kraus 2013; Cherepashchuk 2014; Postnov & Yungelson 2014). In fact, roughly one third of all main-sequence (MS) stars are members of binary systems, while $\sim 10\%$ of solar-type MS stars and an overwhelming 73% of O-type MS stars have 2 or more stellar companions (Moe & Di Stefano 2017).

Multiple-star systems are found throughout the galaxy, traveling through gaseous environments with widely varying densities, temperatures, and compositions. The range of gaseous environments include the interstellar medium (Chanamé & Gould 2004), accretion flows in active galactic nuclei (AGN; Artymowicz et al. 1993), the dense envelopes of evolved companion stars (Sabach & Soker 2015; Di Stefano 2018), and the intercluster medium in young star clusters (Naiman et al. 2011, 2018; Abbate et al. 2018; Roupas & Kazanas 2019; Kaaz et al. 2019).

A gravitating object moving through gas captures mass and momentum from its surroundings (Hoyle & Lyttleton 1939; Bondi & Hoyle 1944). The drag force it feels due to its gravitationally-induced wake robs it of linear momentum (Chandrasekhar 1943; Ostriker 1999). For binary or multiple objects, drag forces could lead to a metamorphosis of the size and shape of their shared orbit.

The effects of accretion and drag can have profound consequences. For example, a metal poor star moving through the interstellar medium (ISM) could accrete, over its history, enough material to significantly enhance its birth metallicity (Shen et al. 2017). More dramatically, the orbit of a stellar-mass binary black hole (BBH) embedded in an AGN disk may be tightened by gaseous interaction to the point that the binary merges under the influence of gravitational wave (GW) radiation (Stone et al. 2017). Whether such binaries form within AGN disks or are dynamically captured (Bartos et al. 2017), they may be the only case of BBH mergers that are accompanied by an electromagnetic signature (due to the surrounding gas; Stone et al. 2017).

Corresponding author: Andrea Antoni
aantoni@berkeley.edu

* NASA Einstein Fellow

Our goal in this paper is to examine the nature of accretion and drag experienced by binaries moving through gaseous environments and to learn the extent to which we can derive physical intuition from the classical Bondi-Hoyle-Lyttleton (BHL) formalism (Hoyle & Lyttleton 1939; Bondi & Hoyle 1944; Bondi 1952). To that end we perform 3D hydrodynamical studies of binary systems moving supersonically through a gaseous medium.

In the next section, we introduce the BHL formalism for a single accretor, discuss how this formalism can be extended to binary systems, and consider the scales for astrophysically-typical encounters. In Section 3, we describe our numerical method and present the results of our hydrodynamic simulations in Sections 4 and 5. In Section 6, we discuss the implications of our results for astrophysical systems. Finally, in Section 7, we conclude.

2. SCALES AND TYPICAL ENCOUNTERS IN BINARY-BHL FLOWS

In this section we define the characteristic scales of BHL and their extension to binary systems. Finally, we briefly discuss typical astrophysical environments for binary-BHL flows.

2.1. *Characteristic Scales: Single-Object BHL*

A massive object moving through an initially-uniform background gas accelerates matter in its direction as it moves. If the motion of the mass is supersonic relative to the background, a bow shock forms and shocked gas piles up in a stagnation region downstream of the moving object. If it is absorbing, the object accretes gravitationally-bound material from the wake while the rest is eventually advected away. Although the material in this wake is, therefore, transient, the overall structure of the wake persists and it exerts a gravitational drag force on the point mass until there ceases to be relative motion between the object and the gas (Chandrasekhar 1943).

The BHL formalism provides analytical estimates for these interactions. Let M be the mass of the object, v_∞ be the speed of the object relative to the gas, and $c_{s,\infty}$ be the sound speed of the gas. The Mach number of the flow is $\mathcal{M}_\infty = v_\infty/c_{s,\infty}$. The object's influence on the gas is characterized by its accretion radius. If the object moves highly-supersonically, then we can use the Hoyle-Lyttleton accretion radius,

$$R_\text{a} = \frac{2GM}{v_\infty^2}, \tag{1}$$

where G is the gravitational constant (Hoyle & Lyttleton 1939). For very subsonic motion, the accretion radius is given by the Bondi radius,

$$R_B = \frac{GM}{c_{s,\infty}^2} = \frac{1}{2}\mathcal{M}_\infty^2 R_\text{a} \tag{2}$$

(Bondi 1952).

2.1.1. *Hoyle-Lyttleton (HL) Scalings*

In general, BHL predicts an accretion rate that is given by the flux of matter through a circular cross-section far upstream from the object, where the radius of the cross-section is the accretion radius of the object. In the highly-supersonic regime, this gives

$$\dot{M}_\text{HL} = \pi R_\text{a}^2 \rho_\infty v_\infty = 4\pi G^2 M^2 \rho_\infty v_\infty^{-3} \tag{3}$$

(Hoyle & Lyttleton 1939). The drag force on the object due to the wake is

$$F_\text{HL} = \dot{M}_\text{HL} v_\infty = 4\pi G^2 M^2 \rho_\infty v_\infty^{-2}, \tag{4}$$

and the rate at which energy is dissipated is

$$\dot{E}_\text{HL} = \frac{1}{2}\dot{M}_\text{HL} v_\infty^2 = 2\pi G^2 M^2 \rho_\infty v_\infty^{-1}. \tag{5}$$

Finally, the approximate timescale for the object to stop is

$$\tau_\text{stop,HL} \equiv \frac{\frac{1}{2}Mv_\infty^2}{\dot{E}_\text{HL}} = \frac{v_\infty^3}{4\pi G^2 M \rho_\infty}. \tag{6}$$

In the HL formalism, the accretion timescale is identical to the stopping timescale because

$$\tau_\text{accr,HL} = \frac{M}{\dot{M}_\text{HL}} = \frac{\frac{1}{2}Mv_\infty^2}{\frac{1}{2}\dot{M}_\text{HL}v_\infty^2} = \frac{\frac{1}{2}Mv_\infty^2}{\dot{E}_\text{HL}} = \tau_\text{stop,HL}. \tag{7}$$

2.1.2. *Bondi-Hoyle (BH) Scalings*

For mild Mach numbers, the work of Bondi & Hoyle (1944) and Bondi (1952) led to an interpolation formula for the accretion rate

$$\dot{M}_\text{BH} = \frac{4\pi G^2 M^2 \rho_\infty}{\left(v_\infty^2 + c_{s,\infty}^2\right)^{3/2}} = \dot{M}_\text{HL}\left(\frac{\mathcal{M}_\infty^2}{1+\mathcal{M}_\infty^2}\right)^{3/2} \tag{8}$$

where the factor of four was found by (Shima et al. 1985). It is helpful to define quantities analogous to those of the HL formalism. If we factor $\dot{M}_\text{BH}$ similarly to $\dot{M}_\text{HL}$ in equation (3), then

$$\dot{M}_\text{BH} = \pi R_\text{BH}^2 \rho_\infty (v_\infty^2 + c_{s,\infty}^2)^{1/2} \tag{9}$$

where the characteristic velocity is $(v_\infty^2 + c_{s,\infty}^2)^{1/2}$ and the BH accretion radius is

$$R_\text{BH} = \frac{2GM}{v_\infty^2 + c_{s,\infty}^2} = R_\text{a}\left(\frac{\mathcal{M}_\infty^2}{1+\mathcal{M}_\infty^2}\right). \tag{10}$$

In keeping with equation (4), we define the BH drag force as an accretion rate times a characteristic velocity, or

$$F_\text{BH} = \dot{M}_\text{BH}(v_\infty^2 + c_{s,\infty}^2)^{1/2} = F_\text{HL}\left(\frac{\mathcal{M}_\infty^2}{1+\mathcal{M}_\infty^2}\right). \tag{11}$$

For $\mathcal{M}_\infty \ll 1$, $F_{\mathrm{BH}} \approx \mathcal{M}_\infty^2 F_{\mathrm{HL}}$, whereas the piecewise analytical dynamical friction formula for a subsonic, non-accreting perturber goes as $\mathcal{M}_\infty^3 F_{\mathrm{HL}}$ (Ostriker 1999). For a highly supersonic object ($\mathcal{M}_\infty \gg 1$), $F_{\mathrm{BH}} \to F_{\mathrm{HL}}$.

Similarly, we can define the characteristic energy dissipation rate to be

$$\dot{E}_{\mathrm{BH}} = \tfrac{1}{2} \dot{M}_{\mathrm{BH}} (v_\infty^2 + c_{s,\infty}^2) = \dot{E}_{\mathrm{HL}} \left(\frac{\mathcal{M}_\infty^2}{1 + \mathcal{M}_\infty^2} \right)^{1/2}. \quad (12)$$

The translational kinetic energy of the object is $\tfrac{1}{2} M v_\infty^2$, which gives a BH stopping time of

$$\tau_{\mathrm{stop,BH}} \equiv \frac{\tfrac{1}{2} M v_\infty^2}{\dot{E}_{\mathrm{BH}}} = \tau_{\mathrm{stop,HL}} \left(\frac{1 + \mathcal{M}_\infty^2}{\mathcal{M}_\infty^2} \right)^{1/2}. \quad (13)$$

The BH accretion timescale is

$$\tau_{\mathrm{accr,BH}} = \frac{M}{\dot{M}_{\mathrm{BH}}} = \tau_{\mathrm{stop,BH}} \left(\frac{1 + \mathcal{M}_\infty^2}{\mathcal{M}_\infty^2} \right). \quad (14)$$

While the above equations are only approximately correct, coefficients for drag and accretion for the above canonical case have been obtained numerically by Shima et al. (1985); Ruffert & Arnett (1994); Ruffert (1994, 1995); Blondin & Raymer (2012). See Edgar (2005) for a review of the BHL accretion formalism, including derivations of the above equations, and Ostriker (1999) for the first analytical treatment of the gaseous dynamical friction (DF) drag approximated by the expressions for F_{HL} and F_{BH}.

2.2. *Characteristic Scales: Binary BHL*

Now consider what happens if we replace the single object of mass M with two objects, m_1 and m_2, whose total mass is M, and whose center of mass (CM) moves with velocity $\mathbf{v}_\infty$ relative to the gas. Free parameters now include the binary mass ratio, the initial eccentricity of the orbit, the inclination of the orbital plane relative to $\mathbf{v}_\infty$, and the semi-major axis of the orbit, a. We will examine the simplifying case of an equal-mass binary in an initially-circular orbit with inclination of $\pi/2$ (that is, the incoming gas intercepts the binary "edge-on" to the orbit).

Now there are two key length scales in the problem: the gravitational focusing scale, R_{BH}, and the binary semi-major axis, a. Here, R_{BH}, defined by equation (10), is the BH accretion radius of the CM. We can re-express this ratio of length scales in terms of other parameters of the binary:

$$\frac{a}{R_{\mathrm{BH}}} = \frac{GM/v_{\mathrm{orb}}^2}{2GM/(v_\infty^2 + c_{s,\infty}^2)} = \frac{v_\infty^2 + c_{s,\infty}^2}{2 v_{\mathrm{orb}}^2} = \frac{v_\infty^2 (1 + \mathcal{M}_\infty^{-2})}{2 v_{\mathrm{orb}}^2}, \quad (15)$$

where we have used the orbital speed, $v_{\mathrm{orb}} = \sqrt{GM/a}$, for a binary in a circular orbit. Therefore, in the limit of highly-supersonic motion (large $\mathcal{M}_\infty$), $a/R_{\mathrm{BH}} \approx v_\infty^2 / 2 v_{\mathrm{orb}}^2$.

We can imagine two limiting cases for the ratio of a/R_{BH}. When $a \ll R_{\mathrm{BH}}$, the binary appears essentially single as gas is focused toward the system's CM from the background medium. In this case, we might imagine that the derivations of the previous section provide a reasonable description of flow around, accretion toward, and drag forces on the system's CM. In the opposite limit, when $a \gg R_{\mathrm{BH}}$, the binary is much wider than the gravitational focusing scale. In this case, we might expect that each object undergoes an essentially-isolated BHL interaction with the gaseous background. That is, the system evolves according to the BHL prescription for two independent objects (each of mass $\tfrac{1}{2} M$). In this limit, we would expect the accretion rate of the system and the total DF force on the binary to be $\propto (m_1^2 + m_2^2) = M^2/2$.

If we allow $a \sim R_{\mathrm{BH}}$, the two length scales are on the same order. Gas is focused toward both the individual objects and the system's CM. Orbital motion projects phase-dependent velocities for the individual objects with magnitude similar to that of the CM motion. Without a clear expectation for the flow structures in this intermediate regime, we turn to hydrodynamical simulations to provide a solution for the small- and large-scale structures that contribute to the evolution of the orbital and CM motion of the binary. The purpose of the remainder of this paper is to explore binary-BHL flow with varying a/R_{BH} and to characterize the evolution of a binary as a function of this ratio.

2.3. *Typical Encounters in Binary BHL*

Astrophysical binary systems span many orders of magnitude in mass and semi-major axis and these systems interact with a wide variety of ambient gases. In Table 1, we calculate a/R_{BH} for a sampling of binary systems moving through the ISM. For each gaseous medium in Table 1, we assume an isothermal ideal gas and calculate the sound speed as $c_{s,\infty} = \sqrt{k_B T / m_p}$. We see from the table that a stellar mass binary with a separation of 1 AU moving through the warm ISM may have a/R_{BH} values from several hundredths to a few times ten. Increasing the mass of the binary by a factor of ten gives results of $0.3 \lesssim a/R_{\mathrm{BH}} \lesssim 3$ when crossing the disk.

We discuss ambient gases of much greater density in Section 6. For example, a binary embedded in the model AGN disk presented in Section 6.4 may encounter number densities, n_∞, of 10^8 - 10^{14} cm^{-3}, depending on its radial location in the disk. A stellar mass binary with a separation of 1 AU located at a radius of 2 pc in this disk will have $a/R_{\mathrm{BH}} \approx 0.6$. The same binary embedded at a radius of 0.5 pc will have $a/R_{\mathrm{BH}} \approx 2.5$. As another example, we discuss in Section 6.5 a common envelope interaction in the triple system PSR J0337+1715 . We find that the models of Sabach & Soker (2015) imply envelope densities of $10^{16} \leq n_\infty \lesssim 10^{19}$ and the embedded binary would have $0.8 < a/R_{\mathrm{BH}} < 2.7$. The scal-

Table 1. a/R_{BH} in a variety of encounters.

Binary Type	Mass [$M_\odot$]	a	a/R_{BH}		
			Warm ISM		Hot ISM
			motion in plane of disk	*motion perpendicular to disk*	
Stellar Binary	1 + 1	2 $R_\odot$	5×10^{-3}	0.03 - 0.24	0.05 - 0.24
		1 AU	0.05	2.8 - 25	5 - 26
		0.05 pc	531	$10^4 - 10^5$	$10^4 - 10^5$
Massive Stellar Binary	10 + 10	30 $R_\odot$	7×10^{-4}	0.04 - 0.35	0.07 - 0.4
		1 AU	0.005	0.3 - 2.5	0.5 - 2.6
Binary Black Holes	30 + 30	10 $R_\odot$	8×10^{-5}	0.004 - 0.04	0.008 - 0.04
		100 $R_\odot$	8×10^{-4}	0.04 - 0.4	0.08 - 0.4
SMBHs	10^6 - 10^8	1 pc	$10^{-4} - 10^{-2}$	0.01 - 10	0.02 - 11
Double Planet	$3.7 M_{\mathrm{Jup}} + 3.7 M_{\mathrm{Jup}}$	3.9 AU	56	$10^3 - 10^4$	$10^3 - 10^4$

NOTE—The warm ISM consists of neutral and ionized gas and constitutes more than half of the volume of the ISM. We calculate the sound speed using $T = 10^4$ K (Kim & Ostriker 2017). For the warm ISM with motion in the plane of the disk, we assume the CM moves at $v_\infty = 10$ km s^{-1}, which would be the case for newly formed binaries in the plane of the disk (where the dispersion velocity is $\approx$ 10 - 50 km/s, Bovy et al. 2012). For the warm ISM with motion perpendicular to the disk, we use $v_\infty = 100 - 300$ km s^{-1}. This represents halo or bulge binaries crossing the disk plane. For the hot ISM, we use a temperature range of $T = 10^6 - 10^7$ K (Kim & Ostriker 2017) and a dispersion velocity of $v_\infty = 100$ km s^{-1} (Brown et al. 2010; Kafle et al. 2014).

ing with ρ_∞ in equation (13) indicates that the binary in one of these environments will transform 10 orders of magnitude more quickly than in the ISM.

3. NUMERICAL APPROACH

We perform simulations of supersonic BHL flows around an embedded binary system. The traditional approach to numerical studies of BHL is to perform simulations in the frame of a point mass by constructing a wind tunnel that sends gas flowing past a single, gravitating sink particle that is fixed at the coordinate origin. The sink particle accretes gas from the domain and the forces experienced by the sink particle due to the gas can be recorded at each time step. We modify this approach by instead placing two sink particles in orbit within a wind tunnel. The sink particles are free to move about the domain and we start the simulations in the initial frame of the CM of the binary. The sink particles accrete gas from the domain and actively respond to the forces they experience due to the gas. In the following subsections, we give a brief history of numerical studies of BHL that are most relevant to the current work, we describe our numerical method, and we outline the parameters chosen for the suite of simulations that we run.

3.1. *Previous Numerical Approaches to BHL*

BHL flows have a long history of hydrodynamical study, beginning with Hunt (1971), which has been reviewed by Edgar (2004) and Foglizzo et al. (2005). Of particular importance to our work are the studies of Ruffert & Arnett (1994);

Ruffert (1995, 1996, 1999), who performed Eulerian hydrodynamic simulations of BHL. They model the central, accreting boundary condition with a low-pressure sink that effectively absorbs all incoming material and removes it from the domain. These papers examine the effects of gas adiabatic index, Mach number, sink size, resolution, and the size of the computational domain on the rates of accretion and drag. They showed the qualitative features of BHL flows in 3D: a symmetric bow shock sets up in front of the accretor with an opening angle and standoff distance that are set by γ and $\mathcal{M}_\infty$. High-density material collects in a downstream wake from which material is accreted or is advected downstream. Quantitatively, they found higher accretion rates with smaller adiabatic index and with lower Mach number.

Ruffert's results, along with the more recent, higher resolution simulations of Blondin & Pope (2009); Blondin & Raymer (2012), have shown that accretion rates are also sensitive to the size of the computational domain, the size of the sink, and the resolution of the grid. We therefore studied those three aspects of our numerical setup before proceeding with our production runs. The results of those studies are presented in Appendix B.

In this paper, we use a very similar numerical approach to extend the efforts of Ruffert & Arnett (1994); Ruffert (1995, 1996, 1999); Blondin & Raymer (2012); MacLeod & Ramirez-Ruiz (2015); MacLeod et al. (2017); Murguia-Berthier et al. (2017) to binary systems by simulating two sink particles orbiting within a supersonic BHL flow. While methodologically distinct, we note that a similar scenario has

been simulated in 3D by Farris et al. (2010) in the ultra-relativistic regime in which a pair of black holes decays rapidly to merger while traversing through a surrounding gaseous medium.

3.2. *Notation for Two-Body Orbits*

Before we describe our numerical method in further detail, it is necessary to define the notation we will use to describe the orbit of the binary. We follow the notation of Hilditch (2001, Chapter 2) with the exception that we use M to represent the total mass of the binary. Let us summarize the quantities relevant to this paper. If $\mathbf{r}_1$ and $\mathbf{r}_2$ are the positions of m_1 and m_2, respectively, relative to the coordinate origin, then the CM is located at

$$\mathbf{R}_{CM} = \frac{m_1}{M}\mathbf{r}_1 + \frac{m_2}{M}\mathbf{r}_2. \tag{16}$$

Similarly, the velocity of the CM is

$$\mathbf{V}_{CM} = \frac{m_1}{M}\mathbf{v}_1 + \frac{m_2}{M}\mathbf{v}_2 \tag{17}$$

where $\mathbf{v}_1$ and $\mathbf{v}_2$ are the velocities of m_1 and m_2 relative to the origin. Consistent with Hilditch (2001), we use capital letters with subscripts for the barycentric quantities. The barycentric position and velocity of particle m_i are, respectively,

$$\mathbf{R}_i = \mathbf{r}_i - \mathbf{R}_{CM} \tag{18}$$

and

$$\mathbf{V}_i = \mathbf{v}_i - \mathbf{V}_{CM}. \tag{19}$$

The position of m_1 relative to m_2 is $\mathbf{r} = \mathbf{r}_1 - \mathbf{r}_2$ and the semi-major axis of this "relative" orbit is denoted by a. The semi-major axis of the barycentric orbit of m_1 is

$$a_1 = \frac{m_2}{M}a \tag{20}$$

and similarly for m_2. For a circular orbit, the orbital speed is

$$v_{orb} = \left(\frac{GM}{a}\right)^{1/2}. \tag{21}$$

3.3. *Hydrodynamical Setup*

We model BHL accretion onto a binary system moving relative to a uniform gas using FLASH (Fryxell et al. 2000). FLASH is an Eulerian hydrodynamic code with adaptive mesh refinement (AMR). We use FLASH's directionally-split Piecewise Parabolic Method Riemann solver (Colella & Woodward 1984). The gas pressure is defined by an ideal gas, gamma-law equation of state

$$P = (\gamma - 1)\rho\epsilon. \tag{22}$$

where ρ, ϵ, and γ are the density, internal energy, and adiabatic index of the gas, respectively. We initialize a 3D Cartesian grid with the coordinate origin at the center of the grid.

The size of the computational domain in x, y, and z is L, giving a domain volume of L^3.

We use the active sink particles (ASP) unit in FLASH (Federrath et al. 2010) to model the binary system. We represent the binary with two equal point masses, m_1 and m_2, placed at positions $\mathbf{r}_1$ and $\mathbf{r}_2$ relative to the grid. We begin the simulations with the CM of the binary at rest ($\mathbf{V}_{CM} = \mathbf{0}$) at the origin of the coordinate system ($\mathbf{R}_{CM} = \mathbf{0}$). The two masses are initialized in a circular orbit of semi-major axis a_0 in the $x-y$ plane with the orbital angular momentum vector pointing in the $+z$ direction. For comparison to single-particle BHL, we also include the option to place a single particle of mass M on the grid instead of a binary.

To model the supersonic motion of the binary relative to a uniform gas, we fill the domain with a wind of density ρ_∞ that flows in the $+x$ direction at speed v_∞. The wind speed is related to the sound speed, $c_{s,\infty}$, through the Mach number $\mathcal{M}_\infty = v_\infty/c_{s,\infty}$. The initial gas pressure is set according to

$$P_\infty = \frac{\rho_\infty c_{s,\infty}^2}{\gamma} = \frac{\rho_\infty}{\gamma\mathcal{M}_\infty^2}. \tag{23}$$

An inflow boundary condition at the $-x$ boundary of the computational domain replenishes this homogeneous wind throughout the simulation. All other boundaries of our computational domain have outflow conditions, which extrapolate the thermodynamic quantities and allow gas to freely leave and enter the domain. In our code units, $v_\infty = 1$. With this choice and $M = (2G)^{-1}$, $R_a = 2GM/v_\infty^2 = 1$. The result is a dimensionless setup with length unit R_a and time unit R_a/v_∞.

3.4. *Active Sink Particle Dynamics and Diagnostics*

We utilize many features built in to the ASP unit of FLASH with some additional diagnostics. See Federrath et al. (2010) for a complete description; we briefly describe our implementation here. The two massive particles that represent our binary system are gravitationally softened point masses surrounded by a spherical inflow boundary of radius R_s. The softening radius of each point mass is $0.4R_s$. Once initialized, each particle moves in response to gravitational accelerations from the other particle and the gas in the domain. The inflow boundary, or sink, that surrounds each particle removes gas from the domain. Once material falls into the sink, it is added to the sink particle properties and then it is deleted. This boundary condition represents perfectly efficient accretion without feedback. In our implementation of the ASP, we turn off the creation of new sink particles and we turn off self-gravity of the gas.

3.4.1. *Accreted Quantities*

Gas absorbed by sink particles carries mass and momentum, which are acquired by the particle. The accretion step is

performed by integrating the quantity over all cells within the volume of the sink and by adding the summed values to the particle's properties. To compute an accretion rate, we divide each accreted quantity by the time step. The accretion rates are recorded, then the accreted gas is deleted by setting the density within the sink cells to $\rho_{\text{sink}} = 10^{-2}\rho_{\infty}$, and setting all components of the gas velocity to zero. The mass accretion rate for particle m_i is calculated as a volume integral over the sink

$$\dot{m}_i = \frac{1}{\Delta t} \int_{\text{sink}_i} \left(\rho - \rho_{\text{sink}}\right) dV. \tag{24}$$

The total mass accretion rate for the binary is $\dot{M} \equiv \dot{m}_1 + \dot{m}_2$.

The accretion of linear momentum is integrated in each Cartesian coordinate. For particle i, this is given by

$$\dot{\mathbf{p}}_i = \frac{1}{\Delta t} \int_{\text{sink}_i} \mathbf{v}\left(\rho - \rho_{\text{sink}}\right) dV. \tag{25}$$

The accretion of linear momentum represents a force on each particle. We will denote these "momentum transport forces" on m_1 and m_2, respectively, as $\mathbf{F}_{\dot{p}_1}$ and $\mathbf{F}_{\dot{p}_2}$. Finally,

$$\mathbf{F}_{\dot{p}} = \mathbf{F}_{\dot{p}_1} + \mathbf{F}_{\dot{p}_2} \tag{26}$$

is the total momentum transport force on the binary CM.

3.4.2. *Dynamical Friction*

Each sink particle exerts a gravitational force on the gas, which restructures the gas in the domain. In turn, the redistributed gas exerts a gravitational force on each particle. This gravitational drag force, or gaseous DF, will occur whenever the gas distribution is not spherically symmetric about the particle. The total (vector) DF force acting on each particle is found by summing up the gravitational force on the particle due to each cell in the domain. Recalling that $\mathbf{r}_i$ is the location of m_i in the grid and letting $\mathbf{r}'$ denote the location of a particular gas cell, then the force on m_i due to the cell is

$$d\mathbf{F}_{\text{DF}_i} = -\frac{Gm_i\rho(\mathbf{r}')dV}{|\mathbf{r}_i - \mathbf{r}'|^3}\left(\mathbf{r}_i - \mathbf{r}'\right) \tag{27}$$

and the total DF force on m_i is the integral over the domain

$$\mathbf{F}_{\text{DF}_i} = -\int_{\text{domain}} \frac{Gm_i\rho(\mathbf{r}')dV}{|\mathbf{r}_i - \mathbf{r}'|^3}\left(\mathbf{r}_i - \mathbf{r}'\right). \tag{28}$$

The total DF force on the CM is

$$\mathbf{F}_{\text{DF}} = \mathbf{F}_{\text{DF}_1} + \mathbf{F}_{\text{DF}_2}. \tag{29}$$

3.4.3. *Particle Advancement*

The CM position and CM velocity of each particle is updated to account for the accreted gas. Before the gas is evolved further, each particle's motion is advanced using ASP's leapfrog integrator. The advancement step applies the momentum transport, DF, and sink-on-sink accelerations to each sink particle. At each time step, we record the accretion rates and forces as well as the total mass, position, and velocity of each particle.

3.5. *Simulation Parameters*

To summarize, the free physical parameters of our numerical setup are the background density ρ_{∞}, the flow Mach number $\mathcal{M}_{\infty}$, the adiabatic index γ, and the initial semi-major axis of the binary a_0. In order to study the effects of changing binary separation relative to the gravitational focusing scale, we vary a_0 while holding $\mathcal{M}_{\infty}$ and γ constant. We simulate seven values of a_0/R_a: 0.0, 0.16, 0.3, 0.41, 0.55, 0.74, and 1.0. Each of these simulations adopts $\rho_{\infty} = 10$, $\gamma = 5/3$, and $\mathcal{M}_{\infty} = 2$.

We have studied the effects of domain size, spatial resolution, and background density on our results. We present these validations of our method in Appendix B. As a result of these studies, we adopt the following in our production runs. We use a domain of volume $L^3 = (32R_a)^3$, with the CM of the binary initialized at the center. The base-level mesh consists of 4 blocks of 8^3 cells in the x, y, and z directions. We adaptively apply between 1 and 7 levels of refinement. The finest grid cells are $\delta_{\text{min}} = 0.016R_a$ wide in x, y, and z. The ASP unit maximally refines the region of each sink particle. We further instruct the AMR unit to refine on the second derivative of the internal energy of the gas. We run the simulations to $t = 50\,R_a/v_{\infty}$, which is $18\,R_a/v_{\infty}$ beyond the box-crossing time of the wind. We note that the $a_0 = 1.0R_a$ simulation falls in the $a \gtrsim R_{\text{BH}}$ regime since $1.0R_a = 1.25R_{\text{BH}}$.

4. NUMERICAL RESULTS

In this section, we describe the results of our gas dynamical simulations of binary-BHL flows. We analyze the morphology of these flows, the resultant accretion onto the individual members, and the forces on the binary CM and orbit.

4.1. *Flow*

The presence of a binary significantly alters the morphology of BHL accretion flows. At a given time, the manifestation of the binary's presence depends strongly on a_0 as compared to R_a, and on orbital phase. We explore these two aspects of BHL flows in the following subsections and in Figures 1, 2, 3, and 4. These figures show slices through the orbital ($z = 0$) plane.

4.1.1. *Binary Separation and Binary-BHL Flows*

Figure 1 illustrates the effect of semi-major axis on flow morphology. Here we plot density (in units of ρ_{∞}) for our single-particle simulation (upper left) and for binary simulations with 5 different values of semi-major axis. The single particle, with the same total mass as the binaries, represents the limit of zero binary separation ($a_0 \rightarrow 0.0R_a$).

The $a_0 = 0.0R_a$ snapshot of Figure 1 illustrates key features of canonical BHL flow. Supersonic motion relative to the background gas sets up an upstream bow shock front that funnels material into a downstream wake. The shock
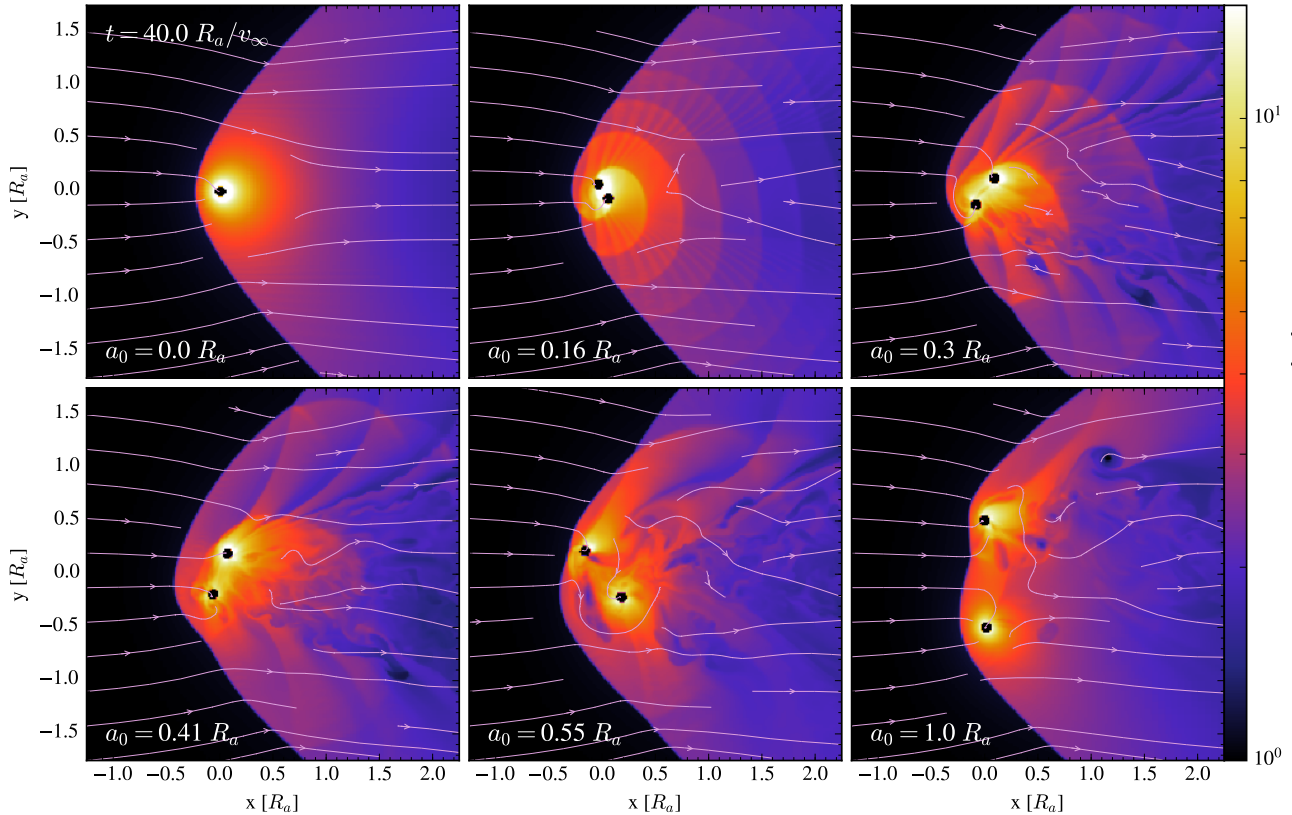
Figure 1. Comparison of binary flow morphology to single-particle BHL flow. Shown are density slices through the orbital (z=0) plane in units of ρ_∞ at time $t = 40.0 R_a/v_\infty$ with streamlines following the velocity field. The wind flows from left to right in these images. The axes are in units of $R_a = 2GMv_\infty^{-2}$, the accretion radius of the CM of the particle(s). These slices show the region of the orbiting pair; the full computational domain extends to $\pm 16 R_a$ in x, y, and z. The upper left snapshot shows BHL flow for a single particle of mass $M = (2G)^{-1}$. The remaining snapshots show the binary systems simulated, each with total mass $M = (2G)^{-1}$ but a different value of the initial semi-major axis, a_0. More compact binaries impart spiral shocks into the post-bow-shock region, but the impact of the binary on the shape of the overall bow shock increases with a_0.

front, which has an opening angle proportional to $c_{s,\infty}/v_\infty$, is smooth and axisymmetric about the line of motion of the point mass.

With the introduction of a binary, rather than a single, central object, some aspects of the flow remain similar while others diverge substantially. With $a_0 = 0.16R_a$, the size and shape of the primary shock remains very similar to that of $a_0 = 0.0R_a$. As a_0 increases, the effect of the binary on the overall bow shock structure becomes more apparent. By $a_0 = 1.0R_a$, each particle sets up its own primary shock (during parts of the orbit) and the overall structure is the superposition of the two shock cones.

Figure 1 also shows that the post-shock density and velocity structures are also modified by the presence of a binary. In the single-object case, the highest densities surround the accreting object. Flow converges in the wake and compresses as it falls inward toward the accretor. With increasing binary separation relative to R_a, we see that this density enhancement divides into separate convergences near m_1 and

m_2. This is particularly apparent in the $a_0 = 1.0R_a$ snapshot. We can understand this transition by considering that, with the division of the central object into a binary, the formally divergent potential at the origin (with $a_0 = 0.0R_a$) has been replaced by a potential that is softened on the scale of the binary separation. This restructuring of material in the post-shock region has implications for the rates of accretion and drag, which we discuss in detail in Sections 4.2 and 4.3.

Trailing the bow shock, flow is relatively smooth in the case of a single accretor. With the introduction of a binary, orbital motion imparts new features on the post-shock flow. For compact binary separations (e.g. $a_0 = 0.16R_a$) some of the primary features are spiral shocks launched because the orbital motion of the binary is supersonic relative to the surrounding gas. These features are most apparent in Figure 2, in which we plot the velocity divergence, $\nabla \cdot \mathbf{V}_{gas}$. Shocked material is revealed in purple in the figure, where $\nabla \cdot \mathbf{V}_{gas} < 0$ indicates abrupt convergence of gas at a shock front. Especially for the binaries with $a_0 = 0.16R_a$ and $a_0 = 0.3R_a$, spiral
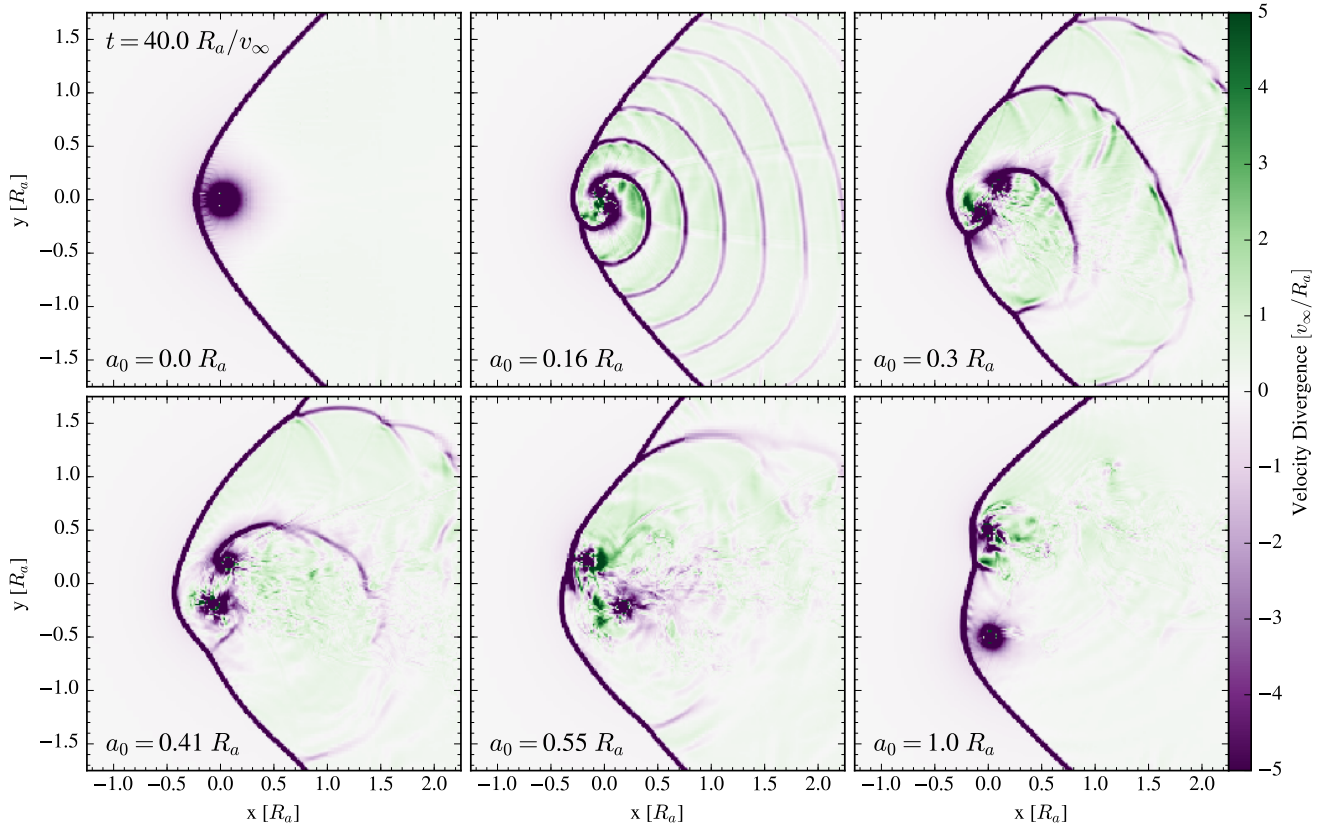
Figure 2. Same as in Figure 1, except that here we plot velocity divergence, $\nabla \cdot \mathbf{V}_{\text{gas}}$. Shades of purple highlight shocked material, where $\nabla \cdot \mathbf{V}_{\text{gas}} < 0$. Secondary shocks form in the vicinity of particles in supersonic relative motion. The increasing orbital period with increasing a means that the secondary shocks are absent by $a_0 = 1.0 R_a$.

shocks propagate outward away from the binary and are advected downstream in the wake.

As the binary separation increases, the relative velocity between the binary object's orbital motion and the gas decreases. The particle moving through $-y$ positions transitions to subsonic relative motion first, since the particle in the lower half of the orbit moves in the same direction as the gas. This transition to subsonic relative motion is visible in the bottom row of Figure 2 through the disappearance of the leading shock front and in Figure 1 through the symmetric density distribution around the object. In the $a_0 = 0.41 R_a$ slice of Figure 2, the secondary shock ahead of the lower particle is barely discernible. By $a_0 = 1.0 R_a$, both secondary shocks are absent and the only inflection of the binary envelope is from the superposition of *two* primary shock fronts. Here, all orbital motion of the binary is subsonic relative to the post-shock sound speed.

4.1.2. *Time-Dependent Properties of the Flow*

In the simulations involving a binary central object, orbital motion imparts time-variability and orbital phase dependence on the flow structure. We examine those features in detail here. Figures 3 and 4 show time series of the flow for $a_0 =$

$1.0 R_a$ and $a_0 = 0.41 R_a$, respectively. In both of these time series, we show the binary over half of an orbit only. The second half of each orbit is qualitatively similar to the first, except that the roles of m_1 and m_2 are reversed.

Figure 3 shows $a_0 = 1.0 R_a$ over the half-orbit that begins at $t = 42.1 R_a/v_\infty$. In the first image, m_1 is fully upstream from m_2. Although at this instant the particles lie along a line parallel to the wind direction (at ∞), the bow shock is not symmetric about this line but carries distortions that highlight the preceding orbital motion of the binary. We will trace the origin of this distortion through the remaining snapshots of Figure 3.

Situated downstream, m_2 interacts with material that has already been influenced by m_1. This dense, lower-velocity material piles up around m_2, resulting in a higher-than-average, and almost spherical, density distribution about m_2. This density enhancement remains with m_2 as time advances across the upper row of Figure 3, approaching the primary bow shock by the first image of the second row.

At $t = 43.7 R_a/v_\infty$, a second shock front is forming ahead of m_2 as the particle approaches its greatest velocity relative to the gas. Between this snapshot and the next, m_2 crosses the
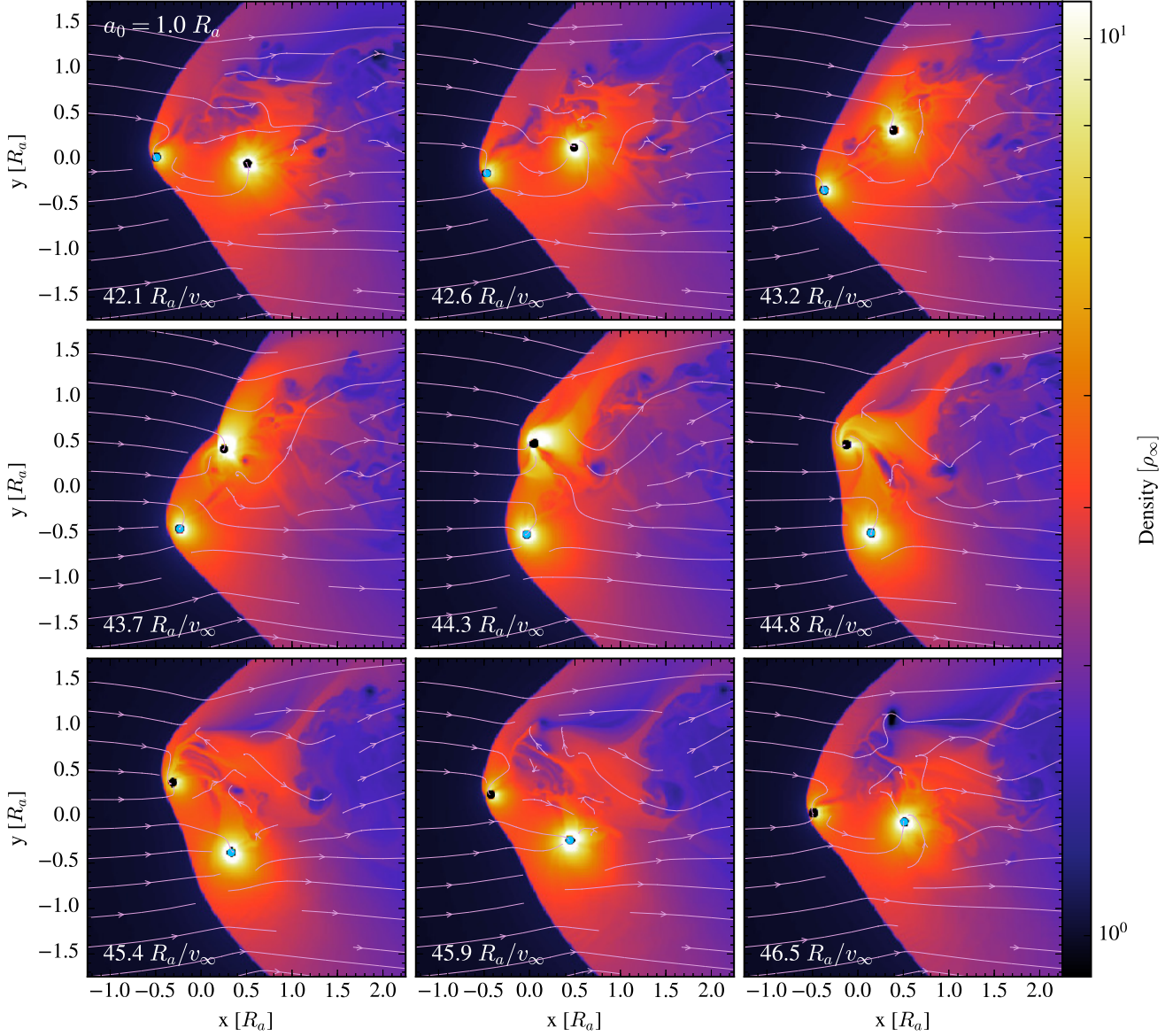
Figure 3. Flow morphology over half of an orbit for the $a_0 = 1.0R_a$ simulation. As in Figure 1, we show density slices of a $3.5R_a \times 3.5R_a$ section of the orbital plane. The simulation time is shown in the lower-left corner of each snapshot and we have marked m_1 with a blue dot and m_2 with a black dot. The overall shape of the primary shock front responds to the rotation of the oblique potential of two particles with finite separation. The density distribution about each particle is heavily influenced by the motion of the particle relative to the wind. In this series, m_1 moves in the $+x$ direction, as does the wind, so has a lower speed relative to the gas. m_2 moves in the $-x$ direction, head-on into the wind. The downstream particle interacts with material that has already interacted with its binary companion (see m_1 in the last two snapshots).

leading boundary of the bow shock of m_1. The over-density that has been carried along by m_2 remains with the particle during the crossing. In the next two images ($t = 44.3$ and $44.8\ R_a/v_\infty$), this dense material is impacted by the incoming wind. By $t = 45.4 R_a/v_\infty$ (first panel of third row), the over-density is largely detached from m_2 and is being pulled into the approaching potential well of m_1. In the same panel, a bridge of material connects the two particles and, for the

first time in these snapshots, the density enhancement about m_1 is greater than that of m_2.

Two flow properties transition in the last row of Figure 3. First, the dense material that is attached to m_2 at $t = 45.4 R_a/v_\infty$ becomes fully detached from the particle as the downstream region is increasingly dominated by the gravitational pull of m_1. Second, as m_2 moves down and to the left, the shock set up by the particle rotates with it, leading the $+y$

portion of the bow shock to protrude further upstream than the $-y$ portion.

Figure 4 shows the $a_0 = 0.41 R_a$ binary for the half-orbit beginning at $t = 40.1 R_a/v_\infty$. We additionally annotate several features, which will be referenced here. As discussed in the context of Figure 2, the particle traveling up wind through the post-bow-shock material launches a secondary spiral shock wave behind the primary shock.

The interaction of the binary with spiral shocks sets up the fan-like structures emanating from the binary in Figure 4. Material crossing the primary shock interacts with each particle twice, resulting in four fan structures per orbit. In the first snapshot ($t = 40.1 R_a/v_\infty$), the particles are located at $x \approx 0$. There is a large stand-off distance between the primary shock and the binary. Behind the primary shock, a secondary shock is set up in front of m_1. We label these structures "1" and "2", respectively, in all of the snapshots shown, so that one can follow each structure over time. From $t = 40.2$ to $40.3 R_a/v_\infty$, shock 1 is deflected due to the gravitational pull of m_1. By $t = 40.4 R_a/v_\infty$, shock 2 is pushed past shock 1 by m_1 as the particle advances in the $-x$ direction. From $t = 40.6$ to $t = 41.0 R_a/v_\infty$, m_2 advances toward $+y$ values and shock 1 is defected by the gravitational pull of m_2. At $t = 41.2 R_a/v_\infty$, a new secondary shock (set up by m_2 and labeled "3" in Figure 4) crosses shock 1 as shock 1 continues to advect downstream. In the final image, shock 3 is advancing to meet shock 2, and will cross shock 2 as the orbit continues.

In addition to the fan structures, the density very close to the binary is of interest. In particular, it appears that the particle at $+y$ positions exhibits a higher local density than its counterpart at $-y$ values. A persistent bridge of dense material always connects the two particles, giving a slightly higher density enclosed by the orbit than in the $a_0 = 1.0 R_a$ simulation.

4.2. Accretion

In this section, we examine instantaneous and orbit-integrated accretion rates onto the objects.

4.2.1. Instantaneous Accretion Rates

In Figure 5, we plot the instantaneous accretion rates versus time for $a_0 = 0.16, 0.41$, and $1.0 R_a$ for simulation times $\geq 30 R_a/v_\infty$. As expected from prior studies of canonical BHL accretion (with $R_s = 0.05 R_a$, $\mathcal{M}_\infty \sim 2$, and at our resolution), $\dot{M}(a_0 = 0) \approx 0.7 \dot{M}_{HL} \approx 1.0 \dot{M}_{BH}$ (Ruffert 1994; Blondin & Raymer 2012).

Although $\dot{M}(a_0 = 0)$ reaches a steady state, the accretion rates for the members of the binary systems are periodic. For the tightest binary, $a_0 = 0.16 R_a$, $\dot{m}_1$ and $\dot{m}_2$ are exactly out of phase, each with an accretion rate that follows the orbital period. As such, $\dot{M}$ is almost constant in time and approaches

$\dot{M}(a_0 = 0)$. For more widely separated binaries, the individual accretion rates of the two particles no longer sum to a constant value. In the case of $a_0 = 1.0 R_a$, $\dot{m}_1$ shows a sharp spike once per orbit before declining to a minimum value, then the rate climbs to a local maxima before the next sharp spike in accretion. While the curve for $\dot{m}_2$ looks very similar, the variation in $\dot{M}$ reveals that the individual accretion rates are not exactly out of phase. In the case of $a_0 = 0.41 R_a$, the individual accretion rates reveal one peak and one valley per orbit with transitions between the two that are variable from one orbit to the next. In addition, $\dot{m}_1$, for example, reveals a slight overall increase and decrease over many orbits. The superposition of these trends in $\dot{m}_1$ and $\dot{m}_2$ yields an $\dot{M}$ that has irregularly spaced peaks and valleys with variation from orbit to orbit.

Let us now connect features of the accretion rates depicted in Figure 5 to the flow morphology discussed in Section 4.1.2. In Figure 6, we show $\dot{m}_1$, $\dot{m}_2$, and $\dot{M}$ for the $a_0 = 1.0 R_a$ simulation for simulation times $t = 39.9$ to $48.7 R_a/v_\infty$, as in the panels of Figure 3. In the first row of Figure 3, m_2 moves from a position directly downstream from m_1 at $t = 42.1 R_a/v_\infty$ into a lower-density pocket behind the primary shock by $t = 43.2 R_a/v_\infty$. Figure 6 reveals a decreasing accretion rate for m_2 during the same period of time. Although m_2 has carried along higher-density material during this time interval, the material is able to expand into the low-density region behind the primary shock, giving rise to the local minimum in $\dot{m}_2$ at $t \approx 43.2 R_a/v_\infty$.

Between $t = 43.2$ and $43.7 R_a/v_\infty$, m_2 has turned into the oncoming wind and approaches the primary shock front; the particle nears its highest velocity relative to the gas at $t = 43.7 R_a/v_\infty$ and a second shock front forms in front of m_2. Meanwhile, the high-density concentration that has followed m_2 is now stopped by this second shock and a stream of material flows from m_1 to m_2. This confluence of flow gives $\dot{m}_2$ a sharp peak at $t = 43.7 R_a/v_\infty$.

By $t = 44.3 R_a/v_\infty$, m_2 has crossed the primary bow shock of m_1, and now $\dot{m}_2$ declines. From $t = 44.3$ to $44.8 R_a/v_\infty$, m_2 begins to lose the high-density clump that has followed the particle since its time downstream from m_1. $\dot{m}_2$ bottoms out as the clump of material finally detaches from m_2 and is swept down stream ($t = 45.4$ to $46.5 R_a/v_\infty$). At the same time, m_1 is moving into a position downstream from m_2. There is an increase in $\dot{m}_1$ from $t = 44.3$ to $45.9 R_a/v_\infty$ as m_1 moves with its slowest relative velocity compared to the surrounding gas and interacts with dense material stripped from the vicinity of m_2. From 45.9 to $46.5 R_a/v_\infty$, $\dot{m}_1$ declines slightly as the clump of material that has detached from m_2 crosses outside of the orbit of m_1 as it is advected downstream and out of reach.

Figure 7 shows the accretion rates for the $a_0 = 0.41 R_a$ simulation for the time period $t = 39.6$ to $t = 41.9 R_a/v_\infty$,
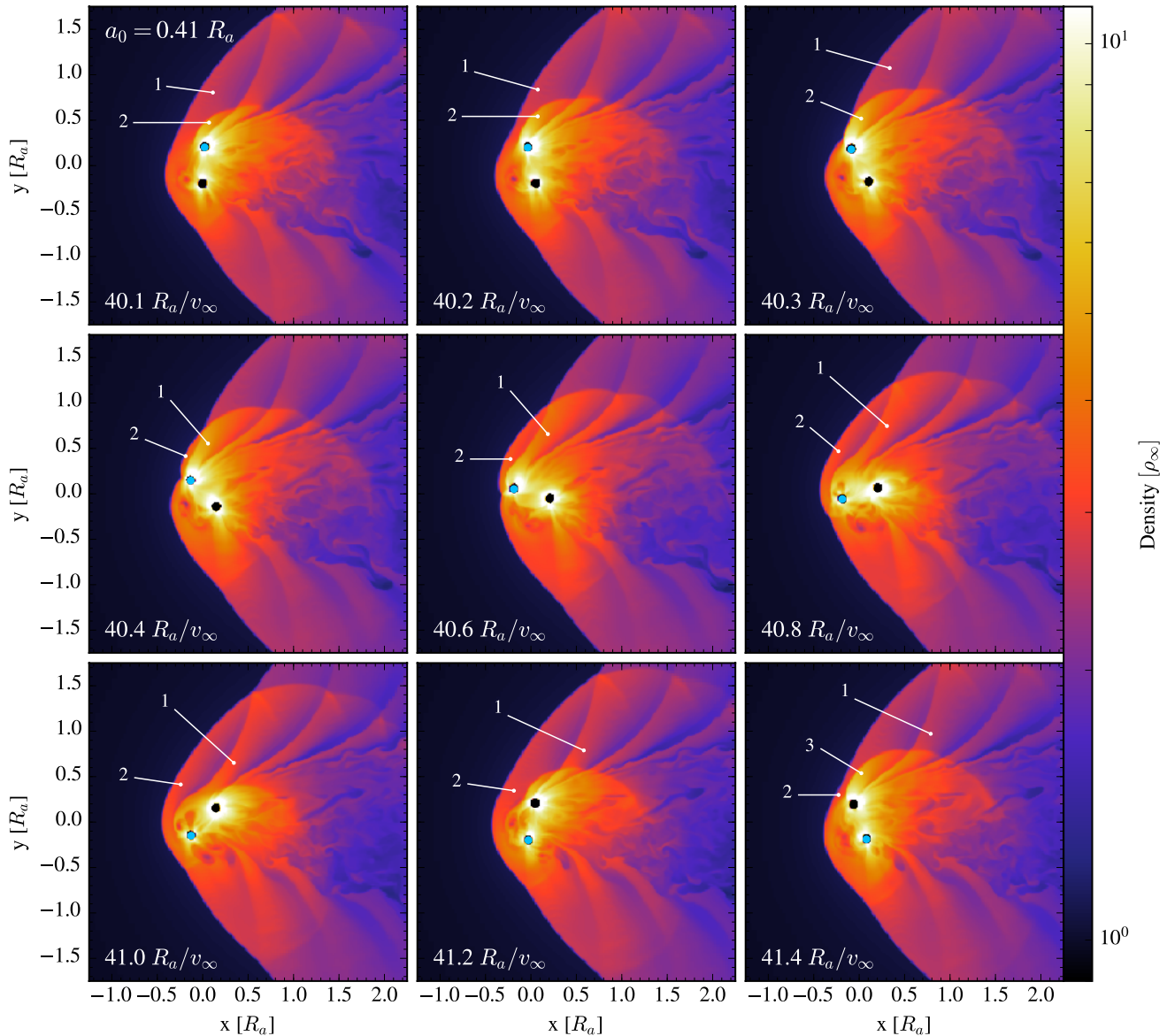
Figure 4. Same as in Figure 3, but for the $a_0 = 0.41 R_a$ simulation. We observe curved fan structures that arise four times each orbit which are discussed in detail in the text.

also shown in the snapshots of Figure 4. From $t = 40.1$ to $40.8 R_a/v_\infty$, $\dot{m}_2$ steadily increases as m_2 moves in the same direction as the flow. At $40.8 R_a/v_\infty$, m_2 turns upstream. There is a steepening of $\dot{m}_2$ to a maximum at $41.0 R_a/v_\infty$ as m_2 deflects shock 1 while also stripping material from the region surrounding m_1. Between 41.0 and 41.2 R_a/v_∞, shock 3 forms in front of m_2. Once this material crosses shock 1 (at $41.2 R_a/v_\infty$), it expands into the lower-density region behind shock 2, reducing the rate of accretion onto m_2.

Meanwhile, m_1 experiences a decreasing accretion rate from $t = 40.1 R_a/v_\infty$ to $t = 40.8 R_a/v_\infty$ as the particle takes up a position in front of m_2. There is a flattening of $\dot{m}_1$ from $t = 40.2$ to $40.3 R_a/v_\infty$ when shock 1 is pulled into m_1 and shock 2 crosses shock 1. The overall decrease in $\dot{m}_1$ continues through $t = 40.8 R_a/v_\infty$ while m_1 is in the upstream position and m_2 pulls material away from m_1. Just before $t = 40.8 R_a/v_\infty$, the slope of $\dot{m}_1$ turns positive as m_1 moves to $-y$ values. There, m_1 moves in the same direction as the wind, reducing the relative motion between the particle and

Figure 5. Instantaneous accretion rates over time for the binaries with $a_0 = 0.16R_a$ (left panel), $a_0 = 0.41R_a$ (center panel), and $a_0 = 1.0R_a$ (right panel). The individual accretion rates, $\dot{m}_1$ and $\dot{m}_2$, and the total rate of accretion, $\dot{M} = \dot{m}_1 + \dot{m}_2$, are shown. The orbital period of each binary is included for reference. On each panel, the dashed line indicates the steady-state accretion rate realized in the single-particle simulation, $a_0 = 0.0R_a$. The individual accretion rates for the $a_0 = 0.16R_a$ binary sum to an almost constant value, while the total accretion rates for $a_0 = 0.41R_a$ and $a_0 = 1.0R_a$ exhibit significant time variability. The wider binaries experience lower accretion rates than the tightest binary, whose total accretion rate approaches that of the single particle simulation.
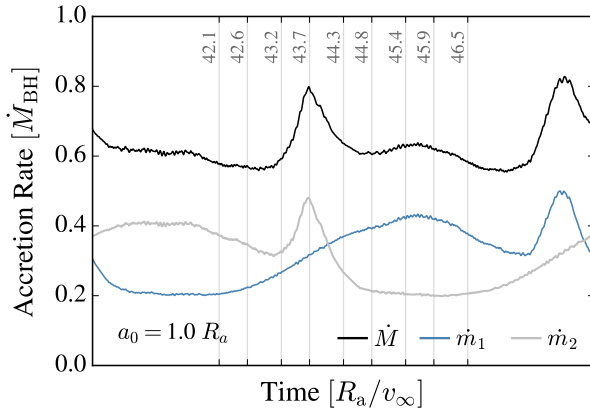
Figure 6. As in the right panel of Figure 5, instantaneous accretion rates are shown for the $a_0 = 1.0R_a$ binary. Here we focus on one orbit of the binary, which begins at $t = 39.9R_a/v_\infty$. Each vertical line corresponds to one of the density snapshots of Figure 3.

Figure 7. Instantaneous accretion rates for the $a_0 = 0.41R_a$ binary for a single orbit, beginning at $t = 39.6R_a/v_\infty$. Each vertical gray line corresponds to one of the density snapshots of Figure 4.

the gas. From there the cycle depicted in Figure 4 begins again, but this time with the roles of m_1 and m_2 reversed.

4.2.2. *Orbit-Averaged Accretion Rates*

Having examined the origins of time-variable accretion rates in binary-BHL flows, we now compare time-integrated quantities for binaries of varying separation.

It is apparent from Figure 5 that $\dot{m}_1$, $\dot{m}_2$, and $\dot{M}$ for $a_0 = 0.41$ and $1.0R_a$, are lower than the corresponding accretion rates in the $a_0 = 0.16R_a$ case. To look for trends in the accretion rate as a function of a_0, let us compare the time-averaged total accretion rate for each pair. We use angled brackets, $\langle \rangle$, to indicate quantities averaged over an integer number of orbits. Each time average begins at $t = 30R_a/v_\infty$ and termi-
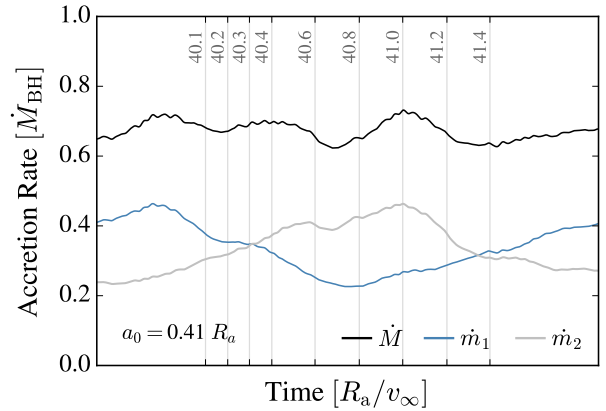
nates at the end of the last complete orbit before the end of the simulation ($t = 50R_a/v_\infty$). The $a_0 = 1.0R_a$ binary (with $P_{\text{orb}} \approx 8.89\,R_a/v_\infty$) completes two full orbits during this time. The $a_0 = 0.16R_a$ binary completes 33 full orbits.

In Figure 8, we plot the orbit-averaged total accretion rate versus a_0. As the binary separation decreases, $\langle \dot{M} \rangle$ approaches $\dot{M}_{\text{BH}} \propto M^2 \propto (m_1 + m_2)^2$. That is, binaries of smaller separations accrete like a single particle of mass $m_1 + m_2$. Wider binaries, on the other hand, have a lower accretion rate and fall closer to $\langle \dot{M} \rangle = 0.5\dot{M}_{\text{BH}}$, which assumes that m_1 and m_2 accrete independently of one another. To see where the factor of 0.5 comes from, let us write the BH accretion rate for $m_1 = M/2$:

$$\dot{M}_{\text{BH},1} = \frac{4\pi G^2 m_1^2 \rho_\infty}{(v_\infty^2 + c_{s,\infty}^2)^{3/2}} = \frac{4\pi G^2 (M/2)^2 \rho_\infty}{(v_\infty^2 + c_{s,\infty}^2)^{3/2}} = \frac{1}{4}\dot{M}_{\text{BH}}. \quad (30)$$
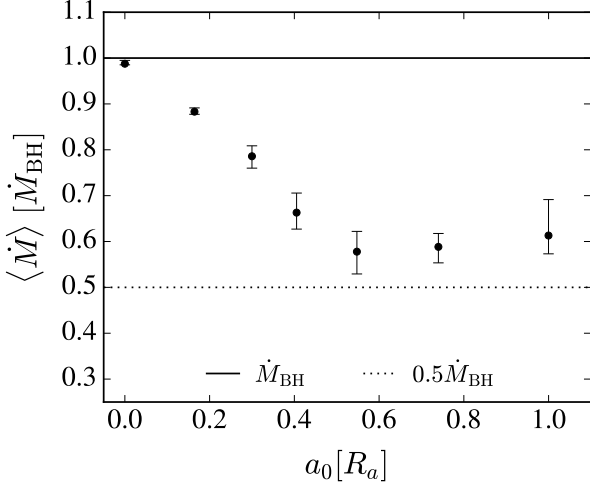
Figure 8. Orbit-averaged total accretion rate, $\langle \dot{M} \rangle$, in units of $\dot{M}_{\mathrm{BH}}$ versus a_0, in units of R_a. The black points show the median of $\dot{M}(t)$ for each binary over an integer number of orbits between $t = 30 R_a/v_\infty$ and $t = 50 R_a/v_\infty$. The error bars show the 15.87th to 85.13th percentile range about the median, driven by periodic variations with orbital phase. At smaller separations, the accretion rate approaches that of a single particle with $\langle \dot{M} \rangle \approx \dot{M}_{\mathrm{BH}} \propto M^2$, while at larger separations, the accretion rate approaches that of two independent particles with $\langle \dot{M} \rangle \approx \dot{M}_{\mathrm{BH,independent}} \propto (m_1^2 + m_2^2)$.

Because $m_2 = M/2 = m_1$, $\dot{M}_{\mathrm{BH},2} = \dot{M}_{\mathrm{BH},1}$. Then the total accretion rate for the pair (treating them as independent particles) is $\dot{M}_{\mathrm{BH,independent}} = 0.25\dot{M}_{\mathrm{BH}} + 0.25\dot{M}_{\mathrm{BH}} = 0.5\dot{M}_{\mathrm{BH}}$. For more general m_1 and m_2, we would say that since $\dot{M}_{\mathrm{BH},1} \propto m_1^2$ and $\dot{M}_{\mathrm{BH},2} \propto m_2^2$, $\dot{M}_{\mathrm{BH,independent}} \propto (m_1^2 + m_2^2)$.

4.3. *Forces*

When either a single object or binary moves through a gaseous medium, it restructures the distribution of the surrounding gas. The restructured gas exerts forces on the CM and components of the binary. In this section, we describe how these forces are calculated from our numerical simulations and we show an example calculation for our $a_0 = 0.41 R_a$ simulation.

4.3.1. *Forces on the Center of Mass*

First, let us consider how the forces change the translational motion of the binary CM. At each time step, we calculate the DF and momentum transport forces acting on each particle. The DF forces on m_1 and m_2 are calculated according to equation (28), while the momentum transport forces are calculated according to equation (25). We can ask how these forces influence the motion of the CM by considering the component of each force along the CM velocity relative to the gas.

The velocity of the CM relative to the grid is $\mathbf{V}_{\mathrm{CM}}$ and the velocity of the wind relative to the grid is $\mathbf{v}_\infty = v_\infty \hat{x}$, so the velocity of the CM relative to the gas is $\mathbf{V}_{\mathrm{rel}} = \mathbf{V}_{\mathrm{CM}} - \mathbf{v}_\infty$. Letting $\hat{V}_{\mathrm{rel}}$ be the unit vector in the direction of $\mathbf{V}_{\mathrm{rel}}$, the scalar component of the DF and momentum transport forces along $\mathbf{V}_{\mathrm{rel}}$ are, respectively,

$$F_{\mathrm{DF,CM}} \equiv \left(\mathbf{F}_{\mathrm{DF}_1} + \mathbf{F}_{\mathrm{DF}_2} \right) \cdot \hat{V}_{\mathrm{rel}} \qquad (31)$$

and the momentum transport force on the CM is

$$F_{\dot{p},\mathrm{CM}} \equiv \left(\mathbf{F}_{\dot{p}_1} + \mathbf{F}_{\dot{p}_2} \right) \cdot \hat{V}_{\mathrm{rel}}. \qquad (32)$$

Notice that $F_{\mathrm{DF,CM}}$ and $F_{\dot{p},\mathrm{CM}}$ may be positive or negative. A positive value indicates a net thrust while a negative value exerts a net drag. The net force on the CM,

$$F_{\mathrm{net,CM}} = F_{\mathrm{DF,CM}} + F_{\dot{p},\mathrm{CM}}, \qquad (33)$$

is the total drag (or thrust) that results from the sum of the two projections.

Figure 9 shows the forces on the CM of the $a_0 = 0.41 R_a$ binary from $t = 30 R_a/v_\infty$ until the end of the simulation. The top panel shows the DF forces on the CM, equation (31). The contribution due to m_1 is $\mathbf{F}_{\mathrm{DF}_1} \cdot \hat{V}_{\mathrm{rel}}$, while the contribution from m_2 is $\mathbf{F}_{\mathrm{DF}_2} \cdot \hat{V}_{\mathrm{rel}}$. The periodic modulation of the blue and grey curves is due to the orbital motion of each particle. Even though the density structure at large scales is relatively stable, the position and velocity of each particle relative to the gas distribution changes as the particles complete each orbit. This gives rise to a changing angle between each force vector and $\hat{V}_{\mathrm{rel}}$ as well as a changing magnitude of the force vectors themselves ($\mathbf{F}_{\mathrm{DF}_1}$ and $\mathbf{F}_{\mathrm{DF}_2}$). In the same panel, $F_{\mathrm{DF,CM}}$ (in black) also shows variation due to the orbital motion about a nearly constant value of -4.2 F_{BH}, which is less than the single-particle value of -5.1 F_{BH}. Overall, the negative value of $F_{\mathrm{DF,CM}}$ indicates that the large-scale structure always exerts a drag on the CM motion of the pair.

The center panel of Figure 9 shows the momentum transport forces acting along the CM motion of the binary, which are calculated according to equation (32). The m_1 and m_2 curves show $\mathbf{F}_{\dot{p}_1} \cdot \hat{V}_{\mathrm{rel}}$ and $\mathbf{F}_{\dot{p}_2} \cdot \hat{V}_{\mathrm{rel}}$, respectively. The blue and grey curves dip to negative values when accreted material is moving opposite the CM motion of the particle. Their sum is always positive, though, so the momentum transport force always exerts a net thrust on the CM. This is similar to the single-particle case, although the median value of $|F_{\dot{p},\mathrm{CM}}| \approx 0.18 \, F_{\mathrm{BH}}$ is 74% less than the magnitude of the single-particle value of 0.69 F_{BH}. Finally, the bottom panel of Figure 9 shows the net force on the CM, given by equation (33). The combination of DF and momentum transport forces always exerts a drag on the CM. The orbit-averaged net force on the CM for the $a_0 = 0.41 R_a$ binary is -4.06 F_{BH}, a value that is only 7% lower than in the single-particle case.
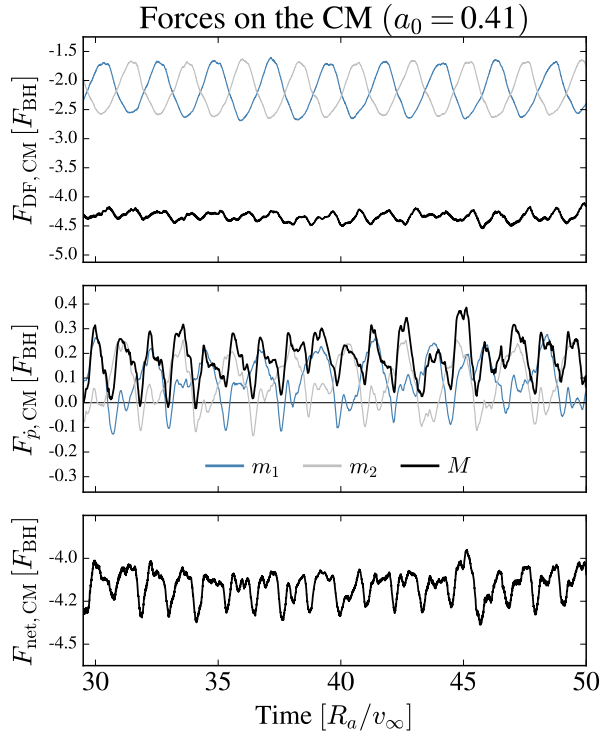
4.3.2. *Forces on the Orbital Motion*

Figure 9. Center of mass forces over time for the $a_0 = 0.41R_a$ binary. In the upper and middle panels, we show the DF and momentum transport forces, respectively, acting along the CM velocity vector relative to the wind, $\hat{V}_{\text{rel}}$. The blue and grey curves show the contributions from m_1 and m_2, respectively, to the total of each type of force (black curve). The bottom panel is the total force on the CM due to both DF and momentum transport. In each panel, a positive value indicates a net thrust of the CM while a negative value indicates a net drag on the CM. The DF force arising from the downstream wake dominates the total force on the CM of the binary. At all times, this net drag force acts to slow down the translational motion of the CM relative to the background gas.

We now consider the forces affecting the motion of the binary *about* the CM. To do this, we find the projections of the forces along the barycentric velocity vectors of the two particles. The barycentric velocities of m_1 and m_2 are $\mathbf{V}_1$ and $\mathbf{V}_2$, respectively (equation (19)). The unit vectors in the directions of these velocities are then $\hat{V}_1 = \mathbf{V}_1/V_1$ and $\hat{V}_2 = \mathbf{V}_2/V_2$. The DF force on the orbital motion of the binary is

$$F_{\text{DF,orb}} \equiv \mathbf{F}_{\text{DF}_1} \cdot \hat{V}_1 + \mathbf{F}_{\text{DF}_2} \cdot \hat{V}_2 \tag{34}$$

and the momentum transport force on the orbit is

$$F_{\dot{p},\text{orb}} \equiv \mathbf{F}_{\dot{p}_1} \cdot \hat{V}_1 + \mathbf{F}_{\dot{p}_2} \cdot \hat{V}_2, \tag{35}$$

which gives a net "orbital" force of

$$F_{\text{net,orb}} = F_{\text{DF,orb}} + F_{\dot{p},\text{orb}}, \tag{36}$$

which is the force projected along the objects' respective directions of orbital motion.
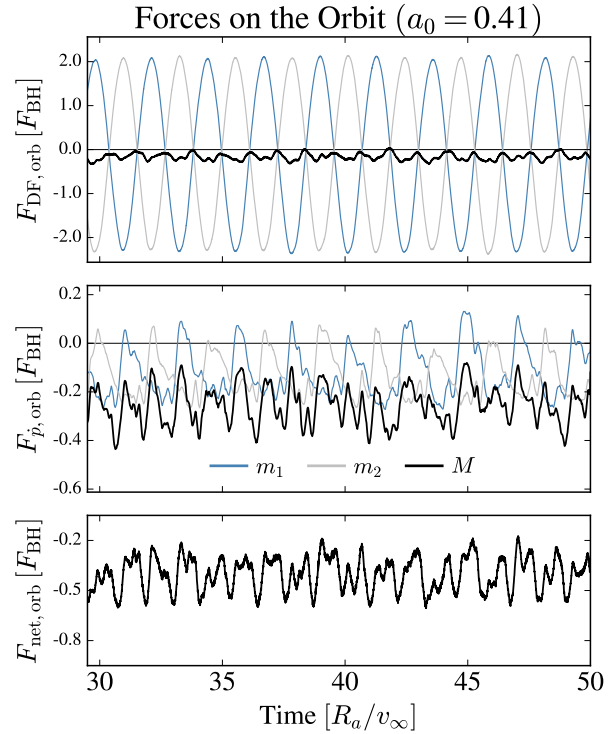
Figure 10. Orbital forces over time for the $a_0 = 0.41R_a$ binary. Same as in Figure 9, except that we plot the projections of the forces along the barycentric velocities of m_1 and m_2. Both DF and momentum transport cause a net drag on the orbital motion at all times. Momentum transport and DF contribute almost equally to the overall drag on the motion. The flow at small scales in the vicinity of the orbiting binary cannot be neglected, as momentum accretion contributes nearly half of the overall drag on the orbital kinetic energy of the binary.

In Figure 10, we show these orbital forces calculated for $a_0 = 0.41R_a$. The DF forces, $\mathbf{F}_{\text{DF}_1} \cdot \hat{V}_1$ and $\mathbf{F}_{\text{DF}_2} \cdot \hat{V}_2$, shown in the upper panel of Figure 10, show a sinusoidal fluctuation between large negative and positive values. Because the overdense wake located at positive x values remains the primary driver of DF forces, this periodic change in the sign of $F_{\text{DF,orb}}$ is dominated by the changing direction of the barycentric velocities over each single orbit. The net force on the orbit due to DF (black curve in the upper panel) is small and negative, always exerting a small drag on the orbit.

The momentum accretion forces, $\mathbf{F}_{\dot{p}_1} \cdot \hat{V}_1$ and $\mathbf{F}_{\dot{p}_2} \cdot \hat{V}_2$, shown in the center panel of Figure 10, exhibit more complex behavior throughout the orbit. Consider the blue curve, for m_1. The momentum accretion often causes a drag on the orbital motion of m_1. The most negative value (largest drag force) occurs while m_1 is moving in the same direction as the wind (for example, the bottom three panels of Figure 4). At some instances, the blue curve turns positive. This occurs when m_1 is traveling head-on into the wind. At this time,

m_1 is moving supersonically relative to the material behind the primary shock. The sharp (positive) peaks in the blue curve occur when a secondary shock forms ahead of m_1 (as in the first snapshot Figure 4). In these cases, m_1 shocks and focuses material locally, accreting some of this material from downstream relative to its instantaneous motion. Because this material is moving in the same direction as m_1 as it is accreted, it imparts a thrust.

Although the momentum transport forces on m_1 and m_2 are sometimes positive, these forces always sum to a negative value (black curve in the middle panel of Figure 10). This reflects the fact that, in the case of $a_0 = 0.41 R_a$, the highest accretion rates happen during the subsonic portions of the orbit of each particle. Material accreted from upstream exerts a drag force on each particle's orbital motion, and the overall result of momentum accretion is a net drag on the orbit.

The net force on the orbit due to both momentum accretion and DF (bottom panel of Figure 10) is always negative (a drag). Momentum accretion contributes nearly half of the drag force on the orbit. We note that momentum accretion is a local phenomenon that depends on the details of the flow in the region of the orbiting binary. An understanding of the longterm evolution of the orbit of an astrophysical binary, therefore, requires an understanding of the dynamics and microphysics at small scales. This conclusion can be contrasted to the CM forces shown in Figure 9, in which the forces are dominated by the DF force, which results from the large-scale structure of the gas.

5. ANALYSIS: TIMESCALES FOR BINARY TRANSFORMATION

A binary interacting with an ambient gas will transform as a result of drag and accretion. The mass of the binary grows by accretion over a timescale $M/\dot{M}$. Forces on the CM reduce the CM kinetic energy, $E_{\text{trans}} = M\mathbf{V}_{\text{CM}}^2/2$, over a timescale $E_{\text{trans}}/\dot{E}_{\text{trans}}$. Forces on the binary orbit tighten the separation over a timescale $a/\dot{a}$. In this section we explore these timescales and their hierarchy. We first derive analytic results from BHL theory as context, then discuss the numerical results from our simulation models.

5.1. *Analytical Timescales*

Before turning to our numerical simulations, let us see what the BHL formalism tells us about these timescales. The BHL stopping timescales are $\tau_{\text{stop,HL}}$ and $\tau_{\text{stop,BH}}$ (equations (6) and (13), respectively) with $M = m_1 + m_2$. Similarly, the accretion timescales are $\tau_{\text{accr,HL}}$ and $\tau_{\text{accr,BH}}$, given by equations (7) and (14), respectively, with $M = m_1 + m_2$.

We derive expressions for the BHL inspiral timescales in Appendix A. For large Mach numbers, the HL characteristic scalings give an orbital inspiral time that can be expressed in terms of the stopping time,

$$\tau_{\text{insp,HL}} = \frac{\tau_{\text{stop,HL}}}{8\sqrt{2}} \left(\frac{a}{R_a} \right)^{-3/2}. \tag{37}$$

In the regime of mild Mach numbers, the BH formalism gives an orbital inspiral time of

$$\tau_{\text{insp,BH}} = \frac{\tau_{\text{stop,HL}}}{8\sqrt{2}} \left(\frac{a}{R_a} \right)^{-3/2} \left[1 + \frac{8a}{\mathcal{M}_\infty^2 R_a} \right]^{1/2}. \tag{38}$$

Because $\tau_{\text{stop,HL}} \propto \rho_\infty^{-1}$, the inspiral timescales are inversely proportional to the ambient density. If the density of the medium is increased, then the binary evolves more quickly.

A less-intuitive feature of the two inspiral timescales is the leading-order dependence on $a^{-3/2}$. This dependence arises from the fact that the accretion radius of each particle is inversely proportional to the square of its speed relative to the gas. As the binary separation decreases, the orbital speed of each object increases, so the BHL force decreases with decreasing a. The lengthening of $\tau_{\text{insp,BH}}$ with decreasing a, for fixed ρ_∞, implies that the binary will never merge.

A natural question to ask is whether the stopping time is longer than the inspiral timescale for a given binary. In the BH regime, the ratio of the timescales is

$$\frac{\tau_{\text{insp,BH}}}{\tau_{\text{stop,BH}}} = \frac{1}{8\sqrt{2}} \left(\frac{\mathcal{M}_\infty^2}{1+\mathcal{M}_\infty^2} \right)^{1/2} \left(\frac{a}{R_a} \right)^{-3/2} \left[1 + \frac{8a}{\mathcal{M}_\infty^2 R_a} \right]^{1/2}. \tag{39}$$

For $\mathcal{M}_\infty = 2$, this implies that $\tau_{\text{stop,BH}} > \tau_{\text{insp,BH}}$ where $a \gtrsim 0.21 R_a$ (this transition would occur at $a = 0.198 R_a$ if the HL timescales are used instead).

5.2. *Numerical Timescales and their Hierarchy*

Having established the analytic predictions for timescales of accretion, stopping, and inspiral, we now proceed to measure these same quantities in our numerical simulations. For our simulated binaries, we measure orbit-averaged timescales of mass accretion,

$$\langle \tau_{\text{accr}} \rangle \equiv \frac{M_0}{\langle \dot{M} \rangle}, \tag{40}$$

slowdown of the CM,

$$\langle \tau_{\text{stop}} \rangle \equiv \frac{E_{\text{trans}}}{\langle \dot{E}_{\text{trans}} \rangle}, \tag{41}$$

and orbital inspiral

$$\langle \tau_{\text{insp}} \rangle \equiv \frac{a_0}{\langle \dot{a} \rangle}, \tag{42}$$

by taking the median over an integer number of orbits from $t = 30 R_a/v_\infty$ until the end of each simulation ($t = 50 R_a/v_\infty$).
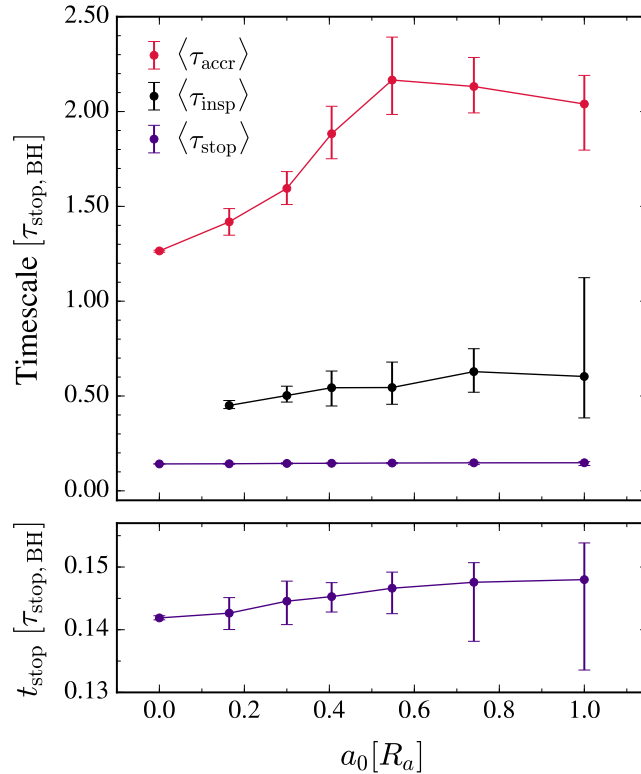
Figure 11. Orbit-averaged timescales versus initial semi-major axis, a_0, calculated according to equations (40), (41), and (42). The error bars show the 15.87th to 87.13th percentile range of instantaneous timescales, where the majority of this modulation occurs periodically, with varying binary orbital phase (see Figures 5, 9, and 10). All values are normalized to the BH stopping time, given by equation (13). Unlike the prediction of BHL, we find that for all of the simulated binaries, the CM motion slows faster than the orbit decays. The difference between $\langle \tau_{\text{accr}} \rangle$ and $\langle \tau_{\text{stop}} \rangle$ for the $a_0 = 0.0R_a$ simulation (single particle) indicates the difference in efficiency between accretion and drag on the CM. The shape of $\langle \tau_{\text{accr}} \rangle$ with increasing a_0, though, shows the truncation of the accretion rate as the binary separation grows.

For $a_0 = 0.0R_a$, the median and percentile ranges of $\langle \tau_{\text{accr}} \rangle$ and $\langle \tau_{\text{stop}} \rangle$ are computed over $30 \leq t \leq 50 R_a/v_\infty$.

Numerically-derived orbit averaged timescales are shown in Figure 11. The difference in $\langle \tau_{\text{accr}} \rangle$ and $\langle \tau_{\text{stop}} \rangle$ at $a_0 = 0.0R_a$ conveys the difference in efficiency of accretion and drag. The fact that $\langle \tau_{\text{stop}} \rangle \ll \langle \tau_{\text{accr}} \rangle$ implies that drag coefficients, compared to the BH predictions, are generally larger than unity, while accretion coefficients are of order unity or lower. This hierarchy of timescales has been consistently observed in previous simulations (e.g. Blondin & Raymer 2012; Thun et al. 2016) and arises from large-scale gravitational interactions contributing to the DF drag (Ostriker 1999), while accretion is a local property.

As we introduce binaries of increasing separation, the timescales change, but their basic hierarchy stays the same. The lengthening accretion timescale with larger binary separation arises from a drop in $\langle \dot{M} \rangle$ with larger a_0, as shown in Figure 8. We also see that $\langle \tau_{\text{stop}} \rangle$ changes by only 5% as the binary separation increases. This reflects the fact that the slow-down of the CM is dominated by the DF force due

to the downstream wake. The wider binaries show larger time-variability since the primary shock changes shape as the particles move in and out of each other's wake (see Figure 1), but the overall structure downstream from the binary is similar in each simulation. Critically, the overall size of the wake and the standoff distance of the primary shock is similar in all simulations, implying the Coulomb logarithm, $\ln(r_{\text{max}}/r_{\text{min}})$ in the DF force is essentially unchanged (Ostriker 1999; Thun et al. 2016, Section 5.3).

Figure 11 shows that the timescales fall into a clear hierarchy with $\langle \tau_{\text{accr}} \rangle > \langle \tau_{\text{insp}} \rangle > \langle \tau_{\text{stop}} \rangle$. The most striking aspect of this hierarchy is that $\langle \tau_{\text{insp}} \rangle > \langle \tau_{\text{stop}} \rangle$ for all of the binary systems we simulated. In Section 5.1, we found that a simple application of BHL predicts that $\langle \tau_{\text{stop}} \rangle$ should be longer than $\langle \tau_{\text{insp}} \rangle$ for all binaries with $a_0 \geq 0.21R_a$. Instead, the stopping time is always shorter, which means that the CM motion will come to a stop before the orbit decays.

Another prediction of the BHL formalism is the shape of $\langle \tau_{\text{insp}} \rangle$ as a function of a_0. We plot $\tau_{\text{insp,BH}}$ versus a_0 in Figure 12 (dashed line). The plot reveals the $a^{-3/2}$ leading order

shape of $\tau_{\mathrm{insp,BH}}$. We include in Figure 12 the calculated values of $\langle\tau_{\mathrm{insp}}\rangle$ of Figure 11. Instead of following $a^{-3/2}$, $\langle\tau_{\mathrm{insp}}\rangle$ *decreases* with decreasing a_0.

To obtain the a_0-dependence of $\langle\tau_{\mathrm{insp}}\rangle$, we perform a least-squares fit to a power law of the form

$$f(a_0) = A(a_0/R_a)^B. \tag{43}$$

We fit to the median values (the black points in Figure 12) and use one standard deviation (approximately the average of the upper and lower error bars) as the uncertainty on each point when performing the fit. We find $A = 0.46 \pm 0.01$ and $B = 0.19 \pm 0.01$, giving the functional form

$$\tau_{\mathrm{insp,fit}} = 0.46(a_0/R_a)^{0.19}\tau_{\mathrm{stop,BH}}. \tag{44}$$

This fit is shown in Figure 12.

5.3. *Physical Interpretation of* $\langle\tau_{\mathrm{insp}}\rangle$

The sharp difference in scaling between $\langle\tau_{\mathrm{insp}}\rangle \propto a_0^{0.19\pm0.01}$, computed from the hydrodynamic simulations, and $\tau_{\mathrm{insp,BH}} \propto a^{-3/2}$, from BHL theory is apparent in Figure 12. While BHL theory predicts that the binary will take an infinite time to merge, $\tau_{\mathrm{insp,fit}}$ grows shorter as the orbit decays.

By assuming a background density of ρ_∞, $\tau_{\mathrm{insp,BH}}$ fails to capture the enhancement of the local density due to the gravitational pull of the binary CM. If the CM of the binary were at rest relative to the gas, we would expect the density as a function of distance from the CM to be similar to a Bondi profile (Bondi 1952, albeit truncated inside the orbit of the binary since the potential is smoothed to a distance of approximately $a/2$). We use a Bondi density profile to express the density of the gas at a distance of $a/2$ from the CM of the binary:

$$\tilde{\rho} \equiv \frac{\mathcal{M}_\infty^3 \rho_\infty}{8}\left(\frac{R_a}{a}\right)^{3/2} \tag{45}$$

(for $\gamma = 5/3$ and $a/2 \le R_B$; Shapiro & Teukolsky 1983). Replacing ρ_∞ with $\tilde{\rho}$ in equation (38) cancels the leading $a^{-3/2}$ dependence of $\tau_{\mathrm{insp,BH}}$. The modified timescale is then

$$\widetilde{\tau}_{\mathrm{insp,BH}} = \frac{\eta}{2\sqrt{2}\pi}\frac{v_\infty}{G\mathcal{M}_\infty^3 \rho_\infty R_a}\left[1 + \frac{8a}{\mathcal{M}_\infty^2 R_a}\right]^{1/2} \tag{46}$$

where the coefficient η is an overall normalization factor. We choose the normalization such that $\widetilde{\tau}_{\mathrm{insp,BH}} = \langle\tau_{\mathrm{insp}}\rangle$ at $a_0 = 0.16R_a$, which yields $\eta = 4.96$.

We plot $\widetilde{\tau}_{\mathrm{insp,BH}}(\eta = 4.96)$ in Figure 12. With this normalization, $\widetilde{\tau}_{\mathrm{insp,BH}}$ nearly replicates the power law fit and the numerical data. The normalization factor of $\eta \approx 5$ indicates that equation (45) overestimates the density by a factor of approximately 5. This may be because the softening of the potential to the size of the orbit as well as the pressure support provided by the orbital motion of the binary both work to

reduce the local density that can be realized versus the pure Bondi case. In addition, the incoming wind sweeps material from the region of the binary, constantly modifying the density structure of the local region.

5.4. *Comparison to Previous Work*

In previous analytical and semi-analytical work, there has been considerable disagreement of how the inspiral timescale and forces scale with binary separation. Here we briefly discuss these results in light of our semi-analytical interpretation of the inspiral timescale of Section 5.3, noting the different physical scenarios and assumptions that lead previous authors to varying results.

The gaseous DF force acting on a point mass in straight-line motion relative to a background gas was first calculated analytically by Ostriker (1999). As in the case of a collisionless gas, the integral nature of the DF force gives rise to a Coulomb logarithm $\ln(r_{\mathrm{max}}/r_{\mathrm{min}})$. The radii r_{max} and r_{min} represent the range of size scales spanned by the asymmetric wake trailing the point mass. Kim & Kim (2007) applied the methods of Ostriker (1999) to a perturber moving in a circular orbit relative to an initially-uniform gas, and found that the orbital motion truncates the maximum coherence length of the wake to $r_{\mathrm{max}} \approx a$.

Kim et al. (2008) extended these calculations to a symmetric binary pair of perturbers in a circular orbit. Kim & Kim (2007); Kim et al. (2008) report their results with piecewise functions of Mach number, which can be computed from the comparison of orbital velocity at a given separation to the background medium's sound speed. We find that in the regime of relevance to our calculations, equation 14 of Kim & Kim (2007) and equation 5 of Kim et al. (2008) have approximate scaling of $F_{\mathrm{DF}} \cdot \hat{v}_{\mathrm{orb}} \propto a^{1.3}$ for the projection of the DF force along the orbital motion. This implies $\tau_{\mathrm{insp}} \propto a^{-1.8}$ for a uniform medium, a very similar scaling to $\tau_{\mathrm{insp,BH}} \propto a^{-1.5}$.

Stahler (2010) also considered angular momentum loss by a binary embedded in a uniform gas in the linear regime, but came to a very different conclusion. Stahler (2010) computed the angular momentum and energy carried by waves induced by the time-varying quadrupole moment of the binary potential, and reported a scaling with opposite sign from Kim & Kim (2007); Kim et al. (2008) and $\tau_{\mathrm{insp,BH}}$, with $\tau_{\mathrm{insp}} \propto a$ (their equation 56). Sánchez-Salcedo & Chametla (2014) report on this discrepancy, and demonstrate that it can be traced to the multipole expansion that underlies Stahler (2010)'s solution.

Sánchez-Salcedo & Chametla (2014) also perform a calculation of torques on a binary with moving CM, with a semi-analytical approach but under otherwise similar approximations to Kim & Kim (2007); Kim et al. (2008). Their results are therefore most applicable to our particular calculation of
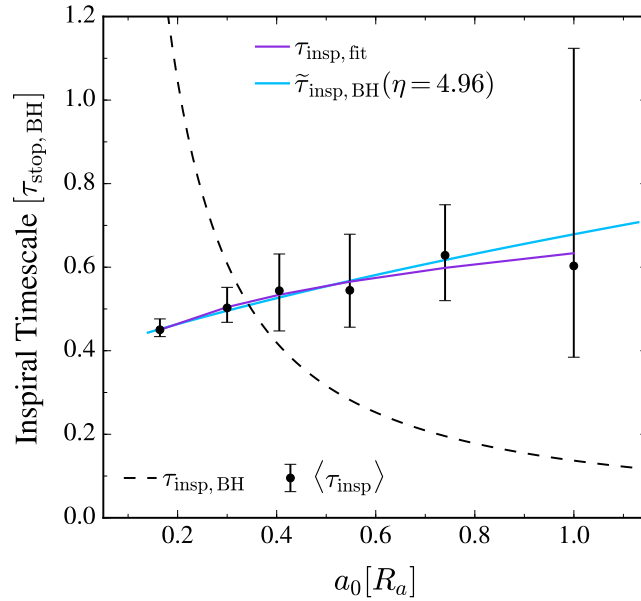
Figure 12. Numerical and analytical inspiral timescales. As in Figure 11, the black points with error bars show $\langle \tau_{insp} \rangle$ for our simulated binaries. A powerlaw fit to the data gives $\tau_{insp,fit} = 0.46(a_0/R_a)^{0.19}$. This increasing inspiral time with a_0 is in stark contrast to the timescale predicted by BHL theory, $\tau_{insp,BH} \propto a^{-3/2}$, which says the binary will never merge. Instead, our simulations show that the inspiral timescale decreases as the binary spirals in. Replacement of ρ_∞ with the Bondi density profile of equation (45) in τ_{insp} gives the modified analytical timescale, $\widetilde{\tau}_{insp,BH}$, given by equation (46). With a normalization factor $\eta = 4.96$, $\widetilde{\tau}_{insp,BH}$ captures our simulated data well, indicating that the positive scaling with a_0 is a result of the density enhancement in the region roughly enclosed by the binary orbit due to the gravitational influence of the CM.

τ_{insp}. Sánchez-Salcedo & Chametla (2014) find identical results to Kim et al. (2008) for the case of a binary with CM at rest. They compute that for a face-on binary at a CM Mach number of 2, the DF torque on the binary orbit has similar scaling to that of Kim et al. (2008), implying $\tau_{insp} \sim \tau_{insp,BH}$, but a normalization lower by a factor of a few, which is similar to our finding of $\eta \sim 5$ in Section 5.3.

Our numerical result exhibits a key difference relative to each of these previous works, which all assume a constant density background. We can improve the analytic representation to bring it into agreement with the numerical findings by considering the enhanced density that arises from flow convergence onto the binary pair. Modifying $\tau_{insp,BH}$ by adopting a local density, $\tilde{\rho} \propto r^{-n}$ (where $n = 1.5$ in the BH case; Section 5.3), changes the scaling of the analytic predictions and can reconcile the results of the analytic models with our simulations, as shown in Figure 12.

6. DISCUSSION

In this section, we discuss some implications of our simulation results for astrophysical binaries.

6.1. *Implications of Timescale Hierarchy and Scaling*

In our models, we focused on the ratio of the initial separation of the binary, a_0, relative to the accretion radius of its center of mass, R_a, as an essential parameter in describing

the flow. This ratio informs the rate of mass accretion and it determines the nature of the drag forces acting on both the orbital and translational motion of the pair. The timescales for accretion, τ_{accr}, orbital inspiral, τ_{insp}, and slow down of the center of mass, τ_{stop} inherit this dependence on a_0/R_a. The timescales follow a hierarchy, with $\tau_{accr} > \tau_{insp} > \tau_{stop}$ for all a_0/R_a that we simulated. In contrast to the expectation from BHL, τ_{insp} is a monotonically increasing function of a_0.

This hierarchy of timescales implies that astrophysical binaries moving through gaseous surroundings will slow relative to the surrounding gas before they either inspiral or accrete significant quantities of gas. Binaries will be slowed when their gravitational cross section has intercepted a gas mass of about 15% the binary mass (because $\tau_{stop} \approx 0.15\tau_{stop,BH}$). To be driven toward merger, they would need to traverse a larger column of approximately 50% their mass, to double in mass, they need to intercept nearly twice their own mass.[1] This suggests that a binary in motion through a uniform, gaseous environment would be slowed such that it

---

[1] We note, however, that the numerically-derived accretion rate (and therefore timescale) is sensitive to the size of the absorbing sink boundary condition, such that smaller objects would be expected to accrete less material (Appendix B). Further, this mass-doubling timescale assumes that the object is able to accrete efficiently from any gas that falls through the sink boundary, without, for example, forming a disk or feeding back substantially into its surroundings.

would enter into a phase of binary-Bondi accretion in which the binary CM was approximately at rest relative to the gas.

The scaling of $\tau_{\rm insp}$ with binary separation is also of great importance. Because this timescale has a positive slope, binaries with shrinking a_0/R_a continue to be driven to merger on finite timescales. The ratio a_0/R_a can shrink either because the binary separation is decreasing, or, as R_a increases when the binary CM motion is slowed. Therefore, whereas the naive scaling $\tau_{\rm insp,BH}$ indicates that pairs of objects can rarely be driven fully to merger by gas – instead being halted at finite separation by the increasing timescale as their orbits shrink – our updated results indicate that a tightening orbit yields a trend toward ever-shorter $\tau_{\rm insp}$.

6.2. *Critical Separation between Gas-Dominated and GW-Dominated Inspiral*

The fact that gaseous forces drive binaries to tighter separations leads to the conclusion that gravitational waves may become important at some separation, especially if the binary is composed of compact objects. For a circular orbit, equal-mass binary, Peters (1964) showed that the inspiral timescale is

$$\tau_{\rm insp,GW} \equiv \frac{a}{\dot{a}_{\rm GW}} = \frac{5a_0^4 c^5}{64 G^3 M^3}, \tag{47}$$

$$= 1.3 \times 10^{18} {\rm yr} \left[\frac{a_0}{\rm AU}\right]^4 \left[\frac{M_\odot}{M}\right]^3. \tag{48}$$

The inspiral timescale that we found numerically, $\tau_{\rm insp,fit}$ given in equation (44), says that $\tau_{\rm insp,gas} \propto a_0^{0.19}$. This mild, positive power law allows the gas to be the dominate driver of orbital inspiral at large separations. At smaller separations, $\tau_{\rm insp,GW} < \tau_{\rm insp,gas}$ and GW radiation dominates the orbital decay until the binary finally merges. Below we find the boundary between gas-dominated and GW-dominated inspiral, by computing the critical separation, $a_{0,\rm crit}$, at which $\tau_{\rm insp,gas} = \tau_{\rm insp,GW}$.

Our expression for $\tau_{\rm insp,fit}$ in equation (44) is given in units of $\tau_{\rm stop,BH}$. To simplify the algebra, let us write our fit in terms of $\tau_{\rm stop,HL}$, instead. Let us define

$$\tau_{\rm insp,gas} = A\left(\frac{a_0}{R_a}\right)^B \frac{v_\infty^3}{4\pi G^2 M \rho_\infty}, \tag{49}$$

where, in these units, $A = 0.71$ instead of 0.46. The power $B = 0.19$ is unchanged. In astrophysical units,

$$\tau_{\rm insp,gas} = 2.9 \times 10^{10} {\rm yr} \left[\frac{a_0}{\rm AU}\right]^{0.19} \left[\frac{v_\infty}{\rm km/s}\right]^{3.38}$$
$$\times \left[\frac{M_\odot}{M}\right]^{1.19} \left[\frac{\rm cm^{-3}}{n_\infty}\right]. \tag{50}$$

Equating $\tau_{\rm insp,gas}$ and $\tau_{\rm insp,GW}$ gives the critical separation

$$a_{0,\rm crit} = 2\left[\frac{A}{5\pi}\frac{G^{1-B}}{c^5}M^{2-B}v_\infty^{2B+3}\rho_\infty^{-1}\right]^{1/(4-B)} \tag{51}$$

with $A = 0.71$ and $B = 0.19$. In astrophysical units,

$$a_{0,\rm crit} = 0.03 {\rm AU}\left[\frac{M}{M_\odot}\right]^{\frac{2-B}{4-B}}\left[\frac{v_\infty}{\rm km/s}\right]^{\frac{2B+3}{4-B}}\left[\frac{\rm cm^{-3}}{n_\infty}\right]^{\frac{1}{4-B}}. \tag{52}$$

In Figure 13, we plot $a_{0,\rm crit}$ versus number density, n_∞, for three sample binary systems (black lines), where we have converted mass density to number density through $\rho_\infty = m_p n_\infty$. The vertical shaded regions give the typical densities encountered in several astrophysical environments. The ISM densities use values from Kim & Ostriker (2017), the AGN conditions use the disk models of Bartos et al. (2017), and the CE density range is modeled after the red giant proposed by Sabach & Soker (2015) to have initiated a CE phase in the hierarchical triple system PSR J0337+1715 . The grey hatched region shows where the enclosed gas mass becomes similar to the binary mass ($M_{\rm encl} > 2M_\odot$). For higher mass binaries, the lower boundary of the hatched region moves up and to the right.

Each black line in the figure plots equation (51) for a different combination of M and v_∞. Above each line, $\tau_{\rm insp,gas}$ is faster than $\tau_{\rm insp,GW}$ and we say that the binary is in the gas-dominated regime. Below each line, $\tau_{\rm insp,GW} < \tau_{\rm insp,gas}$, and the binary is in the GW-dominated regime.

Below, we consider some example systems in the context of Figure 13.

6.3. *Binaries in the ISM*

The multiphase ISM spans a large range of density and temperature conditions. Here, for the sake of a concrete example, we focus on the warm ISM, which occupies about half of the interstellar volume, has a number density of approximately 1 cm^{-3}, and has a temperature of the order of 10^4 K. A binary traveling at 10 km s^{-1} relative to the gas has a Mach number of 1.1. At this speed, a $2M_\odot$ binary with a separation of 1 AU has $\tau_{\rm insp,gas} > \tau_{\rm insp,GW}$. For this system, our numerical fits of $\langle\tau_{\rm insp}\rangle$ and $\langle\tau_{\rm stop}\rangle$ (equations (44) and (C14), respectively) give a stopping timescale of 2×10^{14} yr and an orbital inspiral timescale of 5×10^{13} yr. These timescales indicate that binaries traversing the warm ISM will suffer little dynamical effect from this interaction over the age of the universe.

Nonetheless, this effect might potentially be measurable in the case of pulsar binaries with extremely precise timing. Using $2\dot{P}_{\rm orb}/P_{\rm orb} = 3\dot{a}/a = 3/\tau_{\rm insp}$, the inspiral time gives a period derivative of $\dot{P}_{\rm orb} \approx 10^{-13}$.[2] By comparison, the binary radio pulsar PSR J0751+1807, Nice et al. (2008) found an

---

[2] In this estimate we have neglected the pulsar's influence on its surroundings, which may not be justified because many pulsars are surrounded by hot, low-density wind nebulae. In cases where the standoff distance of the cavity is similar to the binary separation or bow-shock size, drag forces on the binary orbit would likely be substantially reduced.
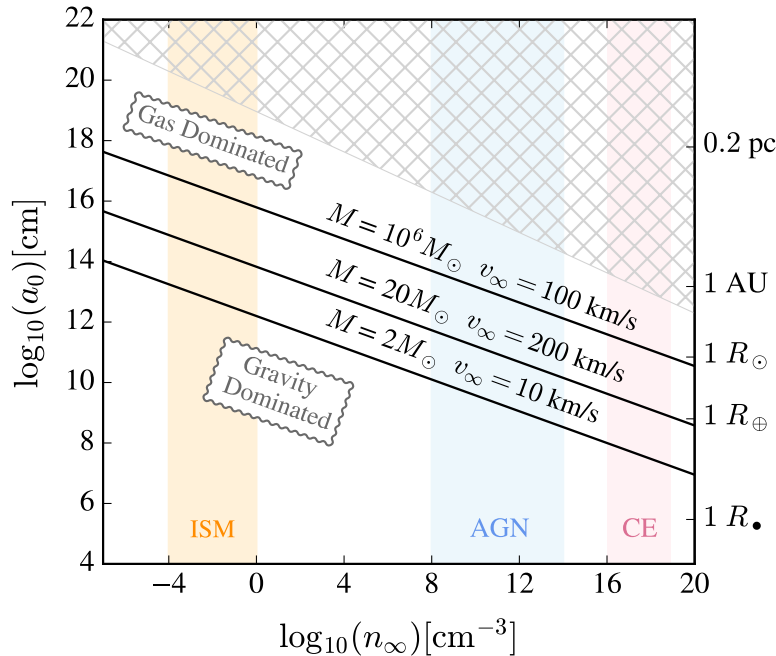
Figure 13. Critical separation between gas-dominated and GW-dominated inspiral as a function of background number density, n_∞. The black curves show $a_{0,\mathrm{crit}}$ (equation (51)) for three combinations of M and v_∞. Above each line, $\tau_{\mathrm{insp,gas}} < \tau_{\mathrm{insp,GW}}$. Below each line, $\tau_{\mathrm{insp,gas}} > \tau_{\mathrm{insp,GW}}$. Vertical shaded regions correspond to the densities found in the Warm/Hot ISM, a model AGN disk, and a red giant envelope (CE). In the grey hatched region, a $2M_\odot$ binary would enclose more than its own mass and, thus, would not remain bound. For higher mass binaries, this "forbidden" region moves up and to the right. See the text for an application of this plot to a few astrophysical systems.

orbital period derivative of $(-3.1 \pm 0.5) \times 10^{-14}$, a precision that is two orders of magnitude better than our sample case presented here.

6.4. *Binaries Interacting with AGN Disks*

The central regions of galaxies hosting AGN experience an inflow of gas that settles into a cold accretion disk surrounding the central SMBH. Stars and binaries coexist with the SMBH and accretion disk in these central regions, forming a dense cluster around the black hole. Dynamical interactions between the stars and disk can trap stars within the disk plane (e.g. Syer et al. 1991; Artymowicz et al. 1993; Ivanov et al. 1998; Šubr & Karas 2005; Miralda-Escudé & Kollmeier 2005; Karas & Šubr 2007; Perets et al. 2007; Baruteau et al. 2011; McKernan et al. 2011, 2012; Just et al. 2012; del Valle & Escala 2014; Kennedy et al. 2016; Panamarev et al. 2018).

Our result that $\tau_{\mathrm{stop}} < \tau_{\mathrm{insp}}$ for all the binaries we simulated demonstrates that trapping by the AGN disk is not reserved for single stars. Instead, the CM motion of a binary can be slowed by the gaseous disk without causing a merger of the binary (we expect this conclusion to hold as long as $a_0 < H$, the scale-height of the disk). That is, binaries formed outside of the disk can remain intact after undergoing capture into the disk plane. When this process involves BBHs, the gaseous drag can aid the trend toward merger until the separation is

reduced sufficiently that gravitational waves take over, as discussed in Section 6.2. These mergers are of additional interest because BBH mergers in dense, gaseous environments may be accompanied by detectable electromagnetic emission (e.g. Farris et al. 2015; Stone et al. 2017; Kelly et al. 2017).

To give a concrete example, we use the disk model of Bartos et al. (2017, their equations 1 - 4) with a central black hole mass of $M_\bullet = 10^6 M_\odot$. The central black hole dominates the gravitational force within a sphere of influence of ≈ 1 pc, so we assume that binaries orbiting the black hole in this region do so in Keplerian orbits with a CM speed of $v_\infty = \sqrt{GM_\bullet / R_{\mathrm{disk}}}$. At $R_{\mathrm{disk}} = 0.1$ pc, $n_\infty = 3 \times 10^{11} \mathrm{cm}^{-3}$, and the Keplerian speed is $v_\infty = 207$ km s^{-1}. This speed gives a CM Mach number of 4.6 (neglecting the effect of rotation of the disk). A $20M_\odot$ BBH with $a_0 = 2$ AU falls in the gas-dominated regime (See Figure 13). If inclined such that it is continuously within the disk plane, we find $\tau_{\mathrm{stop}} = 4 \times 10^4$ yr, $\tau_{\mathrm{insp}} = 2 \times 10^5$ yr, and $\tau_{\mathrm{accr}} = 5 \times 10^5$ yr. This implies that the binary is entrained within the disk flow (and any eccentricity is damped) within approximately 14 orbits, and the BBH inspirals within approximately 70 orbits. Over this time, the BBH might accrete up to 40% its own mass, growing to approximately $30M_\odot$. The brevity of these timescales relative to a typical AGN activity cycle, on the order of 10^6 yr, in-

dicates that under certain conditions AGN disks very likely play a role in tightening BBHs.

6.5. *Embedded Binaries in Common Envelope*

Triple-star systems are common. While about 10% of solar mass stars are in triple or higher-order systems, nearly 60% of O-type stars are in similar hierarchical configurations (e.g. Moe & Di Stefano 2017, Figure 39). For long-term dynamical stability, these systems must be hierarchical (Naoz & Fabrycky 2014). Many such triple systems containing compact objects must have experienced significant mass-transfer events as their stellar progenitors evolved (Tauris & van den Heuvel 2014; Sabach & Soker 2015; Toonen et al. 2016; Di Stefano 2018). In some of these hierarchical triple systems, the outer star evolves to transfer mass toward an inner, more compact binary. Depending on the stability of this mass transfer, the donor star's mass transfer could either proceed at a low rate or lead to runaway orbital tightening and the engulfment of the more compact pair within the envelope of the donor star. What happens when a close binary becomes embedded in a common envelope (CE) has been a topic of previous uncertainty (e.g. Sabach & Soker 2015). In particular, would the binary spiral in within the stellar envelope, or be driven to merger?

Unraveling the outcomes of these triple-star CE encounters requires an understanding of gas accretion and orbital evolution as studied in this paper. If one assumes a simple formalism, such as the timescales derived from BHL, it would appear that a binary embedded in a CE should merge faster than its CM spirals into the donor star's envelope. We have shown here that this is not necessarily the case. Instead, we have found that the slow-down of the binary's CM (which is the driver of the CE inspiral) occurs more quickly than the embedded binary's own separation decays. Therefore, the embedded binary can spiral into the envelope gas and that process alone will not cause the binary to merge.

Since the binary may be able to complete part of the CE inspiral intact, there are many possible outcomes for the interaction. The binary may survive the CE if the envelope can be ejected early in the encounter, the binary may be tidally disrupted before envelope ejection, or, in the case of unsuccessful envelope ejections, one or both of the binary components could merge with the core of the donor star. The revised formalism presented in this paper should be used when examining the various outcomes expected from these complex interactions. For example, Sabach & Soker (2015) considered a formation scenario for PSR J0337+1715 in which the outer binary system remains intact as its CM spirals into the envelope of the donor star, reaching high enough densities to be tidally disrupted. Our results indicate this channel is indeed plausible, as the timescale for the drag-induced inspiral of the CM of the embedded binary is shorter than the

timescale for the embedded binary's finite semi-major axis to decay.

7. CONCLUSIONS

This paper has studied the evolution of binaries moving through gaseous media as a function of the binary system's initial semi-major axis, a_0, relative to its gravitational focusing radius, R_a. We extended the analytical and numerical formalisms of single-particle BHL accretion to the case of a binary system moving perpendicular to the orbital angular momentum vector of the pair. We performed 3D hydrodynamical simulations to study the effects of accretion and drag on the translational and orbital motion of the system. Below we summarize the main conclusions of this work.

1. The introduction of a finite binary separation softens the gravitational potential of the pair relative to a single object, and introduces time-dependent structures into the flow (as described in Section 4.1 and seen in Figures 1, 2, 3, and 4). We find that the ratio of the binary separation to the gravitational focusing scale is crucial in describing the flow structure. When $a/R_{BH} < 1$, the binary orbits within a bow shock that is otherwise similar to that from a single mass. In these cases, the orbital motion is supersonic relative to the post-shock gas and the pair launches spiral shocks into its surroundings (Figure 2). By contrast, when $a/R_{BH} > 1$, the binary members are each trailed by their own shock structure.

2. The orbiting binary's motion introduces periodic variation in the accretion rate onto the binary components (see Section 4.2 and Figure 5). The overall accretion rate onto the binary is again modulated by the ratio of the binary separation to the gravitational focusing scale. When $a/R_{BH} \ll 1$, the accretion rate onto the binary approaches that of a single particle, with scaling $\dot{M} \propto M^2$. When $a/R_{BH} > 1$, the accretion rate approaches the sum of two independent particles with scaling $\dot{M} \propto m_1^2 + m_2^2$ (Figure 8).

3. Gaseous DF and the accretion of momentum give rise to forces that modify the CM and orbital motion of the pair. In Section 4.3, we discuss the projection of these forces onto the CM and orbital velocities. CM deceleration is dominated by DF forces from the large-scale wake that trails the binary (Figure 9). Gas structures and flow on the scale of the binary orbit give rise to forces that drive orbital tightening (e.g., Kim et al. 2008). In this case, momentum accretion and DF become similarly important (Figure 10).

4. We measure orbit-averaged timescales for accretion, $\langle\tau_{accr}\rangle$, slow down of the CM, $\langle\tau_{stop}\rangle$, and orbital inspiral of the binary, $\langle\tau_{insp}\rangle$, equations (40), (41), and

(42), respectively. For all values of a_0 that we simulated, the timescales exhibit a clear hierarchy with $\tau_{\rm stop} < \tau_{\rm insp} < \tau_{\rm accr}$ (Figure 11). Therefore, a binary moving through a gaseous medium slows before being driven to merger or gaining significant mass (Section 5).

5. BHL theory predicts that $\tau_{\rm insp} \propto a_0^{-3/2}$, which implies that as the orbit tightens the time to coalescence lengthens. By contrast, in our simulations we find a mild, positive scaling, $\langle \tau_{\rm insp} \rangle \propto a^{0.19}$ (given by equation (44) and shown in Figure 12). Previous semi-analytic work predicting the sign and scaling of this relation has arrived at a variety of conclusions, as described in Section 5.4. We show that the simulation results can be reproduced by considering the enhanced density in which the binary orbits due to the convergence of gravitationally-focused gas (equation (46)), a key effect that was neglected in previous analytic studies.

6. The magnitude of the forces we derive implies that binaries in environments from the ISM to star-forming clouds, AGN disks, and stellar envelopes during CE phases all may experience transformation due to interaction with their gaseous surroundings. We discuss particular systems, the implications of the observed hierarchy of timescales, and derive the transition between systems whose orbital evolution is dominated by gaseous interaction (at large separations) and those whose orbital evolution is driven by gravitational radiation (at small separations) in Section 6.

There are many aspects of this problem left to explore. In this work, we have simulated equal-mass binary systems in circular orbits inclined such that the incoming wind hits the orbital plane edge-on. To extend the formalism of BHL, we modeled the idealized case of a uniform-density background gas. Realistic binary systems are often subject to nonuniform gases with gradients in density, pressure, and Mach number. Previous work has shown that breaking the symmetry of canonical BHL has significant impacts on the flow. For example, MacLeod & Ramirez-Ruiz (2015); MacLeod et al. (2017) found that in single-object BHL, the presence of density gradients typical of CE encounters impart net rotation and reduce accretion from post-shock flow. Krumholz et al. (2006) simulated BHL flows in cold, turbulent media of relevance to star-forming clouds and found that the vorticity imparted by turbulence can dominate the flow structure and lead to highly variable accretion rates. Future simulation work could relax our current assumptions of equal mass, circular orbits, edge-on inclination, and a homogeneous background medium to extend the applicability of these results to a broader range of astrophysical systems and environments.

Software: FLASH (Fryxell et al. 2000); yt (Turk et al. 2011); astropy (Astropy Collaboration et al. 2013).

APPENDIX

A. DERIVATION OF ANALYTICAL TIMESCALES FOR ORBITAL INSPIRAL

A principle objective of this paper is to learn how the predictions of BHL must be modified to describe a binary system. In this section, we derive the analytic timescales for orbital inspiral given by equations (38) and (37).

To associate a timescale with the decay of the orbit, we imagine the CM at rest and calculate the Bondi-Hoyle energy dissipation rate for m_1 and m_2 as they orbit the CM. For an equal-mass binary in a circular orbit, $m_1 = m_2 = M/2$, and the orbital speed is $v_{\rm orb}^2 = GM/a$. If V_1 and V_2 are the barycentric speeds of m_1 and m_2, respectively, then $V_1 = V_2 = v_{\rm orb}/2$. The BH accretion radius, equation (10), of m_1 is

$$R_{\rm BH,1} = \frac{2Gm_1}{V_1^2 + c_{s,\infty}^2} \tag{A1}$$

with an energy dissipation rate, equation (12), of

$$\dot{E}_{\rm BH,1} = \frac{1}{2}\pi R_{\rm BH,1}^2 \rho_\infty (V_1^2 + c_{s,\infty}^2)^{3/2}. \tag{A2}$$

The total energy dissipation rate for m_1 and m_2 is just twice $\dot{E}_{\mathrm{BH},1}$, that is,

$$\dot{E}_{\mathrm{BH,orb}} = \frac{4\pi G^2 m_1^2 \rho_\infty}{(V_1^2 + c_{s,\infty}^2)^{1/2}}. \tag{A3}$$

Replacing $m_1 = M/2$, $V_1 = v_{\mathrm{orb}}/2$, and factoring out a 1/4 from the denominator gives

$$\dot{E}_{\mathrm{BH,orb}} = \frac{2\pi G^2 M^2 \rho_\infty}{(v_{\mathrm{orb}}^2 + 4c_{s,\infty}^2)^{1/2}}. \tag{A4}$$

The total orbital energy of the binary is $E_{\mathrm{orb}} = -Gm_1 m_2/2a = -GM^2/8a$, so the timescale for orbital decay is

$$\tau_{\mathrm{insp,BH}} \equiv \frac{|E_{\mathrm{orb}}|}{\dot{E}_{\mathrm{BH,orb}}} = \frac{GM^2/8a}{2\pi G^2 M^2 \rho_\infty (v_{\mathrm{orb}}^2 + 4c_{s,\infty}^2)^{-1/2}} = \frac{(v_{\mathrm{orb}}^2 + 4c_{s,\infty}^2)^{1/2}}{16\pi G \rho_\infty a}. \tag{A5}$$

If we factor v_{orb}^2 out of the parenthesis and substitute $v_{\mathrm{orb}} = (GM/a)^{1/2}$ then

$$\tau_{\mathrm{insp,BH}} = \frac{1}{16\pi G \rho_\infty a}\left(\frac{GM}{a}\right)^{1/2}\left[1 + 4a\frac{c_{s,\infty}^2}{GM}\right]^{1/2} = \frac{1}{16\pi \rho_\infty a^{3/2}}\left(\frac{M}{G}\right)^{1/2}\left[1 + 4a\frac{c_{s,\infty}^2}{GM}\right]^{1/2}. \tag{A6}$$

Now, the term $c_{s,\infty}^2/GM$ can be expressed as

$$\frac{c_{s,\infty}^2}{GM} = \frac{2c_{s,\infty}^2}{v_\infty^2}\frac{v_\infty^2}{2GM} = \frac{2}{\mathcal{M}_\infty^2 R_a}, \tag{A7}$$

so we can write

$$\tau_{\mathrm{insp,BH}} = \frac{1}{16\pi}\left(\frac{M}{G}\right)^{1/2}\rho_\infty^{-1} a^{-3/2}\left[1 + \frac{8a}{\mathcal{M}_\infty^2 R_a}\right]^{1/2}. \tag{A8}$$

It is convenient to introduce a factor of R_a in order to obtain the quantity (a/R_a), giving

$$\tau_{\mathrm{insp,BH}} = \frac{1}{8\sqrt{2}}\left[\frac{v_\infty^3}{4\pi G^2 M \rho_\infty}\right]\left(\frac{a}{R_a}\right)^{-3/2}\left[1 + \frac{8a}{\mathcal{M}_\infty^2 R_a}\right]^{1/2}. \tag{A9}$$

The first term in brackets is simply $\tau_{\mathrm{stop,HL}}$, so we have arrived at equation (38):

$$\tau_{\mathrm{insp,BH}} = \frac{\tau_{\mathrm{stop,HL}}}{8\sqrt{2}}\left(\frac{a}{R_a}\right)^{-3/2}\left[1 + \frac{8a}{\mathcal{M}_\infty^2 R_a}\right]^{1/2}. \tag{A10}$$

In the Hoyle-Lyttleton formalism, the sound speed is omitted from the characteristic velocity in the expressions (A1) and (A2), resulting in a total orbital energy dissipation rate of $\dot{E}_{\mathrm{HL,orb}} = 2\pi G^2 M^2 \rho_\infty v_{\mathrm{orb}}^{-1}$ and a decay timescale of

$$\tau_{\mathrm{insp,HL}} = \frac{\tau_{\mathrm{stop,HL}}}{8\sqrt{2}}\left(\frac{a}{R_a}\right)^{-3/2}, \tag{A11}$$

which is equation (37). This quantity is the leading coefficient of $\tau_{\mathrm{insp,BH}}$. That is,

$$\tau_{\mathrm{insp,BH}} = \tau_{\mathrm{insp,HL}}\left[1 + \frac{8a}{\mathcal{M}_\infty^2 R_a}\right]^{1/2}. \tag{A12}$$

B. VALIDATION OF NUMERICAL METHOD

In this section, we characterize the sensitivity of our results to background density, ρ_∞, the length of the computational domain in each Cartesian direction, L, the radius of the absorbing sinks used to represent the binary, R_s, and the length of each side of the finest grid cells, δ_{min}. The studies presented in this section adopt $\mathcal{M}_\infty = 2$, $\gamma = 5/3$, and $a_0 = 1.0 R_a$. In the panels of Figure 14, we plot $\langle \tau_{\mathrm{accr}} \rangle$, $\langle \tau_{\mathrm{insp}} \rangle$, and $\langle \tau_{\mathrm{stop}} \rangle$, normalized to $\tau_{\mathrm{insp,BH}}$, for each series of studies.

B.1. *Grid Refinement*

We maximally refine the region of our two sink particles, so that sink cells have length of $\delta_{\min}$ in each Cartesian direction. We test sensitivity to $\delta_{\min}$ by running simulations with $\delta_{\min}/R_{\rm s} = 3$ and 6 with sink sizes of $R_{\rm s} = 0.05R_{\rm a}$ and $R_{\rm s} = 0.1R_{\rm a}$. Comparing points with the same $R_{\rm s}$ in panel C of Figure 14 reveals that there is very little difference in the orbit-average timescales when the resolution is doubled from our fiducial value of $\delta_{\min}/R_{\rm s} = 3$. When $R_{\rm s} = 0.05R_{\rm a}$, $\langle\tau_{\rm stop}\rangle$ and $\langle\tau_{\rm accr}\rangle$ change by less than 1% and $\langle\tau_{\rm insp}\rangle$ increases by 2.5%. Accretion rates are larger when $R_{\rm s} = 0.1R_{\rm a}$ and, in this case, we find that a resolution of twice our fiducial value increases $\langle\tau_{\rm accr}\rangle$ by 2.6% and the other timescales change by less than 1%. We adopt $\delta_{\min}/R_{\rm s} = 3$ in our production runs.

B.2. *Sink Radius*

The influence of sink radius, $R_{\rm s}$, on accretion rates in single-object BHL flows has been well-studied (e.g. Ruffert & Arnett 1994; Blondin & Raymer 2012; MacLeod & Ramirez-Ruiz 2015; MacLeod et al. 2017). For example, Ruffert & Arnett (1994) found that doubling the size of the sink increased accretion rates by $\approx 15-25\%$ in their simulations with $\mathcal{M}_\infty = 3$ and $\gamma = 5/3$. We test $R_{\rm s}$ in our setup by running simulations with half and twice our fiducial value of $R_s = 0.05R_{\rm a}$. These simulations adopt $\delta_{\min}/R_{\rm s} = 3$, $\rho_\infty = 10$ and $L = 32R_a$. When $R_{\rm s}/R_{\rm a}$ is doubled from 0.05 to 0.1, $\langle\tau_{\rm stop}\rangle$ decreases by 1% and $\langle\tau_{\rm insp}\rangle$ and $\langle\tau_{\rm accr}\rangle$ each decrease by 25%. A doubling of $R_{\rm s}/R_{\rm a}$ from 0.025 to 0.05 similarly decreases $\langle\tau_{\rm stop}\rangle$ by 1%, while $\langle\tau_{\rm insp}\rangle$ decreases by 17% and $\langle\tau_{\rm accr}\rangle$ decreases by 27%.

The filled points in panel C of Figure 14 show that the hierarchy of timescales $\langle\tau_{\rm accr}\rangle \geq \langle\tau_{\rm insp}\rangle \geq \langle\tau_{\rm stop}\rangle$ is preserved across values of $R_{\rm s}$. However, because sink size influences rates of mass accretion, the accretion timescale is sensitive to this choice. For an astrophysical accretor of size less than $R_{\rm s}$, the mass accretion rate we derive therefore represents the upper limit defined by the flux of material into the object's vicinity, rather than the precise amount that is able to accrete. Because sink size affects the momentum accreted, we note that the exact scaling of $\tau_{\rm insp,fit}$ as a function of a_0 will be influenced by choice of sink radius. We adopt $R_{\rm s} = 0.05R_{\rm a}$ in our production runs.

B.3. *Background Density*

We performed tests of background density, ρ_∞, to ensure that the timescales we derive could be scaled to any astrophysical density. We ran simulations with $\rho_\infty = 10$, 100, and 1000. These simulations were run with $R_{\rm s} = 0.05R_{\rm a}$, $L = 16R_{\rm a}$, and $R_s/\delta_{\min} = 6$. Panel A of Figure 14, shows that the background density scales out of the orbit-average timescales so that the values are the same when normalized to $\tau_{\rm stop,BH}$. In all cases $\langle\tau_{\rm accr}\rangle \gg \langle\tau_{\rm insp}\rangle \gg \langle\tau_{\rm stop}\rangle$. Increasing our fiducial value by a factor of 100 (to $\rho_\infty = 1000$) only changes $\langle\tau_{\rm accr}\rangle/\tau_{\rm stop,BH}$ and $\langle\tau_{\rm insp}\rangle/\tau_{\rm stop,BH}$ by 7.6% each, and decreases $\langle\tau_{\rm stop}\rangle/\tau_{\rm stop,BH}$ by 4%. We adopt $\rho_\infty = 10$ for our production runs.

B.4. *Extent of the Computational Domain*

The DF drag forces exerted on an object depend on the size of the wake, with approximate scaling dictated by a Coulomb logarithm $\ln(r_{\max}/r_{\min})$, where $r_{\min}$ is the size scale outside of which a net force is contributed and $r_{\max}$ is the system size (Ostriker 1999). While we are forced to choose a single system size in our numerical simulations, we measure the approximate scaling here.

In our setup, the CM of the binary is located at the origin and we place all outer boundaries at a distance $L/2$ from the origin. We run simulations with half and double a fiducial value of $L = 16R_{\rm a}$. Panel B of Figure 14 shows that $\langle\tau_{\rm accr}\rangle$ and $\langle\tau_{\rm insp}\rangle$ do not vary significantly at changing L. Doubling L from 16 to 32 reduces $\langle\tau_{\rm accr}\rangle$ by 6.4% and reduces $\langle\tau_{\rm insp}\rangle$ by 2.6%.

On the other hand, the same doubling of L reduces $\langle\tau_{\rm stop}\rangle$ by 43%, which is expected because this timescale is dominated by DF due to gas at larger scales. In otherwise similar simulations of single-object BHL, Thun et al. (2016); MacLeod et al. (2017) found $r_{\min} \approx 0.5R_{\rm a}$ and $r_{\max} \approx L/2$. A fit of the DF force for the simulations presented here reveals that $r_{\min} \sim 3R_{\rm a}$ for the larger box sizes of $L = 16R_{\rm a}$ and $L = 32R_{\rm a}$ (adopting $r_{\max} \approx L/2$). Since $\tau_{\rm stop} \propto 1/F_{\rm DF,CM}$, our measured stopping time can be approximately scaled to larger astrophysical systems by dividing by $\ln[(L/2)/(3R_{\rm a})]$.

C. FITTING FORMULAE TO SIMULATION RESULTS

In this section, we provide formulae for $\langle\tau_{\rm stop}\rangle$, $\langle\tau_{\rm accr}\rangle$, and $\langle\dot{M}\rangle$ as a function of a_0. The fit for $\langle\tau_{\rm insp}\rangle$ was given in Section 5.2. The remaining quantities, $\langle\tau_{\rm stop}\rangle$, $\langle\tau_{\rm accr}\rangle$, and $\langle\dot{M}\rangle$ do not follow a single power law, so we fit piecewise functions for $a_0 \leq 0.55$ and $a_0 > 0.55$ of the functional form

$$f(a_0) = \begin{cases} A(a_0/R_{\rm a}) + B & a_0 \leq 0.55R_{\rm a} \\[2mm] A(0.55) + B & a_0 > 0.55R_{\rm a} \end{cases} \tag{C13}$$

(A)   (B)   (C)
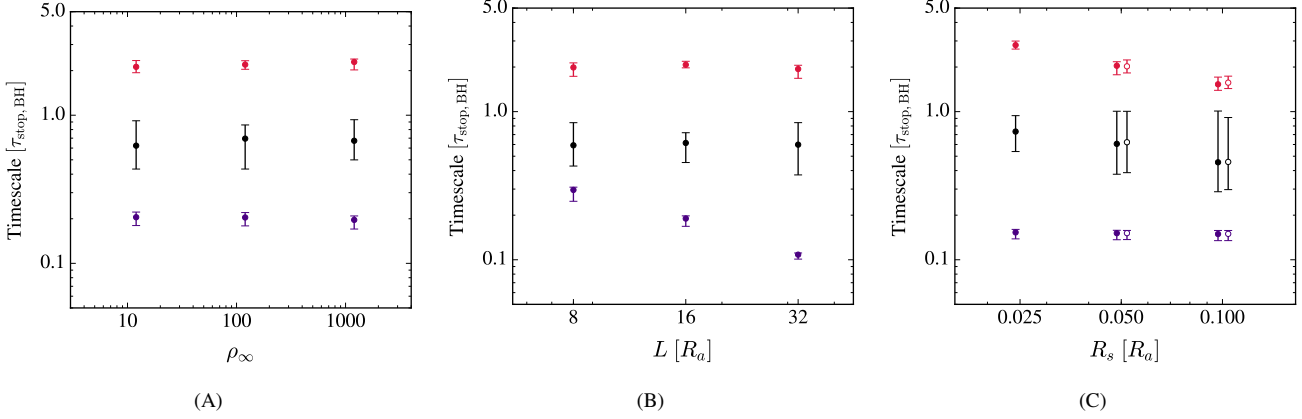
Figure 14. Orbit-averaged timescales calculated from each of our numerical tests. All of these tests were performed with $a_0 = 1.0R_a$ and $\gamma = 5/3$. In each panel, $\langle\tau_{accr}\rangle$ is plotted in red, $\langle\tau_{insp}\rangle$ in black, and $\langle\tau_{stop}\rangle$ in purple. The y axis is in units of $\tau_{stop,BH}$ and the x axis shows the parameter under study. Each point gives the median over the simulation times used in the average while the lower and upper error bars give the 15.87th to 87.13th spread about the median. **Panel A** shows the results of our studies of background density, in which we ran simulations with, $\rho_\infty = 10, 100$, and 1000. All three timescales show excellent convergence. **Panel B** shows our tests of the size of the computational domain. Here L is the width of the domain in the x, y, and z directions, giving a computational volume of L^3. **Panel C** plays a dual role, showing tests of sink size, R_s, and finest grid resolution, δ_{min}. The filled circles show our tests of $R_s = 0.025, 0.05$, and $0.1R_a$ with $R_s/\delta_{min} = 3$ cells across the sink radius. The open circle plots (offset slightly to the right for clarity) show simulations with $R_s = 0.05$ and $1.0R_a$, but at higher resolution ($R_s/\delta_{min} = 6$ cells across the sink radius).

Table 2. Orbit-averaged simulation data.

a_0	$\langle\tau_{insp}\rangle$	$\langle\tau_{stop}\rangle$	$\langle\tau_{accr}\rangle$	$\langle\dot{M}\rangle$
$[R_a]$	$[\tau_{stop,BH}]$	$[\tau_{stop,BH}]$	$[\tau_{stop,BH}]$	$[\dot{M}_{BH}]$
0.0	—	$0.142^{+0.000}_{-0.000}$	$1.265^{+0.004}_{-0.007}$	$0.988^{+0.007}_{-0.002}$
0.16	$0.450^{+0.026}_{-0.016}$	$0.143^{+0.002}_{-0.003}$	$1.418^{+0.070}_{-0.070}$	$0.883^{+0.008}_{-0.006}$
0.3	$0.503^{+0.049}_{-0.035}$	$0.145^{+0.003}_{-0.004}$	$1.595^{+0.089}_{-0.085}$	$0.786^{+0.022}_{-0.026}$
0.41	$0.544^{+0.088}_{-0.096}$	$0.145^{+0.002}_{-0.002}$	$1.883^{+0.145}_{-0.132}$	$0.663^{+0.043}_{-0.036}$
0.55	$0.545^{+0.134}_{-0.088}$	$0.147^{+0.003}_{-0.004}$	$2.166^{+0.226}_{-0.181}$	$0.579^{+0.041}_{-0.049}$
0.74	$0.628^{+0.121}_{-0.109}$	$0.148^{+0.003}_{-0.009}$	$2.132^{+0.153}_{-0.139}$	$0.588^{+0.029}_{-0.035}$
1.0	$0.603^{+0.521}_{-0.219}$	$0.148^{+0.006}_{-0.014}$	$2.040^{+0.151}_{-0.243}$	$0.613^{+0.079}_{-0.041}$

NOTE—Here we give median values of the orbit-averaged timescales and accretion rates for our simulated binaries. The subscripts and superscripts give the 15.87th to 87.13th percentile spread, respectively, about the median. The timescales are given in units of $\tau_{stop,BH}$. The accretion rates are in units of $\dot{M}_{BH}$.

which goes to a constant value because the two particles become independent as $a_0 \to \infty$. We perform least-squares fits of the median values given in Table 2 to the model, $f(a_0)$, weighting the points according to one standard deviation of their time variability. For $\langle\tau_{stop}\rangle$, we find $A = 0.009$ and $B = 0.142$, giving

$$\frac{\tau_{stop,fit}}{\tau_{stop,BH}} = \begin{cases} 0.009(a_0/R_a) + 0.142 & a_0 \leq 0.55R_a \\ \\ 0.147 & a_0 > 0.55R_a \end{cases} \tag{C14}$$
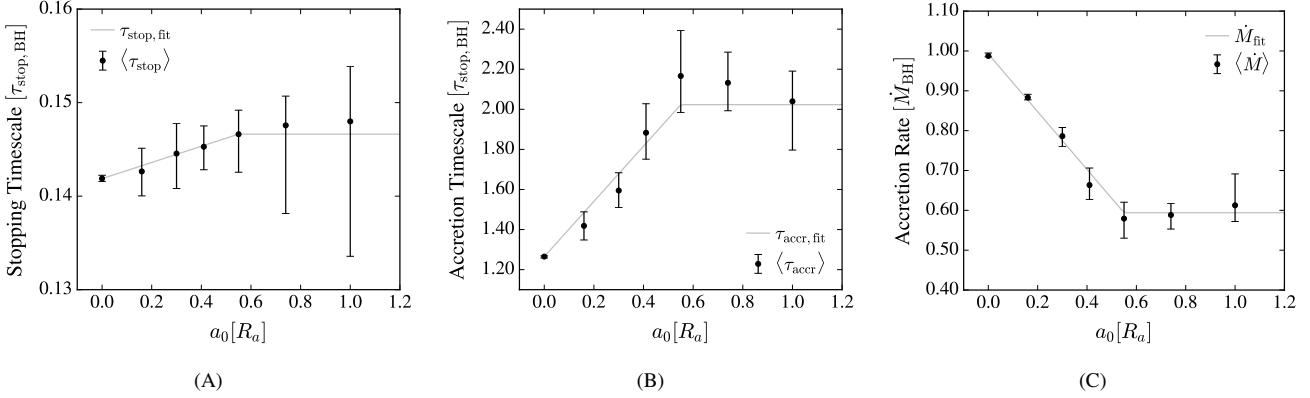
Figure 15. Piecewise fits of $\langle \tau_{\text{stop}} \rangle$, $\langle \tau_{\text{accr}} \rangle$, and $\langle \dot{M} \rangle$ (panels A, B, and C, respectively). In each panel, the black points and error bars correspond to the data of Table 2 and the grey line shows the fit, which are given by equations (C14), (C15), and (C16), respectively.

in units of $\tau_{\text{stop,BH}}$. For $\langle \tau_{\text{accr}} \rangle$, we obtain $A = 1.379$ and $B = 1.265$, or

$$\frac{\tau_{\text{accr,fit}}}{\tau_{\text{stop,BH}}} = \begin{cases} 1.379(a_0/R_\text{a}) + 1.265 & a_0 \le 0.55 R_\text{a} \\ \\ 2.023 & a_0 > 0.55 R_\text{a} \end{cases} \tag{C15}$$

in units of $\tau_{\text{stop,BH}}$. For the accretion rate, $\langle \dot{M} \rangle$, in units of $\dot{M}_{\text{BH}}$, we find $A = -0.724$ and $B = 0.992$, that is

$$\frac{\dot{M}_{\text{fit}}}{\dot{M}_{\text{BH}}} = \begin{cases} -0.724(a_0/R_\text{a}) + 0.992 & a_0 \le 0.55 R_\text{a} \\ \\ 0.594 & a_0 > 0.55 R_\text{a}. \end{cases} \tag{C16}$$

In panels (A), (B), and (C) of Figure 15, we plot $\langle \tau_{\text{stop}} \rangle$, $\langle \tau_{\text{accr}} \rangle$, and $\langle \dot{M} \rangle$, respectively, with points and error bars. The associated fit of each quantity is shown with a grey line in each panel.

REFERENCES

Abbate, F., Possenti, A., Ridolfi, A., et al. 2018, MNRAS, 481, 627, doi: 10.1093/mnras/sty2298

Artymowicz, P., Lin, D. N. C., & Wampler, E. J. 1993, ApJ, 409, 592, doi: 10.1086/172690

Astropy Collaboration, Robitaille, T. P., Tollerud, E. J., et al. 2013, A&A, 558, A33, doi: 10.1051/0004-6361/201322068

Bartos, I., Kocsis, B., Haiman, Z., & Márka, S. 2017, ApJ, 835, 165, doi: 10.3847/1538-4357/835/2/165

Baruteau, C., Cuadra, J., & Lin, D. N. C. 2011, ApJ, 726, 28, doi: 10.1088/0004-637X/726/1/28

Blondin, J. M., & Pope, T. C. 2009, ApJ, 700, 95, doi: 10.1088/0004-637X/700/1/95

Blondin, J. M., & Raymer, E. 2012, ApJ, 752, 30, doi: 10.1088/0004-637X/752/1/30

Bondi, H. 1952, MNRAS, 112, 195, doi: 10.1093/mnras/112.2.195

Bondi, H., & Hoyle, F. 1944, MNRAS, 104, 273, doi: 10.1093/mnras/104.5.273

Bovy, J., Rix, H.-W., Hogg, D. W., et al. 2012, ApJ, 755, 115, doi: 10.1088/0004-637X/755/2/115

Brown, W. R., Geller, M. J., Kenyon, S. J., & Diaferio, A. 2010, AJ, 139, 59, doi: 10.1088/0004-6256/139/1/59

Chanamé, J., & Gould, A. 2004, ApJ, 601, 289, doi: 10.1086/380442

Chandrasekhar, S. 1943, ApJ, 97, 255, doi: 10.1086/144517

Cherepashchuk, A. M. 2014, Physics-Uspekhi, 57, 359

Colella, P., & Woodward, P. R. 1984, Journal of Computational Physics, 54, 174, doi: 10.1016/0021-9991(84)90143-8

Cowley, A. P. 1992, ARA&A, 30, 287, doi: 10.1146/annurev.aa.30.090192.001443

del Valle, L., & Escala, A. 2014, ApJ, 780, 84, doi: 10.1088/0004-637X/780/1/84

Di Stefano, R. 2018, ArXiv e-prints. https://arxiv.org/abs/1805.09338

Duchêne, G., & Kraus, A. 2013, ARA&A, 51, 269, doi: 10.1146/annurev-astro-081710-102602

Edgar, R. 2004, NewAR, 48, 843, doi: 10.1016/j.newar.2004.06.001

Edgar, R. G. 2005, A&A, 434, 41, doi: 10.1051/0004-6361:20042067

Farris, B. D., Duffell, P., MacFadyen, A. I., & Haiman, Z. 2015, MNRAS, 446, L36, doi: 10.1093/mnrasl/slu160

Farris, B. D., Liu, Y. T., & Shapiro, S. L. 2010, PhRvD, 81, 084008, doi: 10.1103/PhysRevD.81.084008

Federrath, C., Banerjee, R., Clark, P. C., & Klessen, R. S. 2010, ApJ, 713, 269, doi: 10.1088/0004-637X/713/1/269

Foglizzo, T., Galletti, P., & Ruffert, M. 2005, A&A, 435, 397, doi: 10.1051/0004-6361:20042201

Fryxell, B., Olson, K., Ricker, P., et al. 2000, ApJS, 131, 273, doi: 10.1086/317361

Hilditch, R. W. 2001, An Introduction to Close Binary Stars, 392

Hoyle, F., & Lyttleton, R. A. 1939, Proceedings of the Cambridge Philosophical Society, 35, 405, doi: 10.1017/S0305004100021150

Hunt, R. 1971, MNRAS, 154, 141, doi: 10.1093/mnras/154.2.141

Ivanov, P. B., Igumenshchev, I. V., & Novikov, I. D. 1998, ApJ, 507, 131, doi: 10.1086/306324

Just, A., Yurin, D., Makukov, M., et al. 2012, ApJ, 758, 51, doi: 10.1088/0004-637X/758/1/51

Kaaz, N., Antoni, A., & Ramirez-Ruiz, E. 2019, arXiv e-prints. https://arxiv.org/abs/1901.03649

Kafle, P. R., Sharma, S., Lewis, G. F., & Bland-Hawthorn, J. 2014, ApJ, 794, 59, doi: 10.1088/0004-637X/794/1/59

Karas, V., & Šubr, L. 2007, A&A, 470, 11, doi: 10.1051/0004-6361:20066068

Kelly, B. J., Baker, J. G., Etienne, Z. B., Giacomazzo, B., & Schnittman, J. 2017, PhRvD, 96, 123003, doi: 10.1103/PhysRevD.96.123003

Kennedy, G. F., Meiron, Y., Shukirgaliyev, B., et al. 2016, MNRAS, 460, 240, doi: 10.1093/mnras/stw908

Kim, C.-G., & Ostriker, E. C. 2017, ApJ, 846, 133, doi: 10.3847/1538-4357/aa8599

Kim, H., & Kim, W.-T. 2007, ApJ, 665, 432, doi: 10.1086/519302

Kim, H., Kim, W.-T., & Sánchez-Salcedo, F. J. 2008, ApJL, 679, L33, doi: 10.1086/589149

Krumholz, M. R., McKee, C. F., & Klein, R. I. 2006, ApJ, 638, 369, doi: 10.1086/498844

MacLeod, M., Antoni, A., Murguia-Berthier, A., Macias, P., & Ramirez-Ruiz, E. 2017, ApJ, 838, 56, doi: 10.3847/1538-4357/aa6117

MacLeod, M., & Ramirez-Ruiz, E. 2015, ApJ, 803, 41, doi: 10.1088/0004-637X/803/1/41

McKernan, B., Ford, K. E. S., Lyra, W., & Perets, H. B. 2012, MNRAS, 425, 460, doi: 10.1111/j.1365-2966.2012.21486.x

McKernan, B., Ford, K. E. S., Lyra, W., et al. 2011, MNRAS, 417, L103, doi: 10.1111/j.1745-3933.2011.01132.x

Miralda-Escudé, J., & Kollmeier, J. A. 2005, ApJ, 619, 30, doi: 10.1086/426467

Moe, M., & Di Stefano, R. 2017, ApJS, 230, 15, doi: 10.3847/1538-4365/aa6fb6

Murguia-Berthier, A., MacLeod, M., Ramirez-Ruiz, E., Antoni, A., & Macias, P. 2017, ApJ, 845, 173, doi: 10.3847/1538-4357/aa8140

Naiman, J. P., Ramirez-Ruiz, E., & Lin, D. N. C. 2011, ApJ, 735, 25, doi: 10.1088/0004-637X/735/1/25

—. 2018, MNRAS, 478, 2794, doi: 10.1093/mnras/sty1198

Naoz, S., & Fabrycky, D. C. 2014, ApJ, 793, 137, doi: 10.1088/0004-637X/793/2/137

Nice, D. J., Stairs, I. H., & Kasian, L. E. 2008, in American Institute of Physics Conference Series, Vol. 983, 40 Years of Pulsars: Millisecond Pulsars, Magnetars and More, ed. C. Bassa, Z. Wang, A. Cumming, & V. M. Kaspi, 453–458

Ostriker, E. C. 1999, ApJ, 513, 252, doi: 10.1086/306858

Panamarev, T., Shukirgaliyev, B., Meiron, Y., et al. 2018, MNRAS, 476, 4224, doi: 10.1093/mnras/sty459

Perets, H. B., Hopman, C., & Alexander, T. 2007, ApJ, 656, 709, doi: 10.1086/510377

Peters, P. C. 1964, Physical Review, 136, 1224, doi: 10.1103/PhysRev.136.B1224

Postnov, K. A., & Yungelson, L. R. 2014, Living Reviews in Relativity, 17, 3, doi: 10.12942/lrr-2014-3

Roupas, Z., & Kazanas, D. 2019, A&A, 621, L1, doi: 10.1051/0004-6361/201834609

Ruffert, M. 1994, A&AS, 106, 505

—. 1995, A&AS, 113, 133

—. 1996, A&A, 311, 817

—. 1999, A&A, 346, 861

Ruffert, M., & Arnett, D. 1994, ApJ, 427, 351, doi: 10.1086/174145

Sabach, E., & Soker, N. 2015, MNRAS, 450, 1716, doi: 10.1093/mnras/stv717

Sánchez-Salcedo, F. J., & Chametla, R. O. 2014, ApJ, 794, 167, doi: 10.1088/0004-637X/794/2/167

Shapiro, S. L., & Teukolsky, S. A. 1983, Black holes, white dwarfs, and neutron stars: The physics of compact objects

Shen, S., Kulkarni, G., Madau, P., & Mayer, L. 2017, MNRAS, 469, 4012, doi: 10.1093/mnras/stx1094

Shima, E., Matsuda, T., Takeda, H., & Sawada, K. 1985, MNRAS, 217, 367, doi: 10.1093/mnras/217.2.367

Stahler, S. W. 2010, MNRAS, 402, 1758, doi: 10.1111/j.1365-2966.2009.15994.x

Stone, N. C., Metzger, B. D., & Haiman, Z. 2017, MNRAS, 464, 946, doi: 10.1093/mnras/stw2260

Syer, D., Clarke, C. J., & Rees, M. J. 1991, MNRAS, 250, 505,
doi: 10.1093/mnras/250.3.505

Tauris, T. M., & van den Heuvel, E. P. J. 2014, ApJL, 781, L13,
doi: 10.1088/2041-8205/781/1/L13

Thun, D., Kuiper, R., Schmidt, F., & Kley, W. 2016, A&A, 589,
A10, doi: 10.1051/0004-6361/201527629

Toonen, S., Hamers, A., & Portegies Zwart, S. 2016,
Computational Astrophysics and Cosmology, 3, 6,
doi: 10.1186/s40668-016-0019-0

Turk, M. J., Smith, B. D., Oishi, J. S., et al. 2011, ApJS, 192, 9,
doi: 10.1088/0067-0049/192/1/9

Šubr, L., & Karas, V. 2005, A&A, 433, 405,
doi: 10.1051/0004-6361:20042089

Bibliography

[1]   F. Hoyle and R. A. Lyttleton, Proceedings of the Cambridge Philosophical Society **35**, 405 (1939).

[2]   H. Bondi, Mon. Not. Royal Astron. Soc. **112**, 195 (1952).

[3]   S. Chandrasekhar, Astroph. Journal **97**, 255 (1943).

[4]   E. C. Ostriker, Astroph. Journal **513**, 252 (1999).

[5]   F. J. Sánchez-Salcedo and R. O. Chametla, Astroph. Journal **794**, 167 (2014).

[6]   S. W. Stahler, Mon. Not. Royal Astron. Soc. **402**, 1758 (2010).

[7]   H. Kim, W.-T. Kim, and F. J. Sánchez-Salcedo, Astroph. Journal Let. **679**, L33 (2008).

[8]   S. Shen, G. Kulkarni, P. Madau, and L. Mayer, Mon. Not. Royal Astron. Soc. **469**, 4012 (2017).

[9]   N. C. Stone, B. D. Metzger, and Z. Haiman, Mon. Not. Royal Astron. Soc. **464**, 946 (2017).

[10] I. Bartos, B. Kocsis, Z. Haiman, and S. Márka, Astroph. Journal **835**, 165 (2017).

[11] H. Bondi and F. Hoyle, Mon. Not. Royal Astron. Soc. **104**, 273 (1944).

[12] B. Fryxell, K. Olson, P. Ricker, F. X. Timmes, M. Zingale, D. Q. Lamb, P. MacNeice, R. Rosner, J. W. Truran, and H. Tufo, Astroph. Journal Sup. **131**, 273 (2000).

[13] E. Shima, T. Matsuda, H. Takeda, and K. Sawada, Mon. Not. Royal Astron. Soc. **217**, 367 (1985).

[14] M. Ruffert, Astron. & Astroph. Sup. **106**, 505 (1994).

[15] M. Ruffert, Astron. & Astroph. Sup. **113**, 133 (1995).

[16] M. Ruffert and D. Arnett, Astroph. Journal **427**, 351 (1994).

[17] J. M. Blondin and E. Raymer, Astroph. Journal **752**, 30 (2012).

[18] R. G. Edgar, Astron. & Astroph. **434**, 41 (2005).

[19] C.-G. Kim and E. C. Ostriker, Astroph. Journal **846**, 133 (2017).

[20] J. Bovy, H.-W. Rix, D. W. Hogg, T. C. Beers, Y. S. Lee, and L. Zhang, Astroph. Journal **755**, 115 (2012).

[21] W. R. Brown, M. J. Geller, S. J. Kenyon, and A. Diaferio, AJ**139**, 59 (2010).

[22] P. R. Kafle, S. Sharma, G. F. Lewis, and J. Bland-Hawthorn, Astroph. Journal **794**, 59 (2014).

[23] R. W. Hilditch, *An Introduction to Close Binary Stars, by R. W. Hilditch, pp. 392. ISBN 0521241065. Cambridge, UK: Cambridge University Press, March 2001.* (PUBLISHER, ADDRESS, 2001), p. 392.

[24] R. Hunt, Mon. Not. Royal Astron. Soc. **154**, 141 (1971).

[25] T. Foglizzo, P. Galletti, and M. Ruffert, Astron. & Astroph. **435**, 397 (2005).

[26] M. Ruffert, Astron. & Astroph. **346**, 861 (1999).

[27] M. Ruffert, Astron. & Astroph. **311**, 817 (1996).

[28] P. Colella and P. R. Woodward, Journal of Computational Physics **54**, 174 (1984).

[29] C. Federrath, R. Banerjee, P. C. Clark, and R. S. Klessen, Astroph. Journal **713**, 269 (2010).

[30] A. Murguia-Berthier, M. MacLeod, E. Ramirez-Ruiz, A. Antoni, and P. Macias, Astroph. Journal **845**, 173 (2017).

[31] M. MacLeod, A. Antoni, A. Murguia-Berthier, P. Macias, and E. Ramirez-Ruiz, Astroph. Journal **838**, 56 (2017).

[32] M. MacLeod and E. Ramirez-Ruiz, Astroph. Journal **803**, 41 (2015).

[33] D. Thun, R. Kuiper, F. Schmidt, and W. Kley, Astron. & Astroph. **589**, A10 (2016).

[34] S. L. Shapiro and S. A. Teukolsky, *Research supported by the National Science Foundation. New York, Wiley-Interscience, 1983, 663 p.* (PUBLISHER, ADDRESS, 1983).

[35] P. C. Peters, Physical Review **136**, 1224 (1964).

[36] J. J. Andrews, J. Chanamé, and M. A. Agüeros, Research Notes of the American Astronomical Society **2**, 29 (2018).

[37] J. J. Andrews, J. Chanamé, and M. A. Agüeros, Mon. Not. Royal Astron. Soc. **472**, 675 (2017).

[38] E. Sabach and N. Soker, Mon. Not. Royal Astron. Soc. **450**, 1716 (2015).

[39] J. Miralda-Escudé and J. A. Kollmeier, Astroph. Journal **619**, 30 (2005).

[40] P. Artymowicz, D. N. C. Lin, and E. J. Wampler, Astroph. Journal **409**, 592 (1993).

[41] M. Moe and R. Di Stefano, Astroph. Journal Sup. **230**, 15 (2017).

[42] S. Naoz and D. C. Fabrycky, Astroph. Journal **793**, 137 (2014).

[43] T. M. Tauris and E. P. J. van den Heuvel, Astroph. Journal Let. **781**, L13 (2014).

[44] M. J. Turk, B. D. Smith, J. S. Oishi, S. Skory, S. W. Skillman, T. Abel, and M. L. Norman, Astroph. Journal Sup. **192**, 9 (2011).

[45] Astropy Collaboration, T. P. Robitaille, E. J. Tollerud, P. Greenfield, M. Droettboom, E. Bray, T. Aldcroft, M. Davis, A. Ginsburg, A. M. Price-Whelan, W. E. Kerzendorf, A. Conley, N. Crighton, K. Barbary, D. Muna, H. Ferguson, F. Grollier, M. M. Parikh, P. H. Nair, H. M. Unther, C. Deil, J. Woillez, S. Conseil, R. Kramer, J. E. H. Turner, L. Singer, R. Fox, B. A. Weaver, V. Zabalza, Z. I. Edwards, K. Azalee Bostroem, D. J. Burke, A. R. Casey, S. M. Crawford, N. Dencheva, J. Ely, T. Jenness, K. Labrie, P. L. Lim, F. Pierfederici, A. Pontzen, A. Ptak, B. Refsdal, M. Servillat, and O. Streicher, Astron. & Astroph. **558**, A33 (2013).